

UNIVERSITY OF CALIFORNIA

Los Angeles

**Amplification of Short Laser Pulses via  
Resonant Energy Transfer in Underdense  
Thermal Plasmas**

A dissertation submitted in partial satisfaction  
of the requirements for the degree  
Doctor of Philosophy in Electrical Engineering

by

**Tyan-Lin Wang**

2010

© Copyright by  
Tyan-Lin Wang  
2010

The dissertation of Tyan-Lin Wang is approved.

---

Troy Carter

---

Christoph Niemann

---

Warren Mori

---

Chandrasekhar Joshi, Committee Chair

University of California, Los Angeles

2010

*This thesis is dedicated to the scientists in the field of laser-plasma interactions who had the patience, interest, and most importantly, time to assist and support me throughout the research process.*

# TABLE OF CONTENTS

<b>1 Introduction . . . . .</b>	<b>1</b>
1.1 Using plasma for amplification of laser pulses . . . . .	1
1.2 Selected previous work on BRA . . . . .	4
1.2.1 PIC Simulations . . . . .	5
1.2.2 Experiments . . . . .	9
1.3 Purpose of this dissertation and outline . . . . .	13
<b>2 Stimulated Raman Scattering and Backward Raman Amplification (BRA) Physical Concepts . . . . .</b>	<b>18</b>
2.1 Derivation of the Three Wave Equations Describing Raman Scattering and Light Wave Coupling . . . . .	18
2.2 Theory behind the BRA process . . . . .	23
2.3 Plasma wave dynamics and their impact on laser beams in BRA .	26
2.4 Multi-dimensional aspects of BRA . . . . .	30
2.5 Motivation for choosing 1054 nm as the pump wavelength . . . . .	31
<b>3 1D OSIRIS Simulations of Ultrashort Pulse Backward Raman Amplification (BRA) . . . . .</b>	<b>35</b>
3.1 Case studies of ultrashort pulse amplification . . . . .	35
3.1.1 Case I . . . . .	37
3.1.2 Case II . . . . .	42
3.1.3 Case III . . . . .	47

3.1.4	Case IV . . . . .	51
3.2	Optimal plasma conditions for amplification . . . . .	54
<b>4</b>	<b>Creating Seed Laser Pulses . . . . .</b>	<b>60</b>
4.1	Description of the experiment . . . . .	60
4.2	Experimental layout and procedure . . . . .	66
4.3	Experimental results . . . . .	70
<b>5</b>	<b>Amplifying Seed Laser Pulses . . . . .</b>	<b>78</b>
5.1	Introduction . . . . .	78
5.2	Experimental layout and procedure . . . . .	84
5.3	Experimental results . . . . .	90
<b>6</b>	<b>Experimental Results Compared to Simulations . . . . .</b>	<b>106</b>
6.1	Description of phase plates . . . . .	106
6.2	1D OSIRIS and 2D pF3d simulations using experimental parameters	110
6.3	Additional BRA studies comparing 1D OSIRIS to 2D pF3d . . . . .	124
<b>7</b>	<b>Summary and Ideas for Future Work . . . . .</b>	<b>142</b>
7.1	Summary . . . . .	142
7.2	Ideas for Future Work . . . . .	145
<b>A</b>	<b>Extended Three Wave Model . . . . .</b>	<b>149</b>
	<b>References . . . . .</b>	<b>159</b>

## LIST OF FIGURES

1.1	Depiction of the SRS cycle (left) and of BRA (right). . . . .	4
2.1	Mathematical plots of a $\pi$ -pulse solution (left) and a normalized seed intensity waveform (right). . . . .	25
2.2	Multi-dimensional representation of a $\pi$ -pulse solution from a pre-focused seed. . . . .	31
2.3	Cartoon drawing showing re-amplified SRS from a LEH (left) and the Janus experiment (right) which has pump and seed lasers interacting in a plasma made from a gas jet. . . . .	33
3.1	Case I - Snapshots of the seed at various times during amplification (left panels) and k spectrum of the pump, seed, and electrostatic waves (right panels). Reprinted with permission from T.-L. Wang, D. S. Clark, D. J. Strozzi, S. C. Wilks, S. F. Martins, and R. K. Kirkwood, Phys. Plasmas <b>17</b> , 023109 (2010). Copyright 2010, American Institute of Physics. . . . .	39
3.2	Wigner transform of the seed pulse undergoing amplification for Case I. . . . .	40
3.3	Case I - Color scheme representation of the seed waveform. The bottom row shows zoomed-out snapshots of the seed waveform in the entire box. . . . .	41

3.4	Case I - Phase space features at different locations inside the seed pulse. The center image shows the plasma wave with amplitude $a_2 = eE_2/m\omega_0c = 0.01$ . Non-resonant wave vector components have been filtered out and shown with the initial unfiltered plasma wave. Reprinted with permission from T.-L. Wang, D. S. Clark, D. J. Strozzi, S. C. Wilks, S. F. Martins, and R. K. Kirkwood, Phys. Plasmas <b>17</b> , 023109 (2010). Copyright 2010, American Institute of Physics. . . . .	43
3.5	Case II - Snapshots of the seed at various times during amplification (left panels) and k spectrum of the pump, seed, and electrostatic waves (right panels). Reprinted with permission from T.-L. Wang, D. S. Clark, D. J. Strozzi, S. C. Wilks, S. F. Martins, and R. K. Kirkwood, Phys. Plasmas <b>17</b> , 023109 (2010). Copyright 2010, American Institute of Physics. . . . .	44
3.6	Wigner transform of the seed pulse undergoing amplification for Case II. . . . .	45
3.7	Case II - Color scheme representation of the seed waveform. The bottom row shows zoomed-out snapshots of the seed waveform in the entire box. . . . .	46

3.8	Case II - Phase space features at different locations inside the seed pulse. The center image shows the plasma wave with amplitude $a_2 = eE_2/m\omega_0c = 0.007$ . Non-resonant wave vector components have been filtered out and shown with the initial unfiltered plasma wave. Reprinted with permission from T.-L. Wang, D. S. Clark, D. J. Strozzi, S. C. Wilks, S. F. Martins, and R. K. Kirkwood, Phys. Plasmas <b>17</b> , 023109 (2010). Copyright 2010, American Institute of Physics. . . . .	48
3.9	Case III - Snapshots of the seed at various times during amplification (left panels) and k spectrum of the pump, seed, and electrostatic waves (right panels). Reprinted with permission from T.-L. Wang, D. S. Clark, D. J. Strozzi, S. C. Wilks, S. F. Martins, and R. K. Kirkwood, Phys. Plasmas <b>17</b> , 023109 (2010). Copyright 2010, American Institute of Physics. . . . .	49
3.10	Wigner transform of the seed pulse undergoing amplification for Case III. . . . .	50
3.11	Case III - Phase space features at different locations inside the seed pulse. The center image shows the plasma wave with amplitude $a_2 = eE_2/m\omega_0c = 0.0017$ . Non-resonant wave vector components have been filtered out and shown with the initial unfiltered plasma wave. Reprinted with permission from T.-L. Wang, D. S. Clark, D. J. Strozzi, S. C. Wilks, S. F. Martins, and R. K. Kirkwood, Phys. Plasmas <b>17</b> , 023109 (2010). Copyright 2010, American Institute of Physics. . . . .	51

3.12	Case IV - Snapshots of the seed at various times during amplification (left panels) and k spectrum of the pump, seed, and electrostatic waves (right panels). Reprinted with permission from T.-L. Wang, D. S. Clark, D. J. Strozzi, S. C. Wilks, S. F. Martins, and R. K. Kirkwood, Phys. Plasmas <b>17</b> , 023109 (2010). Copyright 2010, American Institute of Physics. . . . .	53
3.13	Wigner transform of the seed pulse undergoing amplification for Case IV. . . . .	54
3.14	Case IV - Phase space features at different locations inside the seed pulse. The center image shows the plasma wave with amplitude $a_2 = eE_2/m\omega_0c = 0.003$ . Non-resonant wave vector components have been filtered out and shown with the initial unfiltered plasma wave. Reprinted with permission from T.-L. Wang, D. S. Clark, D. J. Strozzi, S. C. Wilks, S. F. Martins, and R. K. Kirkwood, Phys. Plasmas <b>17</b> , 023109 (2010). Copyright 2010, American Institute of Physics. . . . .	55
3.15	Density vs temperature plot showing parameter regime for optimal seed amplification. The four cases presented earlier are indicated by the circles. Optimal amplification of the seed is shown to be possible for plasma densities between $0.01 n_{cr}$ and $0.015 n_{cr}$ and temperatures up to 200 eV. Reprinted with permission from T.-L. Wang, D. S. Clark, D. J. Strozzi, S. C. Wilks, S. F. Martins, and R. K. Kirkwood, Phys. Plasmas <b>17</b> , 023109 (2010). Copyright 2010, American Institute of Physics. . . . .	57
4.1	Potential energy curves showing the electronic, vibrational, and rotational levels of a molecule. . . . .	62

4.2	Simple energy level diagram showing Stokes and anti-Stokes transitions. . . . .	63
4.3	Schematic of the 2 meter long Raman gas cell. The inset shows the arrangement of the internal telescope optics. . . . .	65
4.4	Schematic of the Raman cell. . . . .	68
4.5	Pictures of the experimental setup. . . . .	69
4.6	Results of Raman lines produced with $H_2$ , $N_2O$ , and $C_3H_8$ gases. The red vertical line is a reference marker for 1200 nm, showing where it falls in the seed spectrum. All vertical axes are in raw counts. . . . .	73
4.7	COMET laser energy scan for $N_2O$ gas at 150 psi. . . . .	74
4.8	Typical autocorrelation trace giving a pulsewidth measurement of 3.7 ps for the laser pulse converted by $N_2O$ gas. . . . .	76
4.9	Comparison of normalized spectra for 0.67 ps and 3.7 ps pulses for $N_2O$ gas. . . . .	76
5.1	Overall schematic of the seed amplification experiment. . . . .	85
5.2	View of the various laser beam paths in Target Area 1. . . . .	86
5.3	Pictures of the experimental setup. . . . .	87
5.4	Typical plasma density interferogram. . . . .	91
5.5	Post-processed plasma density profiles. . . . .	92
5.6	Experimental results of short pulse seed amplification with vertical axis in raw counts. The initial seed energies are: 5.88 $\mu J$ (top left), 54.4 $\mu J$ (top right), 160 $\mu J$ (bottom left), 228 $\mu J$ (bottom right) .	93

5.7	Overlaid raw seed spectra for shots 64 -- 126, 67 -- 132, and 65 -- 129 along with SRS noise spectrum before (top) and after (bottom) amplification. . . . .	99
5.8	SRS noise spectrum in terms of peak spectral energy. . . . .	100
5.9	Short pulse seed amplification results. Peak spectral energy is shown in shaded green diamonds and integrated energy is shown in blue outlined diamonds. . . . .	101
5.10	Long pulse seed amplification results. Peak spectral energy is shown in shaded orange diamonds. . . . .	102
5.11	Plot of output peak intensity (top) and intensity gain (bottom) versus input peak intensity. Short pulse data are shown in shaded green diamonds and long pulse data in shaded orange diamonds. The two short pulse points with uncertainty in the gain are circled.	103
5.12	Comparison of parameters between the Princeton and LLNL experiments. . . . .	104
5.13	1D photodiode lineout of the seed spot profile and amplifier bandwidth measured from a pump and seed spectrum. Reprinted with permission from Y. Ping, R. K. Kirkwood, T.-L. Wang, D. S. Clark, S. C. Wilks, N. Meezan, R. L. Berger, J. Wurtele, N. J. Fisch, V. M. Malkin, E. J. Valeo, S. F. Martins, and C. Joshi, Phys. Plasmas <b>16</b> , 123113 (2009). Copyright 2009, American Institute of Physics. . . . .	105
6.1	Cartoon drawing of a phase plate with a focusing lens and speckles at focus. . . . .	108

6.2	Piecewise density profile used in the simulations shown in Figure 6.3. Negative signs indicate that the values refer to the electron density. The vertical axis is in units of critical density, which is $1 \times 10^{21} \text{ cm}^{-3}$ . Areas having zero density correspond to vacuum regions. . . . .	111
6.3	Initial and final seed amplification results in a 1D OSIRIS run for the 0.67 ps, $3.26 \times 10^{11} \text{ W/cm}^2$ (top) and 3.7 ps, $4.36 \times 10^{11} \text{ W/cm}^2$ (bottom) cases. The plasma slab is indicated by the red rectangle.	113
6.4	Simulations showing SRS backscattered light from the pump laser for an initial pump intensity of $1.11 \times 10^{14} \text{ W/cm}^2$ (left) and 99% transmission of an unamplified 0.67 ps, $3.26 \times 10^{11} \text{ W/cm}^2$ seed passing through the plasma (right). Length scales are in terms of pump wavelengths and intensities in the color table are normalized to the initial pump intensity of $1.11 \times 10^{14} \text{ W/cm}^2$ . . . . .	119
6.5	Final seed amplification results in a 2D pF3d run for the 0.67 ps, $3.26 \times 10^{11} \text{ W/cm}^2$ (top) and 3.7 ps, $4.36 \times 10^{11} \text{ W/cm}^2$ (bottom) cases. Length scales are in terms of pump wavelengths and intensities in the color table are normalized to the initial pump intensity of $1.11 \times 10^{14} \text{ W/cm}^2$ . . . . .	120
6.6	Simulation plots of intensity gain versus input peak intensity for 0.67 ps short pulse (top) and 3.7 ps long pulse (bottom) cases. Experimental data points are shown along with the 1D OSIRIS and 2D pF3d simulation data points. . . . .	131

6.7	1D OSIRIS results for both low $k_2\lambda_D$ and high $k_2\lambda_D$ cases. Shown are the squared electric field of the seed (top), the amplitude of the plasma wave (middle), and the squared electric field of the pump (bottom). . . . .	132
6.8	Low $k_2\lambda_D$ case results for Gaussian pump (left column), Gaussian seed (center column), and driven plasma wave (right column). Intensities are normalized to the initial pump intensity of $2.8\times 10^{14} W/cm^2$ . Plasma wave amplitudes are normalized to the critical density. . . . .	133
6.9	Low $k_2\lambda_D$ case final contour plots for Gaussian pump (bottom) and Gaussian seed (top). Intensities are normalized to the initial pump intensity of $2.8\times 10^{14} W/cm^2$ . The pump moves to the left in the sense of coming out of the page and the seed moves to the right in the sense of going into the page. . . . .	134
6.10	Low $k_2\lambda_D$ case results for RPP pump (left column), Gaussian seed (center column), and driven plasma wave (right column). Intensities are normalized to the initial pump intensity of $2.8\times 10^{14} W/cm^2$ . Plasma wave amplitudes are normalized to the critical density. . . . .	135
6.11	Low $k_2\lambda_D$ case final contour plots for RPP pump (bottom) and Gaussian seed (top). Intensities are normalized to the initial pump intensity of $2.8\times 10^{14} W/cm^2$ . The pump moves to the left in the sense of coming out of the page and the seed moves to the right in the sense of going into the page. . . . .	136

6.12	High $k_2\lambda_D$ case results for Gaussian pump (left column), Gaussian seed (center column), and driven plasma wave (right column). Intensities are normalized to the initial pump intensity of $2.8\times 10^{14} W/cm^2$ . Plasma wave amplitudes are normalized to the critical density. . . . .	137
6.13	High $k_2\lambda_D$ case final contour plots for Gaussian pump (bottom) and Gaussian seed (top). Intensities are normalized to the initial pump intensity of $2.8\times 10^{14} W/cm^2$ . The pump moves to the left in the sense of coming out of the page and the seed moves to the right in the sense of going into the page. . . . .	138
6.14	High $k_2\lambda_D$ case results for RPP pump (left column), Gaussian seed (center column), and driven plasma wave (right column). Intensities are normalized to the initial pump intensity of $2.8\times 10^{14} W/cm^2$ . Plasma wave amplitudes are normalized to the critical density. . . . .	139
6.15	High $k_2\lambda_D$ case final contour plots for RPP pump (bottom) and Gaussian seed (top). Intensities are normalized to the initial pump intensity of $2.8\times 10^{14} W/cm^2$ . The pump moves to the left in the sense of coming out of the page and the seed moves to the right in the sense of going into the page. . . . .	140
6.16	Plot of electrostatic field amplitude versus input peak intensity for 0.67 ps short pulse (green) and 3.7 ps long pulse (orange) cases in the 1D OSIRIS and 2D pF3d simulations. OSIRIS points are connected by solid lines and pF3d points are connected by dashed lines. The gray dotted line shows the trapping threshold. . . . .	141

7.1	Cartoon showing counter-propagating and shallow angle configurations for pump and seed interaction. . . . .	147
A.1	Snapshots of the 1054 nm pump laser envelope (dash-dotted red line for ETW, solid magenta line for PIC) and the 1300 nm seed laser envelope (dashed green line for ETW, blue line for PIC) interacting in a cold plasma at (a) near the beginning of the simulation, with the seed still outside the plasma and the pump just entering the plasma and (b) near the end of the simulation, after the bulk of the seed and pump envelopes have exited the plasma. The vertical dashed lines indicate the boundaries of the 1 mm plasma slab. Reprinted with permission from T.-L. Wang, D. Michta, R. R. Lindberg, A. E. Charman, S. F. Martins, and J. S. Wurtele, Phys. Plasmas <b>16</b> , 123110 (2009). Copyright 2009, American Institute of Physics. . . . .	156
A.2	Profiles of the final seed laser envelopes (green line for ETW, blue line for PIC, dashed line for LTW) after exiting the plasma for (a) cold, (b) 78 eV, (c) 142 eV, (d) 200 eV, (d) 365 eV, (e) 525 eV cases. Due to the difference in group velocities, the PIC waveforms have been shifted to best overlap with the ETW and LTW envelopes. Reprinted with permission from T.-L. Wang, D. Michta, R. R. Lindberg, A. E. Charman, S. F. Martins, and J. S. Wurtele, Phys. Plasmas <b>16</b> , 123110 (2009). Copyright 2009, American Institute of Physics. . . . .	157

A.3 Time-series of normalized peak intensity versus time for (a) cold, (b) 78 eV, (c) 142 eV, (d) 200 eV, (d) 365 eV, and (e) 525 eV cases, showing predictions of the ETW (green line), PIC (blue line), and LTW (dotted line) models. At time  $t = 0$  ps the peak of the seed and the peak of the pump meet close to the the leading (left) edge of the plasma slab. Reprinted with permission from T.-L. Wang, D. Michta, R. R. Lindberg, A. E. Charman, S. F. Martins, and J. S. Wurtele, Phys. Plasmas **16**, 123110 (2009). Copyright 2009, American Institute of Physics. . . . . 158

## LIST OF TABLES

1.1	Comparison of selected PIC simulation work on BRA . . . . .	5
1.2	Comparison of selected experimental work on BRA . . . . .	10
2.1	Comparison of typical NIF LEH and Gas Bag experiment parameters to the Janus experiment . . . . .	33
4.1	Candidate Raman gases for seed pulse generation. . . . .	66
5.1	Plasma parameters for the seed amplification experiment. . . . .	83
6.1	Parameters used for simulations comparing 1D OSIRIS to 2D pF3d	125
A.1	Parameters used for simulations comparing the ETW, PIC, and LTW models . . . . .	152

## ACKNOWLEDGMENTS

I want to thank my committee chair, Prof. Chandrasekhar Joshi, for being my thesis advisor and for giving me financial support as a GSR during one of my years in graduate school. Going on to the rest of my committee, I want to thank Prof. Warren Mori for letting me attend his simulation group meetings and for granting me computational time to run the OSIRIS code on the Dawson and Hoffman2 clusters. Without this resource I would not have been able to accomplish a large fraction of my work. I want to thank Prof. Christoph Niemann for taking me on a group field trip to Lawrence Livermore National Laboratory (LLNL) several years ago to see the National Ignition Facility (NIF). This led to an opportunity for me to do research at LLNL, which eventually became the foundation of my thesis work. I also want to thank Prof. Troy Carter for showing interest in my research and providing me with useful feedback and questions to think about.

Next I want to thank the PI of the backward Raman amplification (BRA) experimental project, Robert Kirkwood, for serving as my local advisor during my time at LLNL. I also want to thank the co-PI, Yuan Ping, for useful discussions and assistance with the experiment. I want to thank Scott Wilks for his encouragement and support during my initial efforts to run simulations to study the BRA problem. Others that I'd like to thank for fruitful discussions and assistance during my time at LLNL are David Turnbull, Mark Henesian, Norm Kurnit, Ying Tsui, Mahadevan Krishnan, and the members of the Jupiter Laser Facility (JLF) staff, including Dwight Price, Jim Hunter, Gary Freeze, and Beth Mariotti. I'm also grateful to Nathan Meezan for running a few HYDRA simulations for our experiment, and Dave Strozzi and Dick Berger for their patience, assistance, and computational resources during the latter stages of my research

when I was running the pF3d code. I also acknowledge the technical support of the Livermore Computing Center staff. I'm especially grateful to Dan Clark for taking me under his wing and making spare time to meet almost every week to discuss the concepts behind BRA and to mull over my latest simulation results with me. His knowledge, insightfulness, and analytical ability have all made a huge impression on me and I consider him to be a great role model.

Finally I want to thank Prof. Jonathan Wurtele for hosting me in his group each time I visited UC Berkeley, and his current and former group members Andy Charman, Ryan Lindberg, David Michta, and Peter Mardahl. Back at UCLA, those that I want to thank include Jay Fahlen, Ben Winjum, Samuel Martins, and Frederico Fiuza for discussions regarding the OSIRIS code and Michail Tzoufras and Chengkun Huang for discussions on general simulation issues. I also thank the OSIRIS Consortium for allowing me to use the OSIRIS code for my research. In regards to administrative support, I want to thank Maria Guerrero at UCLA and Terrie Valin and Peggy Sharp at LLNL. Lastly, I acknowledge the financial support from Raytheon Company in the form of a full-study doctoral fellowship, which was critical during my final two years in the graduate program.

## VITA

- 1982            Born in Taipei, Taiwan
- 2002            B.S., Electrical Engineering (Summa Cum Laude)  
University of California, Los Angeles  
Los Angeles, CA
- 2004            M.S., Electrical Engineering  
University of California, Los Angeles  
Los Angeles, CA
- 2007 - 2008    Graduate Student Researcher  
Department of Electrical Engineering  
University of California, Los Angeles  
Los Angeles, CA
- 2008 - 2010    Academic Cooperation Program Student  
Lawrence Livermore National Laboratory  
Livermore, CA
- 2008 - 2010    Raytheon Doctoral Fellowship  
Raytheon Company Space and Airborne Systems  
El Segundo, CA

## PUBLICATIONS

T.-L. Wang, D. S. Clark, D. J. Strozzi, S. C. Wilks, S. F. Martins, and R. K.

Kirkwood, “Particle-in-cell simulations of kinetic effects in plasma-based backward Raman amplification in underdense plasmas”, *Phys. Plasmas* **17**, 023109 (2010).

Y. Ping, R. K. Kirkwood, T.-L. Wang, D. S. Clark, S. C. Wilks, N. Meezan, R. L. Berger, J. Wurtele, N. J. Fisch, V. M. Malkin, E. J. Valeo, S. F. Martins, and C. Joshi, “Development of a nanosecond-laser-pumped Raman amplifier for short laser pulses in plasma”, *Phys. Plasmas* **16**, 123113 (2009).

T.-L. Wang, D. Michta, R. R. Lindberg, A. E. Charman, S. F. Martins, and J. S. Wurtele, “Feasibility study for using an extended three-wave model to simulate plasma-based backward Raman amplification in one spatial dimension”, *Phys. Plasmas* **16**, 123110 (2009).

D. H. Froula, C. E. Clayton, T. Doppner, K. A. Marsh, C. P. J. Barty, L. Divol, R. A. Fonseca, S. H. Glenzer, C. Joshi, W. Lu, S. F. Martins, P. Michel, W. B. Mori, J. P. Palastro, B. B. Pollock, A. Pak, J. E. Ralph, J. S. Ross, C. W. Siders, L. O. Silva, and T. Wang, “Measurements of the Critical Power for Self-Injection of Electrons in a Laser Wakefield Accelerator”, *Phys. Rev. Lett.* **103**, 215006, (2009).

T.-L. Wang, “Appearance of Density Cavitations in the Laser Wake in Simulations of High Intensity Laser-Plasma Interactions”, *Advanced Accelerator Concepts: 13th Workshop Proceedings* (2009).

G. Li, R. Yan, C. Ren, T.-L. Wang, J. Tonge, and W.B. Mori, “Laser Channeling

in Millimeter-Scale Underdense Plasmas of Fast-Ignition Targets”, Phys. Rev. Lett. **100**, 125002, (2008).

ABSTRACT OF THE DISSERTATION

**Amplification of Short Laser Pulses via  
Resonant Energy Transfer in Underdense  
Thermal Plasmas**

by

**Tyan-Lin Wang**

Doctor of Philosophy in Electrical Engineering

University of California, Los Angeles, 2010

Professor Chandrasekhar Joshi, Chair

Resonant energy transfer between two laser beams based on the stimulated Raman scattering (SRS) process in underdense thermal plasmas is studied in the context of being a potential mechanism to amplify laser pulses. We demonstrate experimentally the amplification of picosecond-scale seed laser pulses by a nanosecond pump laser pulse inside a millimeter-scale plasma with density such that the plasma frequency satisfies the resonance condition for energy transfer. We then compare the experimental results to simulation results from 1D Particle-In-Cell (PIC) and 2D envelope three wave model codes. Along with the prospect of obtaining amplification, there are adverse physical effects in the plasma such as SRS noise, absorption and self-focusing of the laser beams, and plasma kinetic behavior leading to detuning from resonance and saturation of the gain. We discuss these issues as they arise in both the experimental and simulation results and show how they can place limitations on the peak intensity and beam quality that can be achieved. Possible ideas for mitigating some of these physical restrictions will be given.

# CHAPTER 1

## Introduction

### 1.1 Using plasma for amplification of laser pulses

Stimulated Raman scattering (SRS) in underdense plasmas, long known to be a deleterious laser-plasma interaction (LPI) effect in inertial confinement fusion experiments [1], was proposed about a decade ago as a potentially useful mechanism which may be exploited for the simultaneous amplification and compression of a laser pulse, resulting in orders of magnitude higher powers than those produced by chirped pulse amplification (CPA) laser systems [2]. The technique, referred to as backward Raman amplification (BRA), is based on the premise that a plasma can withstand very high energy densities due to its ionized nature. This has motivated research to realize a “plasma amplifier” to further boost the power of an existing CPA system [3] or as an alternative technique that will replace CPA itself [4, 5]. The idea of the Raman effect in various media to amplify laser pulses extends back to work carried out 40 years ago when researchers used gases and liquids to amplify excimer laser pulses for the purpose of laser-based nuclear fusion [6, 7]. The idea of using plasmas for this same purpose is however more recent. Proof-of-principle experiments demonstrating BRA in a plasma have been reported by several groups over the last 10 years [8, 9, 10, 11]. These recent studies have focused primarily on the amplification of ultrashort Ti:Sapphire laser pulses with the goal of creating ultrahigh peak intensities by

significantly increasing the amount of energy contained in a single femtosecond-scale pulse. If some day the goal of creating a single laser pulse with extremely high intensity is achieved, it may open new possibilities for experiments in the area of superstrong field science [12, 13] or in fast ignition [14].

BRA of a laser pulse, just like SRS, is a three-wave interaction of laser light with a plasma of density lower than one quarter of the critical density. Here critical density is that density where the plasma frequency equals the laser frequency. The three waves in BRA consist of a long low intensity pump laser pulse, a short low intensity seed laser pulse that is to be amplified, and an electron plasma wave that is excited by the beating of the two laser pulses. The pump and seed are both electromagnetic waves while the electron plasma wave, or Langmuir wave, is an electrostatic wave. The SRS process, depicted on the left of Figure 1.1, is somewhat different from the BRA process, shown on the right. The SRS instability occurs when a light wave with a frequency  $\omega_0$  and wave vector  $\vec{k}_0$  enters a plasma and Thomson scatters from noise density fluctuations via a resonant interaction that picks a specific  $\omega_1$  and  $\vec{k}_1$  for the scattered light to conserve energy and momentum at frequency  $\omega_2 = \omega_0 - \omega_1$  and wave vector  $\vec{k}_2 = \vec{k}_0 - \vec{k}_1$ . The scattered light in turn beats with the incident light to create a ponderomotive force proportional to the gradient of the product of their individual amplitudes. This force will then reinforce the density noise resulting in even larger perturbations inside the plasma which become a plasma wave with  $\omega_2$  and  $\vec{k}_2$ . The plasma wave behaves like a density grating which causes further collective scattering of the incident light as the instability cycle continues. The cycle is maintained as long as phase-matching and conservation of total wave action are satisfied. BRA relies upon the backward SRS instability to amplify the short seed laser pulse. In this direct backscatter geometry the pump laser is collided with a counter-propagating injected short seed laser inside the plasma as

shown on the right picture in Figure 1.1. The seed laser frequency is downshifted from the pump laser frequency by the plasma frequency in order to achieve the resonance that would have automatically occurred in backward SRS from the plasma noise. Because the injected seed laser in BRA is stronger than the initially Thomson scattered light from backward SRS, the ponderomotive force and the driven plasma wave amplitude in BRA are larger which can induce a greater amount of energy transfer from the pump to the seed mediated by the plasma wave. The seed can cause pump depletion, suppressing the SRS instability. The slow moving plasma wave has a phase velocity in the same direction as the pump, but its group velocity moves with the short laser pulse being amplified.

Since this process is based on the backward SRS instability, the seed gets amplified until the pump begins to be depleted. As mentioned above, the attraction of this idea is due to the fact that a plasma is capable of withstanding laser pulses of very high intensities that normally would destroy solid state optics such as diffraction gratings used in a CPA system. However a plasma exhibits an abundance of other complex nonlinear behavior not found in ordinary media. For instance, a plasma is highly susceptible to additional transverse and longitudinal instabilities in the presence of a high intensity laser beam. The transverse instabilities can adversely affect the laser spot quality and the longitudinal instabilities can cause the pulse shape to break apart. Both types of instabilities can play a role in reducing the efficiency of the energy transfer process. Therefore the physical restrictions on energy transfer efficiency may place limitations on the amount of seed amplification and the final intensity the seed pulse can reach. As we will discuss in Chapter 2, the onset of these instabilities and their severity depend on the plasma conditions and on the properties of the interacting laser pulses. All of this limits the intensities of amplifying laser pulses and the time scale over which they can grow. Therefore the idea of using stimulated Raman

backscattering in a plasma to achieve fast amplification and compression of lasers is still an ongoing research concept.

## 1.2 Selected previous work on BRA

In this section we review some of the results from previous work conducted by several groups that have done either Particle-In-Cell (PIC) computer simulations or laboratory experiments on the topic of BRA. The motivation for their work came from earlier papers by Malkin, Shvets, and Fisch describing the amplification of laser beams using resonant Raman backscattering in plasmas and proposing the possibility of pump depletion as a means of achieving large output laser intensities.

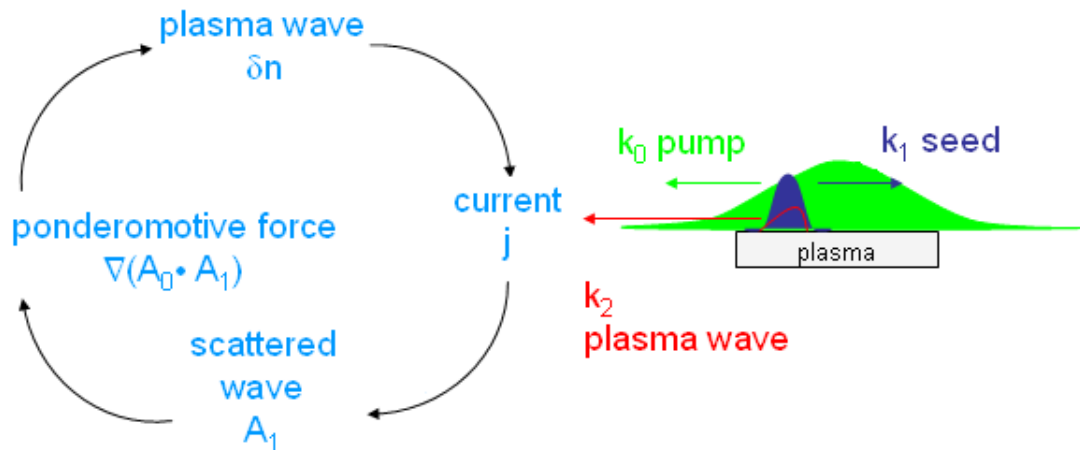


Figure 1.1: Depiction of the SRS cycle (left) and of BRA (right).

Table 1.1: Comparison of selected PIC simulation work on BRA

Investigator	D. Clark	P. Mardahl	R. Trines
Pump wavelength (nm)	1064	1054	800
Pump pulsewidth (ps)	infinite	infinite	infinite
Pump intensity ( $W/cm^2$ )	$2.8 \times 10^{14}$	$2.8 \times 10^{15}$	$1 \times 10^{15}$
Initial seed pulsewidth (fs)	100	50	50
Final seed pulsewidth (fs)	50	50	25
Seed spot size FWHM ( $\mu\text{m}$ )	n/a	6	600
Initial seed intensity ( $W/cm^2$ )	$1.8 \times 10^{14}$	$2.1 \times 10^{15}$	$1 \times 10^{16}$
Final seed intensity ( $W/cm^2$ )	$1.4 \times 10^{16}$	$4.7 \times 10^{17}$	$5 \times 10^{17}$
Plasma length (mm)	1.4	1	4
Plasma density ( $\text{cm}^{-3}$ )	$2.5 \times 10^{19}$	$1 \times 10^{19}$	$4.3 \times 10^{18}$
Plasma temperature (eV)	200	0	0
PIC Code	ZOHAR	XOOPIC	XOOPIC

### 1.2.1 PIC Simulations

Computer simulations have played an integral role in the study of BRA. Because BRA requires two very different pulse length lasers with frequency difference in the 10 THz range, there are not many laboratories that are experimentally studying this amplification scheme. Researchers instead are using theory or simulations to optimize the BRA process by choosing different combinations of laser and plasma parameters. In recent years a few research groups with access to PIC codes have used them to study BRA since PIC codes take into account kinetic effects such as Landau damping and particle trapping. Here we summarize some of their results. Table 1.1 provides a side-by-side comparison of PIC simulation results reported by D. Clark et. al., R. Trines et. al., and P. Mardahl et. al.. The

table lists the relevant parameters for one case study done by each author and their results. Since the transit time of the seed pulse through the plasma is only a few ps it is a common practice in simulation studies of BRA to model the pump pulse as an infinite plane wave. D. Clark et. al. at Princeton University was the first to report results of 1D PIC simulations in a preformed uniform plasma with immobile ions [15, 16] and a finite temperature using the code ZOHAR. He conducted an investigation of the efficiency of Raman amplification by varying the plasma density for a fixed plasma temperature of 200 eV and a pump wavelength of  $1.064 \mu\text{m}$ . He prescribed a seed with an initial pulsewidth of 100 fs, a wavelength adjusted to match the resonance for each plasma condition, and an intensity of  $1.8 \times 10^{14} \text{ W/cm}^2$ , which was comparable to the pump intensity of  $2.8 \times 10^{14} \text{ W/cm}^2$ . Following along with the 1D theory of BRA in cold plasmas [4] they started with a plasma density at the cold wavebreaking limit, a concept we will explain in more detail in Chapter 2, and increased the density in subsequent simulations. In particular they began with a density of  $1.5 \times 10^{19} \text{ cm}^{-3}$  and later went to  $2.5 \times 10^{19} \text{ cm}^{-3}$  and  $3.5 \times 10^{19} \text{ cm}^{-3}$ . He found that at  $1.5 \times 10^{19} \text{ cm}^{-3}$  there was minimal depletion of the pump energy by the seed, but increasing the density resulted in more pump depletion. Because this density scan was done to encompass the phenomenon of wavebreaking in a 200 eV rather than a cold plasma they were able to extract an optimal density for amplification to be  $2.5 \times 10^{19} \text{ cm}^{-3}$ , at which the intensity amplification of close to 100. In addition to observing high amplification, they also verified that the seed cannot grow indefinitely and mechanisms such as forward Raman scattering and modulational instabilities can cause the seed to break apart above a certain threshold intensity. To quantify this they plotted snapshots of the Fourier transform of the seed at various times and pointed out the spectral peaks that were indicative of these instabilities, giving valuable insight into the changing character of instabilities

and kinetic effects.

The work by P. Mardahl et. al. at UC Berkeley reported initial results of 2D PIC simulations using the code XOOPIC [17] which has a moving simulation window containing the seed laser. In their model the pump laser is an infinite plane wave boundary condition that emerges from the side of the window that the seed propagates towards. At each time step, slabs of plasma enter the window simultaneously with pump and the plasma electrons in each slab are set to oscillate self-consistently inside the pump field. By using a moving window they were able to reduce the computation time since the entire plasma did not have to be contained in the window itself. The physical problem that they studied was BRA using a parabolic plasma density channel with on-axis density of  $1 \times 10^{19} \text{ cm}^{-3}$ , where the seed pulse is guided over a distance larger than its diffraction length. The seed pulse they simulated had a diameter of  $4 \mu\text{m}$  FWHM, which normally has a Rayleigh length of  $Z_R = 12 \mu\text{m}$ , but using a density channel they could guide it over 1 mm of plasma. The initial seed intensity was  $2.1 \times 10^{15} \text{ W/cm}^2$  in a 50 fs pulse and the pump intensity had a nominal value of  $2.8 \times 10^{15} \text{ W/cm}^2$ . With the increased interaction length they obtained an intensity amplification of almost 200 as the best case when the channel diameter was matched to the seed spot size. However they observed less than 10% pump depletion and no compression of the seed pulse. It should be noted that they simulated a cold plasma but did not have electron-ion collisions in their code, so both particle trapping and collisional absorption were neglected in their simulations.

The work by R. Trines et. al. at Rutherford Appleton Laboratory [18] also studied 2D PIC simulations using the code XOOPIC with the moving window, but with a wide seed laser pulse of diameter  $300 \mu\text{m}$  and  $600 \mu\text{m}$  FWHM and a 50 fs pulsewidth. They argued that seed pulses having very small spot sizes may be affected by various transverse effects such as self-focusing and filamentation

when they get amplified, and that wide pulses should be studied with simulations. Taking advantage of the moving window capability they used a nominal pump intensity of  $1 \times 10^{15} \text{ W/cm}^2$  and an initial seed intensity of  $1 \times 10^{16} \text{ W/cm}^2$ . They also used a cold plasma but with density of  $4.3 \times 10^{18} \text{ cm}^{-3}$ . At this density the seed pulse diameter of  $300 \text{ }\mu\text{m}$  and  $600 \text{ }\mu\text{m}$  corresponds to  $117 c/\omega_p$  and  $234 c/\omega_p$  respectively. Upon running this simulation they observed an intensity amplification of 50 and pulse shortening down to 25 fs after propagating through 4 mm of plasma. This happened to be their best-case result since they found that for lower densities the energy transfer is inefficient and for higher densities the filamentation will destroy the seed. They also found that for pump intensities of order  $10^{14} \text{ W/cm}^2$  or less the seed will take a longer plasma length to amplify, allowing the plasma to distort its transverse profile. On the other hand for pump intensities of order  $10^{16} \text{ W/cm}^2$  or higher the pump itself will be modified by self-backscatter and filamentation inside the plasma. Therefore they emphasize the importance of finding the right combination of plasma density, pump intensity, and propagation distance for the purpose of maintaining the focusability of the wide seed and keeping a very low level of filamentation so high peak intensities can be reached.

As useful as simulations have been to the study of BRA, the freedom of choice in parameters that they allow usually leads to choices that are somewhat less realistic from an experimental perspective. Very narrow spot sizes or very wide spot sizes with ultrashort pulsewidths are considered extreme parameters to use at present, and realistic plasmas typically have a finite temperature. In addition using initial seed intensities that are comparable to or even an order of magnitude larger than the pump intensity to better induce pump depletion may be interesting for simulations but is perhaps not physically possible to create in a laboratory using current frequency downshifting methods. Therefore experi-

mental results are needed to provide a more realistic approach to understanding amplification.

### 1.2.2 Experiments

While the simulation results that we reviewed were wide-ranging in their parameter selection, experimental setups are more restrictive in that laser plasma interaction experiments are typically conducted using CPA laser systems. These laser systems are typically based on the Ti:Sapphire laser medium and provide intense laser pulses in the range of wavelengths around 800 nm. Therefore the results that we describe here come from plasma conditions that are similar to one another as are the laboratory setups. One aspect to note is that all the experiments make plasma from a hydrocarbon gas. We believe that their purpose for using these gases was to obtain a more uniform plasma density from the gas jets. But we should point out that hydrocarbon gases typically have low liquification pressures ( $< 100$  psi), which puts a maximum limit on the gas pressure that can be used. Furthermore at higher densities these gases can produce clusters which will detract from the uniformity of the plasma. Table 1.2 lists the relevant parameters and results from each experiment. Initial proof-of-principle experimental results of BRA in preformed plasmas were obtained by Y. Ping et. al. at Princeton [8]. In their setup, the pump and seed were both derived from the same 800 nm Ti:Sapphire laser system. The output pulse of that laser system was split into two pulses, with one being compressed down to 10 ps to act as the pump and the other being frequency doubled and sent into an optical parametric generator before compressing down to 500 fs to be the seed. Since the pump was 10 ps this meant that it was not fully compressed and had a residual chirp, and because of the manner in which the seed was created, the resulting output had

Table 1.2: Comparison of selected experimental work on BRA

Investigator	Y. Ping	W. Cheng	J. Ren	C. Pai
Pump wavelength (nm)	800	800	803	810
Pump pulsewidth (ps)	10	10	20	160
Pump intensity ( $W/cm^2$ )	$1.5 \times 10^{14}$	$1 \times 10^{14}$	$2.3 \times 10^{14}$	$1.5 \times 10^{15}$
Initial seed pulsewidth (fs)	500	550	500	38
Final seed pulsewidth (fs)	$\gtrsim 500$	150	50	$\gtrsim 38$
Seed spot size FWHM ( $\mu\text{m}$ )	30	$\lesssim 30$	$\lesssim 55$	14
Initial seed intensity ( $W/cm^2$ )	$1.5 \times 10^{11}$	$1.6 \times 10^{12}$	$1.3 \times 10^{12}$	$2.6 \times 10^{13}$
Final seed intensity ( $W/cm^2$ )	$1.4 \times 10^{12}$	$1.7 \times 10^{15}$	$4 \times 10^{16}$	$2.3 \times 10^{16}$
Plasma length (mm)	2	2	2	9
Plasma density ( $\text{cm}^{-3}$ )	$9 \times 10^{18}$	$1.1 \times 10^{19}$	$1.3 \times 10^{19}$	$5.9 \times 10^{18}$
Plasma temperature (eV)	$< 50$	$< 50$	$< 50$	150
Neutral gas	$C_3H_8$	$C_3H_8$	$C_2H_6$	$H_2$

a broadband spectrum extending from 840 to 940 nm. These were not ideal parameters for amplification based on a resonance effect but they were adequate for a first attempt at BRA. The pump energy was 15 to 20 mJ and the seed energy was 5 to 8  $\mu\text{J}$ . The plasma was created by optical breakdown of a 2 mm long  $C_3H_8$  gas jet using a separate 1.064  $\mu\text{m}$  laser pulse with 7 ns duration and the density was varied by changing the delay between this plasma-forming pulse and the pump and seed pulses. Because the seed was broadband the amplification was measured by taking the ratio of the amplified seed spectrum to a reference seed spectrum. Although they reported an intensity amplification of approximately 10, they did not find evidence of reaching the nonlinear pump depletion regime as the seed pulsewidth not only failed to compress, but also lengthened by a small amount.

Follow-on work by W. Cheng et. al. at Princeton [9] reported to have reached the nonlinear pump depletion regime by showing that the seed pulse simultaneously compressed as it underwent amplification. The setup was similar to the original experiment but the seed was made by sending a pulse through a Raman shifting crystal resulting in a 550 fs narrowband spectrum centered about 873 nm. The gas jet design was also modified to obtain a better plasma uniformity. The pump energy was 40 mJ and the initial seed energy was 7.5  $\mu\text{J}$ . Upon measuring a much higher amplification, they found the seed pulse to reach an intensity almost 1000 times above its initial intensity, and also an order of magnitude larger than the initial pump intensity. Because the amplified seed was more intense, they were able to take autocorrelator measurements to verify the shrinking of the pulsewidth by almost a factor of 4 as an indicator that the seed depleted a portion of the pump. In addition they observed narrowing of the seed spot size, which they believe was caused by the central part of the seed being amplified more than the edges. However one parameter that was not measured in these

experiments was the plasma temperature, which was assumed to be less than 50 eV. As we will show later in this thesis the plasma temperature is very important as it can cause the plasma to exhibit kinetic effects and affect the damping of the plasma wave.

The latest experiments by J. Ren et. al. at Princeton [10] found a way to increase the amplification in BRA experiments even further by setting up a novel double pass configuration in which both pump and seed pulses were reflected from end mirrors back into the plasma for a second round of amplification. Their concept was to reuse the leftover pump energy from the first pass in order to deplete more energy out of the pump on the subsequent pass to get higher gain. They modified the previous experiment by going back to a 500 fs narrowband seed centered at 878 nm and lengthening the pump pulsewidth to 20 ps. The pump energy was 87 mJ and the initial seed energy was 16  $\mu$ J. They also switched to using  $C_2H_6$  gas because they found it to provide even better uniformity in their plasma. The result of their double pass experiment was that the seed amplified to greater than 10000 times its initial intensity and two orders of magnitude above the initial pump intensity. They also measured shortening of the pulsewidth, by a factor of 5 on the first pass and then by an additional factor of 2 on the second pass, and supplemented this by observing broadening of the amplified seed spectrum compared to the original spectrum. The seed spot size was shown to narrow by almost a factor of 4. All indications seemed to imply more pump depletion, but once they quantified the amount of pump energy loss they found the depletion to be only slightly more than 6%, which was much lower than predicted by theory.

A separate research effort by C. Pai et. al. has investigated BRA in a plasma waveguide [11]. Their goal was to dramatically increase the energy transfer from the pump to the seed by extending the length of the resonance region. Their ex-

periment used an ignitor-heater scheme [19] with a hydrogen gas jet to make a 4 mm and later a 9 mm plasma waveguide with an axial density of  $5.9 \times 10^{18} \text{ cm}^{-3}$  to guide the pump and the seed laser pulses. They deduced their plasma temperature from hydrodynamic expansion calculations to be 150 eV. Their pump laser was at 810 nm and had an energy of 345 mJ. Their seed was created by taking a 38 fs, 810 nm laser pulse to form a supercontinuum in a krypton gas cell, resulting in a 0.8  $\mu\text{J}$  spectrum centered at 862 nm. Although their intensity gain was 1000 times above the initial seed intensity they did not detect any measurable pulse compression which led them to conclude that their amplification remained in the linear regime of BRA.

In reviewing the experimental results on BRA thus far it is apparent that finding ways to create the seed by wavelength shifting and making uniform density plasmas that are many  $Z_R$  long is likely to give large amplification factors. But demonstrating clear evidence of having reached the nonlinear pump depletion regime remains a difficult proposition. Measuring the amplification alone is necessary but not a sufficient proof of pump depletion. Even other clues such as the measurements of the changes to the spectral properties of the seed laser and pulse shortening of the seed cannot provide conclusive evidence of significant pump depletion. Thus while it is possible to take advantage of the fact that SRS naturally happens to make BRA work, it remains a challenging proposition to discover an optimal experimental setup to demonstrate this completely.

### 1.3 Purpose of this dissertation and outline

Having reviewed simulation and experimental results showing evidence of BRA and subsequent improvements on the amplification of short and ultrashort laser pulses, we took on the idea of scaling BRA to amplify picosecond-scale seed

pulses using a long nanosecond-scale pump pulse. New applications to inertial confinement fusion (ICF) and high energy density physics will arise if it's possible to successfully amplify a picosecond-scale laser pulse of sub-mJ energy by up to 10 orders of magnitude using a plasma. Also since the majority of laser pulsewidths at  $\lambda = 1 \mu\text{m}$  or  $0.8 \mu\text{m}$  are either  $> 1 \text{ ns}$  or  $< 1 \text{ ps}$ , it is indeed interesting to amplify a pulsewidth that falls in between those two ranges. Our research is a continuation of work initiated by R. Kirkwood et. al. at Lawrence Livermore National Laboratory (LLNL) [20], in which they took the first steps to setting up a BRA experiment where the seed pulse was typically a few ps long and the plasma parameters were such that  $k_2\lambda_D \sim 0.4$  to  $0.5$ . The purpose of our project is to conduct further studies towards the development of a nanosecond laser-pumped Raman amplification system for short laser pulses in what we classify as the strong damping regime ( $k_2\lambda_D \sim 0.4$  to  $0.5$ ) of an underdense thermal plasma, where the kinetic effects are thought to be critical in determining the ultimate amplification. We studied this from both simulation and experimental standpoints and we will discuss our work in more detail in the remaining chapters of this dissertation.

This dissertation is organized as follows. In Chapter 2 we first review a derivation of the three wave model for stimulated Raman scattering and discuss the approximations used in the limit of the strong damping regime. We then show how the three wave model reduces to a sine-Gordon equation and present its corresponding  $\pi$ -pulses solutions as a 1D model for BRA. We follow that with an outline of several plasma kinetic effects and multi-dimensional factors that can impact BRA before closing with a motivation for our selection of 1054 nm as the pump laser wavelength. In Chapter 3 we present our own 1D PIC simulation study of BRA using ultrashort seed pulses, expanding on earlier work by D. Clark by scanning a larger range of plasma densities and temperatures with

finer increments. The results obtained were from using a better resolved spatial grid and more simulation particles to incorporate the presence of particle trapping, thus providing a more accurate representation of kinetic effects in Raman amplification over a broad range of plasma conditions. Since neither the plasma density nor temperature can be precisely controlled in experiments, characterizing the variability of kinetic effects over a range of temperatures and densities is an important step toward optimizing the amplification, and we present a map of this parameter space that shows the best plasma conditions for amplification.

In Chapter 4 we cover the experiment we performed to generate a seed pulse by wavelength downshifting of 1054 nm light for our BRA experiment. In particular we describe the setup involving a Raman gas cell and the candidate gases that we evaluated for shifting the wavelength by molecular Raman scattering using excited vibrational and rotational levels of the neutral gas molecules. We also discuss the transient nature of Raman scattering in the context of converting picosecond laser pulses and mention possible reasons for why conversion into a broad rather than a narrow spectrum occurs in this regime.

In Chapter 5 we highlight the results of our seed amplification experiment for short and long seed pulses. We show from interferometry that our plasma density is not uniform (which is most likely due to non-uniform gas flow out of the gas jet) and describe our method of deducing the plasma temperature. We then show the process by which we determined the amplification from calorimeter energy and spectral measurements of the seed pulse before and after it amplifies. From these calculations we first make separate plots of output energy versus input energy for short and long seed pulse data points and then take all those points together to make one plot of output intensity versus input intensity to observe any intensity scaling of the amplification.

In Chapter 6 we revisit the use of simulations to extract possible insights into

our experiment and what may be happening to the laser beams as they amplify. We use both 1D PIC and a 2D fluid code pF3d to run the simulations. The pF3d runs let us specify 500  $\mu\text{m}$  laser diameters corresponding to our actual experimental spot sizes. In those runs we make the pump and seed cross each other at a shallow angle and incorporate a specialized optic called a phase plate on the pump beam in order to have more of a resemblance to the experiment. We also present further comparative simulations between 1D PIC and 2D pF3d models to show conditions under which both codes agree and disagree, and diagnose the impact of the phase plates in modifying the transverse intensity distribution of the amplified laser beams.

In Chapter 7 we conclude by giving a summary of our findings in this thesis and outlining possible ideas for future work. Our main finding from 1D PIC simulations of ultrashort seed pulses is that the situation in which the best energy amplification occurs happens when plasma conditions are not conducive to  $\pi$ -pulse formation, allowing most of the energy to be contained within just one peak of the seed without the seed developing a trail of decreasing amplitude spikes. Therefore we attempted to demonstrate amplification of a picosecond-scale seed pulse with a 1.054  $\mu\text{m}$  pump pulse in plasma conditions similar to those in the simulations. We found that it was challenging to make a narrow spectrum seed pulse at the desired resonant wavelength by Raman downshifting in a gas cell and that the conversion efficiency was less than 1%. Thus it was in our best interest to use  $N_2O$  gas in the cell to obtain a broad spectrum seed which assures us of hitting resonance at the expense of spectral energy at that particular wavelength. We attempted to amplify the seed we created throughout the course of many shots and ended up with only a few that showed clear evidence of amplification. One of the reasons for this was an inhomogeneous plasma being due to the non-uniformities in the gas jet. Although we obtained

amplification in spite of this, it is obvious that maximizing the amplification will require having a much more uniform plasma profile at the resonant density. In addition our plasma conditions were in the strong damping regime and the seed amplitude was not large enough to deplete the pump so we achieved only small amplification at each seed intensity that we tried. Upon looking for trends in the data we observed lower amplification for higher initial seed intensities, indicating a saturation of the amplification. As far as the seed quality is concerned, intense speckles in the pump beam coming from a RPP can give rise to local intensity modulations in the amplified seed profile, which shows that BRA can actually be sensitive to spatial intensity fluctuations of the laser beams. However if the seed interacts with the pump at an angle, it can encounter more speckle surface area in the pump thus providing an averaging effect over the speckles for a smoother output profile. All of these aspects can be seen from doing large-scale 2D fluid code simulations. While a PIC code can perform kinetic modeling of the plasma such as particle trapping and frequency shift of the plasma wave, large-scale multi-dimensional simulations are computationally intensive. On the other hand a 2D fluid code can simulate large-scale problems involving laser beams fairly quickly but it's based primarily on the linear theory of LPI and inevitably leaves out important physics if the plasma conditions are highly kinetic. Therefore drawing upon the capabilities of both types of codes is necessary to study aspects of BRA on different scale lengths and ultimately the success of amplifying a large  $500 \mu\text{m}$  FWHM laser beam will depend on guidance from simulations along with better understanding about phase plate dynamics.

## CHAPTER 2

# Stimulated Raman Scattering and Backward Raman Amplification (BRA) Physical Concepts

### 2.1 Derivation of the Three Wave Equations Describing Raman Scattering and Light Wave Coupling

Stimulated Raman scattering in a plasma is a three wave process involving a pump laser (denoted by subscript 0), a backscattered light wave (denoted by subscript 1), and an electrostatic plasma wave (denoted by subscript 2). In this chapter we will first derive the standard equations for this resonant three wave coupling in terms of the field envelopes of the three waves. Afterwards we will show, in a special limit, how these coupled equations can govern the BRA in the 1D case. In the steps that follow  $\omega_{pe}$  is the electron plasma frequency,  $\nu$  is the light wave damping rate,  $\nu_p$  is the plasma wave damping rate (which includes Landau and collisional damping), and  $v_{the}$  is the thermal velocity of a plasma with finite temperature.

When stimulated Raman scattering of a laser pulse takes place inside a plasma, the resonant growth of the backscattered light wave and the plasma wave in the context of the three wave model occurs for frequencies that satisfy

$$\omega_1^2 = \omega_{pe}^2 + c^2 k_1^2 \quad (2.1)$$

$$\omega_2^2 = \omega_{pe}^2 + 3v_{the}^2 k_2^2 \quad (2.2)$$

where equation (2.1) is the dispersion relation for an electromagnetic wave in a plasma and equation (2.2) is the dispersion relation for a plasma wave, also known as the Bohm-Gross dispersion relation for finite temperature plasmas. As the first step in this derivation we begin with Maxwell's equations for the propagation of two light waves with vector potentials  $\vec{A}_0$  and  $\vec{A}_1$  in a uniform plasma.

$$\left(\frac{\partial^2}{\partial t^2} - c^2 \nabla^2 + \omega_{pe}^2 + \nu \frac{\partial}{\partial t}\right) \vec{A}_0 = -\omega_{pe}^2 \frac{n}{n_0} \vec{A}_1 \quad (2.3)$$

$$\left(\frac{\partial^2}{\partial t^2} - c^2 \nabla^2 + \omega_{pe}^2 + \nu \frac{\partial}{\partial t}\right) \vec{A}_1 = -\omega_{pe}^2 \frac{n}{n_0} \vec{A}_0 \quad (2.4)$$

$$\left(\frac{\partial^2}{\partial t^2} - 3v_{the}^2 \nabla^2 + \omega_{pe}^2 + \nu_p \frac{\partial}{\partial t}\right) \frac{n}{n_0} = \frac{e^2}{m^2 c^2} \nabla^2 (\vec{A}_0 \cdot \vec{A}_1) \quad (2.5)$$

The light waves are subject to ponderomotive coupling via the driven plasma wave where  $n_0$  is the background plasma electron density and  $n$  is the first order perturbation. Considering the one dimensional backscatter geometry with linearly polarized light defined to be in the  $\hat{y}$  direction, the fields can be decomposed into amplitudes and phases according to

$$\vec{A}_0 = \hat{y} \left(\frac{mc^2}{2|e|}\right) a_0(x, t) e^{i(k_0 x - \omega_0 t)} + c.c. \quad (2.6)$$

$$\vec{A}_1 = \hat{y} \left(\frac{mc^2}{2|e|}\right) a_1(x, t) e^{i(-k_1 x - \omega_1 t)} + c.c. \quad (2.7)$$

$$n = \hat{n}(x, t) e^{i(k_2 x - \omega_2 t)} + c.c. \quad (2.8)$$

We then define the longitudinal electric field normalization to be

$$\vec{E}_2 = -\hat{x} \frac{mc}{|e|} \frac{\sqrt{\omega_0 \omega_{pe}}}{2} a_2(x, t) e^{i(k_2 x - \omega_2 t)} + c.c. \quad (2.9)$$

and applying Gauss' Law we obtain the following expression

$$\frac{n}{n_0} = -\frac{\nabla \cdot \vec{E}_2}{4\pi |e| n_0} \simeq i \frac{ck_2}{2\omega_{pe}} \sqrt{\frac{\omega_0}{\omega_{pe}}} a_2(x, t) e^{i(k_2 x - \omega_2 t)} + c.c. \quad (2.10)$$

Applying the operators on the left hand side of equations (2.3), (2.4), and (2.5) and retaining only the first order derivatives of the amplitudes, we get

$$\left(\frac{\partial^2}{\partial t^2} - c^2 \nabla^2 + \nu \frac{\partial}{\partial t}\right) a_0 = [(c^2 k_0^2 - \omega_0^2) a_0 - 2i(\omega_0 \frac{\partial}{\partial t} a_0 + c^2 k_0 \frac{\partial}{\partial x} a_0) + \nu(-i\omega_0 + \frac{\partial}{\partial t} a_0)] \quad (2.11)$$

$$\left(\frac{\partial^2}{\partial t^2} - c^2 \nabla^2 + \nu \frac{\partial}{\partial t}\right) a_1 = [(c^2 k_1^2 - \omega_1^2) a_1 - 2i(\omega_1 \frac{\partial}{\partial t} a_1 + c^2 k_1 \frac{\partial}{\partial x} a_1) + \nu(-i\omega_1 + \frac{\partial}{\partial t} a_1)] \quad (2.12)$$

$$\left(\frac{\partial^2}{\partial t^2} + \nu_p \frac{\partial}{\partial t}\right) a_2 = [-(2i(\omega_2 \frac{\partial}{\partial t} a_2 + \omega_2^2 a_2) + \nu_p(-i\omega_2 + \frac{\partial}{\partial t} a_2))] \quad (2.13)$$

where we have factored out the eikonal terms  $e^{i(k_i x - \omega_i t)}$ .

A further assumption will be to neglect non-resonant terms and terms of the form  $\nu \frac{\partial}{\partial t} a_i$  as being of higher order, and this reduces equations (2.11), (2.12), and (2.13) into the following format

$$\frac{i}{2} \sqrt{\omega_0 \omega_{pe}} c k_2 a_1 a_2 = (\omega_{pe}^2 + c^2 k_0^2 - \omega_0^2 - i\nu \omega_0) a_0 - 2i(\omega_0 \frac{\partial}{\partial t} a_0 + c^2 k_0 \frac{\partial}{\partial x} a_0) \quad (2.14)$$

$$-\frac{i}{2} \sqrt{\omega_0 \omega_{pe}} c k_2 a_0 a_2^* = (\omega_{pe}^2 + c^2 k_1^2 - \omega_1^2 - i\nu \omega_1) a_1 - 2i(\omega_1 \frac{\partial}{\partial t} a_1 + c^2 k_1 \frac{\partial}{\partial x} a_1) \quad (2.15)$$

$$-\frac{i}{2} \sqrt{\omega_0 \omega_{pe}} c k_2 a_0 a_1^* = (\omega_{pe}^2 - \omega_2^2 - i\nu_p \omega_2) a_2 - 2i\omega_2 \frac{\partial}{\partial t} a_2 \quad (2.16)$$

The last step in deriving the three wave equations in terms of field envelopes is to use the approximate linear dispersion relations for each mode:  $ck_{0,1} \simeq \omega_{0,1} \simeq \omega$  and  $ck_2 = c(k_0 + k_1) \simeq 2\omega$  along with  $\omega_2 \simeq \omega_{pe} - \delta\omega$ , where  $\delta\omega \ll \omega_{pe}$ . Finally upon substitution, equations (2.14), (2.15), and (2.16) become the final coupled three wave equations in terms of field envelopes [21].

$$\left(\frac{\partial}{\partial t} - c \frac{\partial}{\partial x} + \nu\right) a_0 = \frac{\sqrt{\omega \omega_{pe}}}{2} a_1 a_2 \quad (2.17)$$

$$\left(\frac{\partial}{\partial t} + c \frac{\partial}{\partial x} + \nu\right) a_1 = -\frac{\sqrt{\omega \omega_{pe}}}{2} a_0 a_2^* \quad (2.18)$$

$$\left(\frac{\partial}{\partial t} + \nu_p - i\delta\omega\right) a_2 = -\frac{\sqrt{\omega \omega_{pe}}}{2} a_0 a_1^* \quad (2.19)$$

After this reduction of Maxwell's equations into the three wave equations modeling light waves coupled by a Langmuir wave, we can define the coupling constant  $K = \frac{\sqrt{\omega\omega_{pe}}}{2}$  for linearly polarized light and the linear temporal Raman growth rate  $\gamma_R = Ka_0$ . In the limit of the strong damping approximation [22], where the damping term dominates over the time and the convective derivatives (i.e.  $\nu_p \gg \frac{\partial}{\partial t}$  and  $\nu_p \gg c\frac{\partial}{\partial x}$ ), the equation modeling the envelope of the plasma wave becomes  $a_2 \simeq \frac{\gamma_R}{\nu_p}a_1$ . Furthermore, since there is negligible pump depletion in the strong damping regime the e-folding growth of the intensity goes as  $e^{\gamma_R(\frac{\gamma_R}{\nu_p})t}$  where  $\frac{\gamma_R}{\nu_p} \ll 1$ .

When it comes to BRA, the process actually requires a finite amount of damping in the plasma wave. If this were not the case and the plasma wave did not damp, the energy initially transferred from the pump to the seed will end up returning back to the pump, and this back and forth process will continue until the seed exits the pump or the plasma. As we will show in the next section the one dimensional theory developed for BRA in cold plasmas predicts that the seed pulse will amplify and evolve into what is called a  $\pi$ -pulse structure. This structure is comprised of a train of peaks with the leading peak arising from the amplified seed pulse and the trailing peaks developing as a consequence of the back and forth energy transfer. When there is a small amount of damping in the plasma wave, the trailing peaks get progressively smaller and smaller behind the first peak. When the wave experiences strong damping, it will only have a sizeable amplitude in the local overlap region between the pump and seed. Because it is sufficiently damped it does not have much of a presence in the part of the plasma behind the seed and won't transfer enough energy back to the pump for the trailing peaks to grow by much.

Typical conditions under which strong damping can occur is when the plasma has high temperatures for a given density. In those cases the Landau damping

rate can be comparable to or larger than the linear Raman growth rate. An important dimensionless parameter used in classifying plasma response is  $k_2\lambda_D$ , where  $k_2$  is the wavenumber of the plasma wave and  $\lambda_D$  is the Debye length of the plasma, which is a measure of a plasma's ability to shield out electrostatic potentials. Since  $\lambda_D = \frac{v_{the}}{\omega_{pe}}$ , the parameter  $k_2\lambda_D$  increases with increasing plasma temperature and decreases with increasing plasma density. Thus it can serve as a metric that categorizes the transition from the fluid to the kinetic regime of plasma behavior. When  $k_2\lambda_D < 0.3$ , wave-wave or fluid interactions are prominent and the phase velocity  $v_\phi$  of the plasma wave is much larger than the plasma's thermal velocity. When  $k_2\lambda_D \geq 0.3$ , wave-particle or kinetic interactions are prominent and the phase velocity is closer to the bulk of the distribution function [23]. Typically higher densities and lower temperatures correspond to the fluid regime and lower densities and higher temperatures correspond to the kinetic regime. It is interesting to show amplification in the strong damping regime for the purposes of transferring energy to the front portion of the seed without too much wasteful energy transfer to the trailing structures. In this case the goal will not be to deplete a majority of the pump energy and get compression of seed in an attempt at achieving high peak intensities. Although technically the term BRA refers to cases when the seed amplifies to several times the initial pump intensity, in the strong damping that is not the case. Thus we could think of it as just seed amplification but with the output seed intensity being at least an order of magnitude smaller than the pump, accompanied by very small amounts of pump depletion. Nevertheless it behooves us to have a basic understanding of what the 1D BRA theory predicts.

## 2.2 Theory behind the BRA process

The coupled mode equations that we derived for SRS in the previous section is a system of linear partial differential equations in one dimension. This same model captures the main aspects of BRA, which is based on the resonant three wave coupling of the pump, the seed, and the plasma wave. The seed should be at least 100 plasma periods wide for the one dimensional three wave model for BRA to be valid. It cannot be too short or else it will not amplify. The one dimensional theory developed for BRA in cold plasmas has BRA occurring in two regimes: the linear regime and the nonlinear regime. As the seed initially grows, it is classified as being in the linear amplification regime. In this regime there is negligible pump depletion by the seed. The seed amplitude grows exponentially with time while its pulsewidth broadens due to the fact that the bandwidth of the instability is limited by the Raman growth rate resulting in gain narrowing in frequency space. For no detuning the pulse shape in this regime can be analytically determined [24] and thought of as the peak of the pulse moving at speed  $c/2$  while its front moves at speed  $c$ . If the seed keeps growing to intensities above the initial pump intensity it will transition into the nonlinear amplification regime. In this regime there is substantial pump depletion by the seed. The seed growth becomes linear with time while its pulsewidth effectively shortens as its peak grows a lot faster than the front and rear parts of the pulse. This can be thought of as the phase of the peak position moving at a speed greater than  $c$  and overtaking the front. The fraction of energy transfer to the seed in this regime is governed by the Manley-Rowe relations which require photon number or wave action conservation. In other words photons from the higher frequency pump decay into photons of the lower frequency seed, and in principle the energy transfer efficiency is the ratio  $\omega_1/\omega_0$  since some quanta of pump energy goes to the plasma wave which is then

damped. Since the pump is depleted of its energy we can apply the quasi-static approximation to the coupled mode equations and look for a limiting case of those equations in order to solve them analytically.

Upon transforming the spatial coordinate into  $\xi = x/c + t$ , noting that we can neglect the time derivatives with respect to the  $\xi$ -derivatives, and considering the case of no detuning, the three wave equations can be reduced to a set of quasi-static three wave equations

$$2\frac{\partial}{\partial\xi}a_0 = Ka_0a_1 \quad (2.20)$$

$$\frac{\partial}{\partial t}a_1 = -Ka_0a_1^* \quad (2.21)$$

$$2\frac{\partial}{\partial\xi}a_2 = -Ka_0a_1^* \quad (2.22)$$

Then the following transformation [25]

$$\begin{pmatrix} a_0 \\ a_1 \\ a_2 \end{pmatrix} = \begin{pmatrix} a \cos(u/2) \\ -u_\xi/K\sqrt{2} \\ \sqrt{2}a \sin(u/2) \end{pmatrix}$$

reduces those quasi-static three wave equations to a single sine-Gordon equation for the function  $u(\xi, \tau)$

$$\frac{\partial^2 u}{\partial\xi\partial\tau} = \sin u \quad (2.23)$$

where  $\tau = a_0^2 K^2 t$ . The symmetry of the sine-Gordon equation in  $\xi$  and  $\tau$  suggests the existence of a self-similar solution of the form  $u(\xi, \tau) = u(\xi\tau)$ . As a further step, introducing a new variable  $z = 2\sqrt{\xi\tau}$  can transform the sine-Gordon equation into an ordinary differential equation

$$\frac{d^2}{dz^2}u + \frac{1}{z}\frac{d}{dz}u = \sin u \quad (2.24)$$

From numerical investigations into this solution [26] it was found that it rises from an initially small value and then oscillates about  $\pi$  as shown on the left

hand side of Figure 2.1. Therefore this solution of the sine-Gordon equation was referred to as a  $\pi$ -pulse and considered to be an attractor solution for certain initial conditions of the three wave equations [27]. Since the seed envelope is proportional to  $\frac{\partial u}{\partial \xi}$ , the dependence of  $u$  on the product of  $\xi$  and  $\tau$  results in both the narrowing and amplification of the seed pulse shape linearly with time. In other words the amplitude of the leading peak increases directly proportional to time and its width decreases inversely proportional to time. Because the seed envelope is related to the derivative of  $u$ , there is a train of secondary peaks of lower and lower amplitudes behind the leading peak. This can be better visualized by plotting the intensity waveform, which is obtained by squaring the electric field envelope. A normalized seed intensity waveform is shown on the right hand side of Figure 2.1. The physical explanation for the appearance of this structure is that as the seed amplifies and depletes the pump in the form of Stokes scattering, the reverse process also takes place in the form of anti-Stokes scattering of the seed (i.e. the amplified seed beats with plasma wave to regenerate the pump which results in depletion of the seed), and these alternating

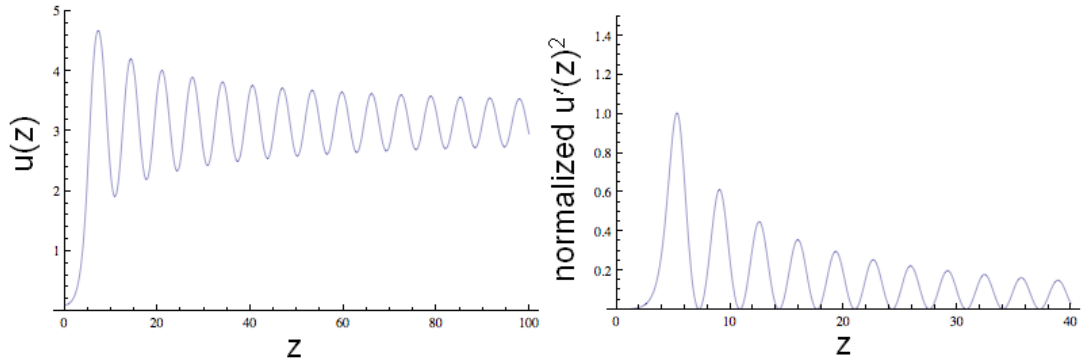


Figure 2.1: Mathematical plots of a  $\pi$ -pulse solution (left) and a normalized seed intensity waveform (right).

processes can repeat several times and result in the  $\pi$ -pulse structure as long as the plasma wave exists to mediate this effect.

The nonlinear pump depletion regime with its characteristic  $\pi$ -pulse solution can be accessed only if Landau damping is not significant. This is because the amplified pulse becomes short enough so that Landau damping cannot affect its amplification since the plasma wave cannot be damped in that short of a time. However we need to keep in mind that this picture of BRA which we described in this section comes from a one dimensional three wave model for a cold plasma. In reality, experimental plasmas have a finite temperature and, if sufficiently hot, can exhibit many kinetic effects. Furthermore there are also multi-dimensional effects that need to be taken into account such as the seed front quality and its focusability. We will discuss more of these aspects in the following sections.

### **2.3 Plasma wave dynamics and their impact on laser beams in BRA**

Perhaps the most important factor that can impact BRA and determine the amount of amplification is the dynamics of the driven plasma wave. There are various effects can impact the plasma wave growth and the overall BRA process. Landau damping, particle trapping and nonlinear frequency shift, and wavebreaking of the plasma wave are all important mechanisms that can have an impact on BRA. Therefore we need to consider these kinetic effects as well as other physical processes that can affect the laser pulses in order to complement what we know about the predictions of the three wave model.

Landau damping is a linear collisionless damping phenomenon that arises from the interplay between a plasma wave and plasma electrons that come into resonance with it [28]. It happens through the course of momentum exchange

between those electrons and the plasma wave, resulting in accelerated electrons at the phase velocity of the wave and a damping of the wave amplitude. Landau damping can occur more easily in plasmas with higher temperatures since there are more electrons that reside in the distribution function near the phase velocity. Strong Landau damping becomes important when the damping rate is larger than the linear Raman growth rate, and this is a valid picture if the behavior of the plasma wave stays linear. However the picture of Landau damping can become more complicated since a plasma wave driven near resonance can become steepened and plasma electrons can get trapped in its electrostatic potential troughs. The trapped electrons can oscillate at a characteristic bounce frequency  $\omega_b$  and if they bounce several times before the wave has a chance to damp, they will flatten the distribution function and nonlinearly reduce the Landau damping rate [30]. This happens because the plasma frequency will undergo a small nonlinear frequency downshift, proportional to the amplitude of the plasma wave, as a result of the particle trapping [31]. The plasma wave may then evolve into a BGK mode that experiences negligible damping and can last for long times [32]. This nonlinear decrease of the Landau damping may also cause the wave amplitude to be larger than that predicted by linear gain estimates, which leads to larger amounts of SRS. This has been observed in experimental measurements of laser intensity reflectivity [33] and has come to be known as kinetic inflation. On the other hand, its also possible that plasma wave nonlinearity could saturate the growth of SRS since the wave amplitude may saturate due to the detuning from ponderomotive resonance as a result of the frequency shift. Another point to mention is that the concept of Landau damping is valid only for small amplitude plasma waves. When plasma waves are very strongly driven the concept no longer applies [34]. Thus wide-ranging research has been done to study this unique kinetic behavior, with more recent work studying the growth, saturation,

and recurrence of plasma wavepackets transitioning from convective to absolute growth in the context of increasing laser intensity in LPI [35].

Wavebreaking is another phenomenon that can happen to a plasma wave in the event it traps a majority of the plasma electrons and those electrons begin to phase mix. At that point the wave loses its coherence and no longer has a well-defined amplitude and phase velocity. In cold plasmas, wavebreaking happens at a well-defined threshold amplitude. But in warm plasmas, wavebreaking occurs at a lower plasma wave amplitude by a scale factor  $(1 + 2\beta^{1/2} - \frac{8}{3}\beta^{1/4} - \frac{1}{3}\beta)^{1/2}$  where  $\beta = 3v_{the}^2/v_\phi^2$ . This scale factor was determined from assuming a waterbag distribution for the warm plasma [29]. However the transition into wavebreaking in thermal plasmas is not an abrupt process and cannot be strictly dictated by the waterbag model. It occurs in a gradual manner as more and more particles are grabbed by the plasma wave and their bounce frequency becomes greater than the plasma frequency. This can readily occur when the ratio  $v_\phi/v_{the}$  is on the order of 1, which can be the case when the plasma has some moderate temperature. Wavebreaking can also be observed as asymmetric heating of the electron distribution as electrons are swept out of the the plasma wave causing it to break.

Besides plasma wave dynamics the laser pulses themselves can experience some adverse effects when they propagate through a plasma on the way to being amplified. For plasmas with low temperatures, collisional damping or inverse bremsstrahlung absorption [36] could result in the seed losing some energy, making the net amplification lower. For plasmas in which absorption is not an issue other phenomena could manifest themselves such as self-focusing and filamentation [37, 38, 39], and temporal modulational instabilities [40, 41] of the seed. These instabilities in full force could very well degrade the output seed transverse quality and longitudinal structure, rendering the seed useless for practical pur-

poses. Finally for seeds that manage to bypass those effects relatively unscathed and amplify to high intensities, forward Raman scattering [42] of the seed could take place and create a large wake in the plasma which drains energy from the seed.

In spite of the various effects that can affect BRA, there are some guidelines that can be followed in the choice of plasma conditions and laser pulse properties that could make BRA successful. Optimal amplification requires a sufficiently low plasma density to delay the onset of the forward Raman instability of the seed, but a sufficiently high plasma density to avoid or approach the threshold of wavebreaking of the driven plasma wave. This comes from the 1D theory of BRA [4] which gives a scaling formula that predicts the ideal density for amplification being the density at which the driven plasma wave should barely break. In other words the plasma wave should be driven up to near its wavebreaking limit to get best amplification. Increasing the density further will actually accelerate the onset of instabilities. Wavebreaking will tend to suppress the secondary peaks of a  $\pi$ -pulse since the plasma wave behind the first peak will have smaller amplitudes when supporting the transfer of energy into trailing peaks. Finally the plasma should have a sufficiently low temperature to avoid strong Landau damping of the plasma wave, but also a sufficiently high temperature to avoid collisional damping of the light waves. If the plasma conditions somehow allow the amplified seed to reach the pump depletion regime, it is expected to shorten and acquire a larger bandwidth, thus making it less sensitive to nonlinear frequency shifts and even detuning from plasma density inhomogeneities. Therefore the BRA process can be quite lenient in that it does not require exact resonance to obtain finite amounts of amplification.

## 2.4 Multi-dimensional aspects of BRA

When considering BRA in multi-dimensions, important physics such as transverse structure of the seed wavefront and diffraction of the seed need to be taken into account as they may impact the focusability of the amplified seed pulse. The transverse properties of a seed pulse can cause its overall amplification pattern to deviate from the predictions of one dimensional theory. An amplified pulse with a relatively good quality phase front must emerge from the plasma in order to have a chance at being focused down to even higher intensities. Thus to take the next step towards establishing better predictions for experiments, two dimensional studies using finite and perhaps large spot sizes need to be performed to better understand if self-focusing and filamentation of the pump and seed may occur.

Initial simulation studies with 2D, three wave envelope codes have shown that amplitude modulations of the seed pulse in the transverse direction may be smoothed by the plasma if the seed reaches the pump depletion regime, and that BRA is rather insensitive to pump and seed spatial intensity fluctuations [43]. So to visualize what the seed could look like in multiple dimensions we can consider an ideal Gaussian pulse, which has the highest intensity in the center and the intensity falling off radially at the edges. For simplicity a 2D contour of the seed can be thought of as multiple 1D seed pulse profiles stacked side by side in the transverse direction. Then for the case of a  $\pi$ -pulse seed, each 1D slice would be a self-similar solution, and the end result is a structure that is most intense and compressed in the middle and less intense and stretched out at the edges. This is reasonable because the wings of the seed, being less intense to begin with, experience delayed growth from accessing the pump depletion regime later in time, if at all. The most amplification occurs at the center of the seed and the  $\pi$ -pulse is more pronounced since the pump is mostly depleted there. For better

visualization, Figure 2.2 gives a multi-dimensional representation of a  $\pi$ -pulse created from a pre-focused seed. A pre-focused seed guarantees a large intensity in the center and the result is a structure that looks like a horseshoe. However we also need to consider the fact that random plasma density inhomogeneities may defocus the seed pulses [44], and thus the horseshoe shape is an ideal case. Nonetheless this picture of an idealized amplified seed provides a baseline from which we can proceed to study BRA in a realistic multi-dimensional setting.

## 2.5 Motivation for choosing 1054 nm as the pump wavelength

In BRA the seed wavelength to be amplified determines the range of pump wavelengths that can be used depending on the range of plasma densities that can be produced. In our case we first chose 1054 nm as the pump, the reason being that this was one of the earlier  $1\omega$  wavelengths conceived for lasers driving ICF [45],

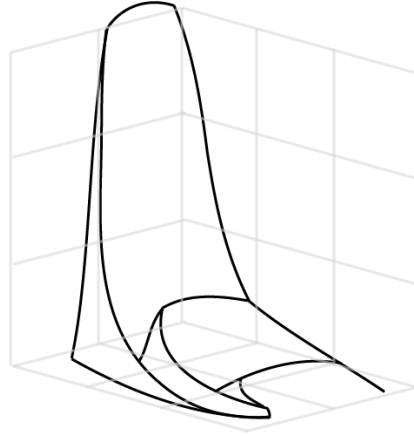


Figure 2.2: Multi-dimensional representation of a  $\pi$ -pulse solution from a pre-focused seed.

and because of its relation to potential ICF experiments at the National Ignition Facility (NIF) [46] at LLNL. NIF, the world's largest and most energetic laser, consists of 192 beams that will illuminate a target called the hohlraum in an attempt at creating fusion burn from the capsule containing deuterium-tritium fuel inside. These drive beams are created and amplified at 1054 nm but get frequency tripled to  $3\omega$  or 351 nm in their final stage so that their normalized intensity will not give rise to intense LPI. But this is not to rule out that the  $1\omega$  wavelength, or adjacent wavelengths in that range, could one day be used to drive fusion, and thus studying BRA at 1054 nm is very worthwhile.

In the indirect-drive configuration for NIF [47], efficient conversion of laser energy into x-rays inside a hohlraum requires that laser beams propagate relatively undisturbed to its walls. However low-density plasma blowoff from those walls during the laser drive which can exit through the hohlraum's laser entrance hole (LEH) and create underdense plasma conditions that are ripe for a variety of LPI instabilities such as SRS. In this sense the conditions are similar to that of a Raman amplifier, and as we mentioned in Chapter 1 the seed in BRA can be thought of as a burst of backscattered SRS light. Figure 2.3 shows cartoon images depicting SRS occurring near a LEH and a possible analogy in the form of our Janus experiment that we will discuss in later chapters of this thesis. Another example that we can reference in regards to Raman amplification in ICF conditions are the studies of crossed beam energy transfer in experiments using a gas-filled, pre-heated 2 mm gas bag target in which the plasma waves are strongly damped [48]. In those experiments the beating of nanosecond 351 nm pump and 527 nm seed lasers generated a plasma wave to scatter energy from the pump to the seed. The results showed significant amplification of weak seeds and saturation of the scattered energy as the seed beam amplitude was increased. Simulations later confirmed that saturation could be due to electron kinetic ef-

Table 2.1: Comparison of typical NIF LEH and Gas Bag experiment parameters to the Janus experiment

Parameters	Pump wavelength (nm)	Density ( $n_{cr}$ )	Temperature (keV)	$k_2\lambda_D$
NIF LEH [47]	351	0.1	4-6	0.4-0.5
Gas Bag [48]	351	0.071	2.6	0.4
Janus	1054	0.008	0.28-0.3	0.4-0.5

fects such as trapping that are effective at higher  $k_2\lambda_D$  and can cause nonlinear saturation of the plasma wave.

Table 2.1 provides a comparison of typical NIF LEH and gas bag experiment parameters to the ones in the Janus experiment. Although the pump wavelength, density, and temperature are not the same, the  $k_2\lambda_D$  is very similar among all three cases. Because of the similarity in this one parameter, it is possible that we may observe the same type of behavior, namely the nonlinear saturation of

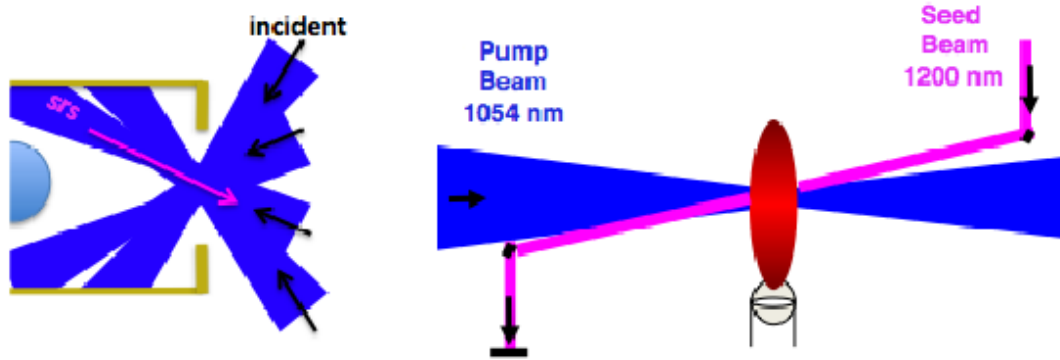


Figure 2.3: Cartoon drawing showing re-amplified SRS from a LEH (left) and the Janus experiment (right) which has pump and seed lasers interacting in a plasma made from a gas jet.

the amplification. Thus we studied the energy transfer from a 1054 nm nanosecond laser to a 1200-1300 nm picosecond-scale laser in a thermal plasma and made amplification measurements of those seeds to survey the possibility of electron kinetic saturation of re-amplified backscattered light in a strongly damped plasma. Our objective was practically different from BRA because we wanted to see how much energy we could transfer rather than to aim for high peak intensities in the seed.

## CHAPTER 3

# 1D OSIRIS Simulations of Ultrashort Pulse Backward Raman Amplification (BRA)

### 3.1 Case studies of ultrashort pulse amplification

Particle-In-Cell (PIC) codes are a very important simulation tool in basic plasma physics research [49]. Their ability to numerically model and simulate the kinetic behavior of plasmas when interacted upon by laser pulses has been a valuable asset in the studies of plasma phenomena in the kinetic regime. PIC codes construct a plasma numerically as a system of macroparticles placed in various regions on a grid and evolves their motions self-consistently in response to prescribed driving forces. They are based on the least amount of assumptions and are the state-of-the-art in simulating plasma kinetic behavior, incorporating advanced numerical techniques to make them robust to noise. In this chapter we report our PIC studies of ultrashort pulse amplification. For the 1D BRA scenario that we considered, we used a pump laser of wavelength  $1.064 \mu\text{m}$  and a normalized vector potential of  $a_0 = 0.015$ . Although our selection of pump wavelength and plasma density and temperature conditions over which to perform this PIC study was motivated by results from recent experimental efforts using a  $1.054 \mu\text{m}$  pump beam [20], we chose  $1.064 \mu\text{m}$  in order to be consistent with previous PIC simulation work [15]. Some of the results that we report here have been published in

a recent paper [50].

According to the 1D BRA theory [4], specifying the wavelength and amplitude of the pump beam determines all of the parameters for optimal operation of a Raman amplifier in a cold plasma. Calculation of those scaling formulas for  $\lambda = 1.064 \mu\text{m}$  and  $a_0 = 0.015$  yields  $n_e/n_{cr} \sim (2\sqrt{2}a_0)^{4/3} = 0.015$  as the optimal density for amplification,  $a_1 \sim 1.7a_0^{1/3} = 0.4$  as the estimate of the final seed amplitude, and  $I \sim [4 \times 10^{18} a_0^{2/3}] / \lambda^2 = 2 \times 10^{17} \text{ W/cm}^2$  for the final seed intensity. Because these predictions were made for cold underdense plasmas in the context of a three wave model, the next logical step was to run a PIC code and scan the plasma density and temperature to measure the amount of amplification for each case. From theoretical considerations we expect that optimal amplification requires a sufficiently low plasma density to delay the onset of the forward Raman instability of the seed, but a sufficiently high plasma density to avoid wavebreaking of the driven plasma wave (see Figure 3.15). In conjunction with that requirement the plasma should have a sufficiently low temperature to avoid strong Landau damping, but also a sufficiently high temperature to avoid collisional damping of the driven plasma wave. Furthermore the three wave model and corresponding  $\pi$ -pulse solution also require the amplifying seed to be ultrashort in order to have a sharp rise in its front. If the seed is too long the slow-rising front will interact with the pump to create precursor plasma waves before the arrival of the main peak of the seed, thus disrupting the amplification process as shown in the work by Tsidulko [51]. Because of this we chose for our ultrashort Gaussian seed pulse a nominal pulse width of 100 fs FWHM.

The fully kinetic PIC code OSIRIS [52] was used to run 1D simulations of BRA that survey different plasma densities  $n_e$  and temperatures  $T_e$  for a uniform plasma of length 4 mm given a pump wavelength of  $1.064 \mu\text{m}$  and normalized vector potential of  $a_0 = 0.015$ . In the simulations the density is scanned from

0.005  $n_{cr}$  to 0.05  $n_{cr}$  in increments of 0.005  $n_{cr}$ , where  $n_{cr} = 9.86 \times 10^{20} \text{ cm}^{-3}$  for a 1.064  $\mu\text{m}$  pump, and the temperature ranges from 50 eV to 500 eV in increments of 50 eV. In the setup the uniform density plasma is a step profile with vacuum regions on both sides. The 1.064  $\mu\text{m}$  pump laser moves from right to left in the simulation box while the seed laser moves from left to right. The long pump pulse is modeled by a 100 fs rise followed by a 26.64 ps flat top, and then a 100 fs fall. The Gaussian seed pulse is also chosen to have  $a_0 = 0.015$ , and a pulsewidth of 100 fs FWHM. The simulation box size is 25481.39  $c/\omega_0$  and contains 240000 cells with 256 particles per cell. Length units are normalized to  $c/\omega_0$  (0.1693  $\mu\text{m}$ ) and time units are normalized to  $\omega_0^{-1}$  (0.5645 fs) of the 1.064  $\mu\text{m}$  pump laser. The time step used is 0.1061  $\omega_0^{-1}$  (0.06 fs) and the total simulation time is 50029.27  $\omega_0^{-1}$  (28.2 ps). The cell size is 0.1061  $c/\omega_0$  corresponding to 60 cells per pump laser wavelength. Both lasers are linearly polarized parallel to each other and only the electrons are allowed to move, with the ions serving as a fixed neutralizing background. Starting with the pump wavelength, for each density and temperature, the seed wavelength is chosen to match the resonance condition for Raman backscatter. This was accomplished by running a series of simulations in which the pump interacted with the plasma alone to produce spontaneous backscatter noise. Measuring the peak  $k$  component of that noise for each case yielded the resonant  $k$  vector which was then assigned to the seed laser for the full BRA simulation. The following sub-sections compare and contrast simulations from four selected case studies.

### 3.1.1 Case I

$$n_e = 0.05 n_{cr}, \omega_0/\omega_{pe} = 4.5$$

$$T_e = 50 \text{ eV}, k_2\lambda_D = 0.076, \text{ seed } \lambda = 1.376 \mu\text{m}$$

The six panels on the left of Figure 3.1 show the amplification of the seed at various times during the simulation. The seed (green) travels from left to right and the pump (red) travels from right to left. The electrostatic plasma wave (magenta) appears where the seed and the pump overlap. The first panel shown is at time 14.1 ps because the pump is given time to cross the entire plasma before intersecting the seed at the left edge of the plasma where the peak of the seed and the beginning of the plateau of the pump overlap. Subsequent frames are plotted in a fixed width window that shifts with the motion of the seed. The plasma is present in the simulation until 28.2 ps when the seed exits into the vacuum region. Observing the progression of the seed we see that it first broadens as it grows. Once it begins to deplete the pump (which happens relatively early in time) it compresses as it amplifies and exhibits a  $\pi$ -pulse structure. The amplification continues until 18.9 ps, which is when the onset of Raman forward scatter (RFS) occurs. As shown in previous PIC simulation results the seed does not amplify indefinitely due to the development of effects such as RFS/wake generation, Raman back scatter (RBS), and frequency modulation [15]. As the seed undergoes RFS it begins to go unstable with the appearance of new k vector components that contribute to its distortion. The two larger panels on the right side of the figure shows the k spectrum at early and late times in order to identify the kinetic features that appear during the amplification process. The onset of RFS is detected when the peak corresponding to the seed wake appears, which in this case starts at 18.9 ps, and subsequently grows in the latter part of the simulation. This is accompanied by the growth of the seed RFS wave vector in the spectrum. The location of the other peaks in the spectrum corresponding to the seed, seed RBS, and plasma wave follow from the k-matching conditions. Figure 3.2 shows the Wigner transform of the seed at three different times. Making a Wigner transform plot allows us to visualize the positions of different k

components of a laser pulse in space. Initially at 14.1 ps the seed shows one primary  $k$  component,  $k = 0.7734 k_0$ . At 18.9 ps, after the  $\pi$ -pulse has formed during amplification, the seed still maintains that  $k$  value. But towards the end at 28.2 ps, we see that sections of the seed have broken off from the initial seed indicating that the amplification became unstable. We attribute the timing of the appearance of these redshifted  $k$  components in the rear of the seed to be the time the seed first created a wake as a result of RFS. To show this in more

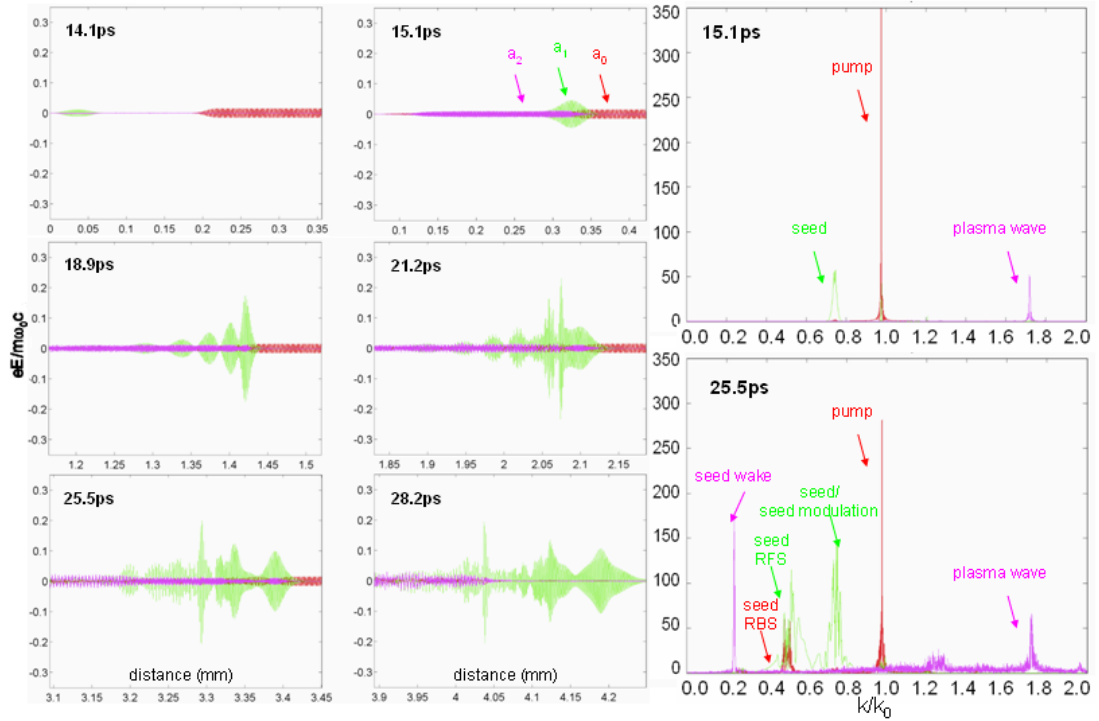


Figure 3.1: Case I - Snapshots of the seed at various times during amplification (left panels) and  $k$  spectrum of the pump, seed, and electrostatic waves (right panels). Reprinted with permission from T.-L. Wang, D. S. Clark, D. J. Strozzi, S. C. Wilks, S. F. Martins, and R. K. Kirkwood, Phys. Plasmas **17**, 023109 (2010). Copyright 2010, American Institute of Physics.

detail we refer to Figure 3.3, which basically replots the seed in Figure 3.1 but with a color scheme that assigns different colors to different  $k$  intervals. This was obtained by taking the Fourier transform of the seed waveform, isolating the different portions of the  $k$  spectrum by zeroing the other  $k$ 's, assigning a color to each portion, and then taking the inverse Fourier transform to obtain the seed waveform showing where the different  $k$ 's are located in the seed. Although this procedure does not reproduce exactly the original waveform, it does retain the majority of its features and gives the added clarity of the  $k$  components that are present in the seed. This is shown by the top two panels where the navy blue and the light blue colors correspond to the intervals  $0.3 \leq k \leq 0.5$  and  $0.5$

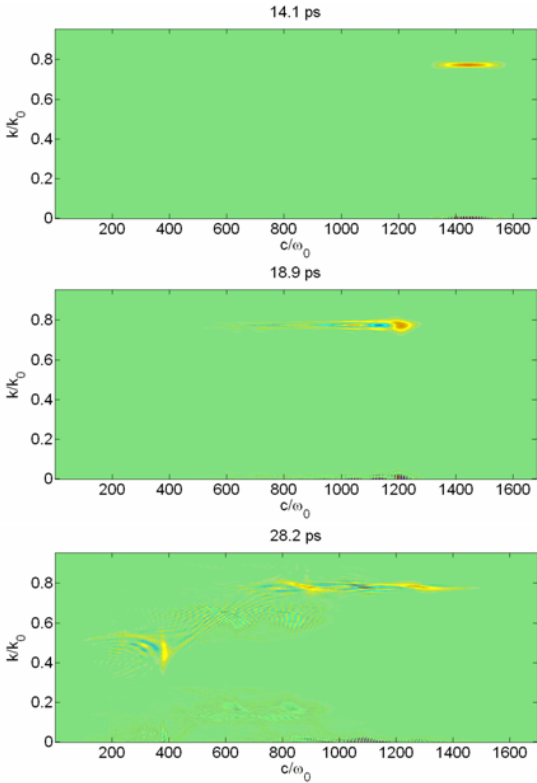


Figure 3.2: Wigner transform of the seed pulse undergoing amplification for Case I.

$\leq k \leq 0.7$  respectively. The bottom four panels show sequential snapshots of initial seed growth to  $\pi$ -pulse formation and then to seed break-up and wake creation. The color-coding allows us to distinguish between the driven plasma wave (purple) and the wake made by the amplified seed (black) so the panels were plotted to show the seed in the entire 4 mm simulation box rather than a zoomed-in window in order to point out these features. Figure 3.4 shows the phase space features associated with the behavior of the plasma particles during the amplification process. To support the interpretation of these features we calculated the relevant quantities for our parameter set, namely phase velocity  $v_\phi/c = 0.13$ , thermal velocity  $v_{the}/c = 0.00988$ ,  $v_\phi/v_{the} = 13.2$ , trapping width  $v_T/c = (2\omega_b/k_2)/c = 0.165$ . For this case the plasma frequency is  $\omega_{pe} = 3.96 \times 10^{14} \text{ s}^{-1}$ , the wave vector of the plasma wave is  $k_2 = 1.01 \times 10^7 \text{ m}^{-1}$ , the Raman growth rate of the pump is  $\gamma_R = 6.1 \times 10^{12} \text{ s}^{-1}$ , and the Landau damping rate is  $\nu_L =$

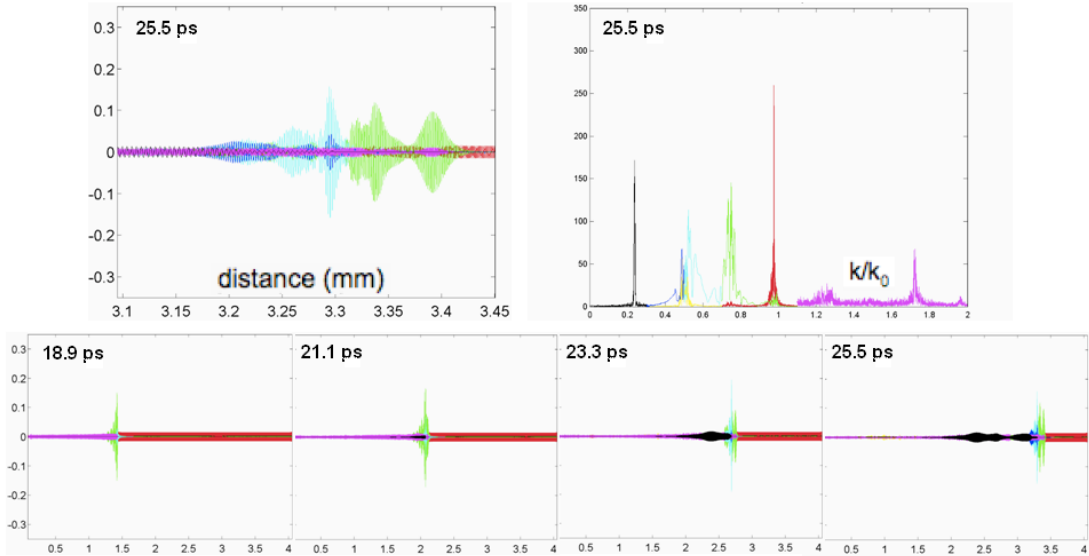


Figure 3.3: Case I - Color scheme representation of the seed waveform. The bottom row shows zoomed-out snapshots of the seed waveform in the entire box.

$-1.91 \times 10^{-21} \text{ s}^{-1}$  [1]. From the simulation the plasma wave grows to an amplitude of  $eE/m\omega_0c = 0.01$ , which gives an estimated bounce frequency of  $\omega_b = 2.5 \times 10^{14} \text{ s}^{-1}$ . From these calculations we find that the ordering of quantities goes as  $\omega_{pe} \geq \omega_b \gg \gamma_R \gg \nu_L$ . From the phase space plot only a tiny fraction of particles are trapped in the plasma wave. Although the distribution is sheared the majority of the bulk particles avoid getting trapped, which is expected since the ratio of  $v_\phi$  to  $v_{the}$  is large. In addition we note that the periodicity of the phase space structures are almost identical within each trailing peak of the seed while the distribution is a thermal Maxwellian in the region in front of the seed. The plasma wave in the seed-pump interaction region maintains most of its amplitude behind the seed, which enables the formation of visible trailing peaks in the  $\pi$ -pulse as the pump and seed interchange energy with one another. Because  $k_2\lambda_D = 0.076$  puts the plasma conditions in the fluid regime, the appearance of a clear  $\pi$ -pulse is consistent with the predictions of the three wave model. Since  $\nu_L$  is negligible in comparison with the other quantities the plasma wave, being strongly driven, does not damp towards its rear and can thus support this exchange of energy. To better visualize the plasma wave in Figure 3.4, we have filtered out the non-resonant wave vector components and plotted the result on top of the initial unfiltered plasma wave.

### 3.1.2 Case II

$$n_e = 0.035 n_{cr}, \omega_0/\omega_{pe} = 5.3$$

$$T_e = 200 \text{ eV}, k_2\lambda_D = 0.186, \text{ seed } \lambda = 1.323 \text{ } \mu\text{m}$$

The six panels on the left of Figure 3.5 show the amplification of the seed at various times during the simulation. The plasma is present in the simulation until 28.2 ps when the seed leaves into the vacuum region. As compared to the

seed in Case I the seed in this case depletes the pump by a lesser amount and the  $\pi$ -pulse structure develops fewer trailing peaks. The amplification continues until 21.2 ps, which is when the onset of RFS occurs. As with Case I effects such as RFS/wake generation, RBS, and frequency modulation appear. The two larger panels on the right side of the figure plot the k spectrum [at early and late

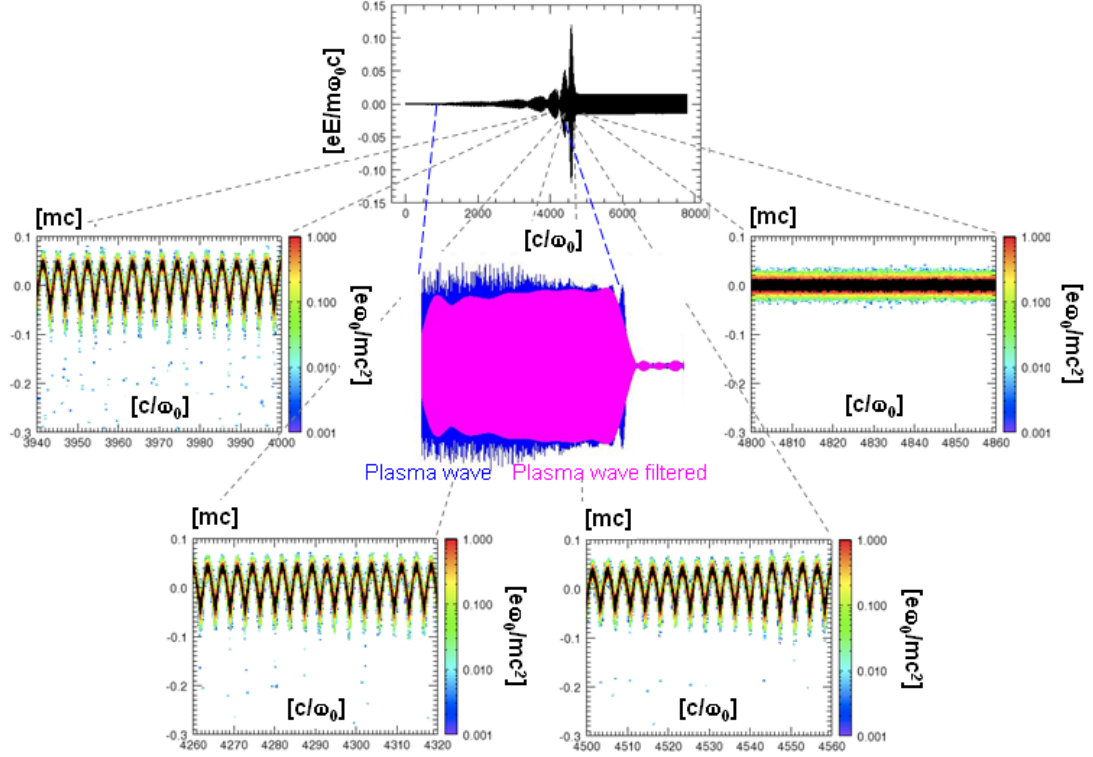


Figure 3.4: Case I - Phase space features at different locations inside the seed pulse. The center image shows the plasma wave with amplitude  $a_2 = eE_2/m\omega_0 c = 0.01$ . Non-resonant wave vector components have been filtered out and shown with the initial unfiltered plasma wave. Reprinted with permission from T.-L. Wang, D. S. Clark, D. J. Strozzi, S. C. Wilks, S. F. Martins, and R. K. Kirkwood, Phys. Plasmas **17**, 023109 (2010). Copyright 2010, American Institute of Physics.

times. Again the onset of RFS is detected when the peak corresponding to the seed wake appears, which in this case starts at 21.2 ps, and subsequently grows in the latter part of the simulation. Figure 3.6 shows the Wigner transform. The primary  $k$  component of the seed is  $k = 0.8044 k_0$  at 14.1 ps. At 18.9 ps, after the partial  $\pi$ -pulse has formed with one trailing peak, the seed still maintains that  $k$  value. This time towards the end at 28.2 ps, the sectioning of the seed due to break-up of the initial seed is not as pronounced and there is not as much

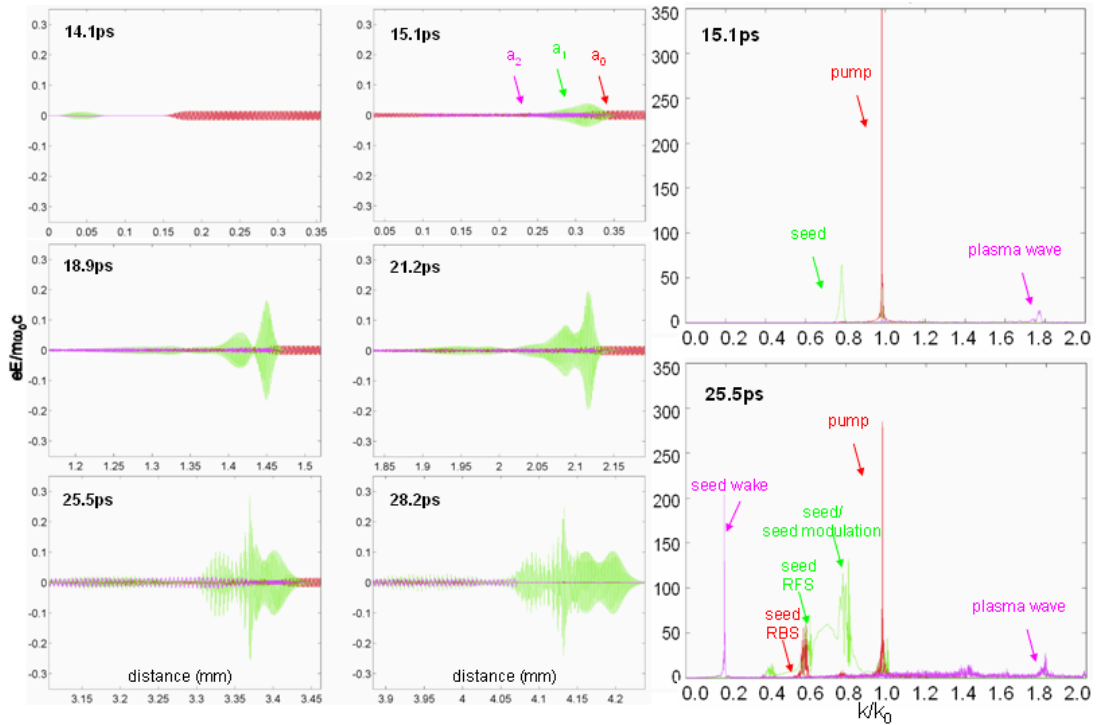


Figure 3.5: Case II - Snapshots of the seed at various times during amplification (left panels) and  $k$  spectrum of the pump, seed, and electrostatic waves (right panels). Reprinted with permission from T.-L. Wang, D. S. Clark, D. J. Strozzi, S. C. Wilks, S. F. Martins, and R. K. Kirkwood, Phys. Plasmas **17**, 023109 (2010). Copyright 2010, American Institute of Physics.

redshift in the rear of the seed as there was in Case I. As in Case I we refer to Figure 3.7, which plots the seed in Figure 3.5 with a color scheme that assigns different colors to different  $k$  intervals. Again the procedure we used to obtain this color arrangement does not reproduce exactly the original waveform but does retain most of its shape. This time the top two panels do not show any navy blue and only a trace amount of light blue which suggest that  $k$ 's in the interval  $0.3 \leq k \leq 0.5$  are barely detected. The bottom four panels show sequential snapshots of initial seed growth to  $\pi$ -pulse formation and then to seed break-up, but this time a smaller wake (black) is made. Figure 3.8 shows the phase space features associated with the behavior of the plasma particles during the amplification

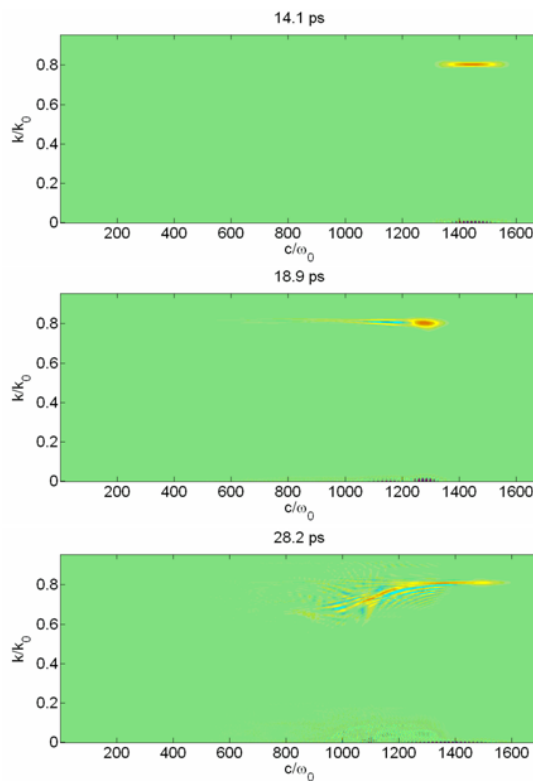


Figure 3.6: Wigner transform of the seed pulse undergoing amplification for Case II.

process. Calculation of quantities gives phase velocity  $v_\phi/c = 0.106$ , thermal velocity  $v_{the}/c = 0.01976$ ,  $v_\phi/v_{the} = 5.4$ , trapping width  $v_T/c = (2\omega_b/k_2)/c = 0.134$ . For this case the plasma frequency is  $\omega_{pe} = 3.31 \times 10^{14} \text{ s}^{-1}$ , the wave vector of the plasma wave is  $k_2 = 1.04 \times 10^7 \text{ m}^{-1}$ , the Raman growth rate of the pump is  $\gamma_R = 5.52 \times 10^{12} \text{ s}^{-1}$ , and the Landau damping rate is  $\nu_L = -4.45 \times 10^9 \text{ s}^{-1}$ . From the simulation the plasma wave grows to an amplitude of  $eE/m\omega_0c = 0.007$ , which gives an estimated bounce frequency of  $\omega_b = 2.1 \times 10^{14} \text{ s}^{-1}$ . We find that the ordering of quantities goes as  $\omega_{pe} \geq \omega_b \gg \gamma_R \gg \nu_L$ , which is the same as that of Case I. But in this case the phase space plot shows a larger amount of particles getting trapped inside the plasma wave (because the ratio of  $v_\phi$  to  $v_{the}$  is now smaller by almost 2.5 times), which is enough to show distinct vortices. The fact that  $k_2\lambda_D = 0.186$  indicates onset of kinetic effects such as trapping is expected. While the trapping vortices are regular and periodic in the leading

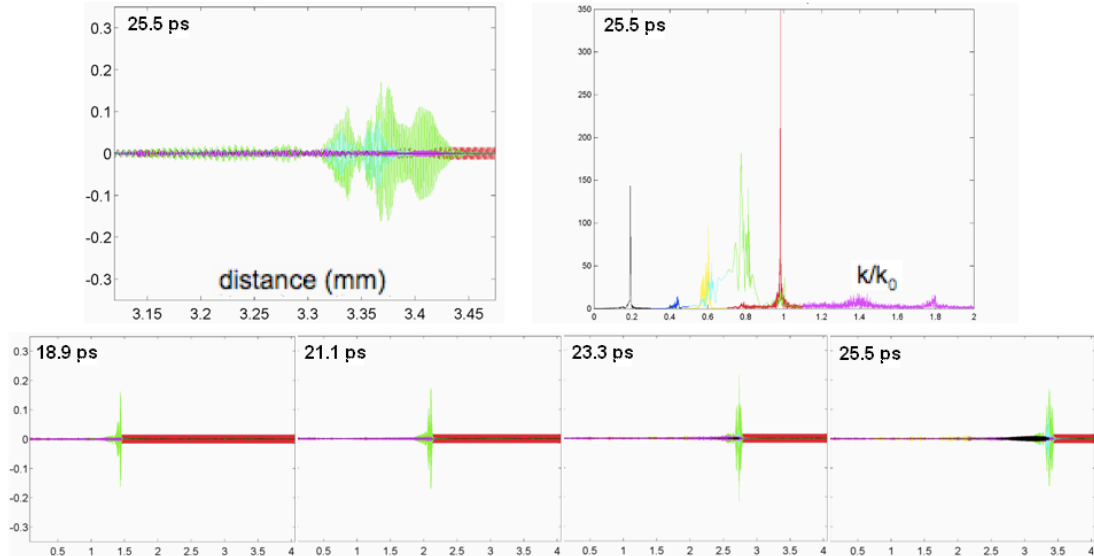


Figure 3.7: Case II - Color scheme representation of the seed waveform. The bottom row shows zoomed-out snapshots of the seed waveform in the entire box.

peak of the seed pulse, in the second peak there are signs of phase mixing as more particles are pulled out to the phase velocity of the plasma wave. The rear of the seed is completely phase mixed, the plasma is asymmetrically heated, and the wave starts to become incoherent. The amplitude of the plasma wave is seen to gradually decrease behind the seed, thus explaining why the seed has fewer and smaller secondary peaks. Another interesting feature, transient in Case I at earlier time but still persisting at 25.5 ps in Case II, is the development of a broad shoulder in the  $k$  spectrum. We believe this shoulder appears due to a nonlinear modification to the electron distribution function.

### 3.1.3 Case III

$$n_e = 0.015 n_{cr}, \omega_0/\omega_{pe} = 8.2$$

$$T_e = 500 \text{ eV}, k_2\lambda_D = 0.467, \text{ seed } \lambda = 1.258 \text{ } \mu\text{m}$$

The six panels on the left of Figure 3.9 show the amplification of the seed at various times during the simulation. The plasma is present in the simulation until 28.2 ps when the seed leaves into the vacuum region. As compared to the seed from the previous two cases the seed in this case causes the least amount of pump depletion and no  $\pi$ -pulse structure develops as there are no peaks behind the first. The amplification continues until the end of the simulation at 28.2 ps, with the seed traversing the entire 4 mm of plasma without experiencing RFS. RBS of the seed also does not occur and the frequency modulations of the seed are minimal. The  $k$  spectra at early and late times show that there are no visible peaks corresponding to the seed wake or to seed RFS. The peak corresponding to the plasma wave is barely visible. Figure 3.10 shows the Wigner transform. The seed initially has  $k = 0.8407 k_0$  at 14.1 ps. The seed does not show signs of break-up and remains relatively intact. There looks to be a slight redshifting at the front

of the seed but this shift is very minimal. Thus we do not show the color-coded plots for this case because the  $k$  spectra do not exhibit a wide range of features that need to be identified. Figure 3.11 shows the phase space features associated with the behavior of the plasma particles during the amplification process. To support the interpretation of these features we calculated the relevant quantities

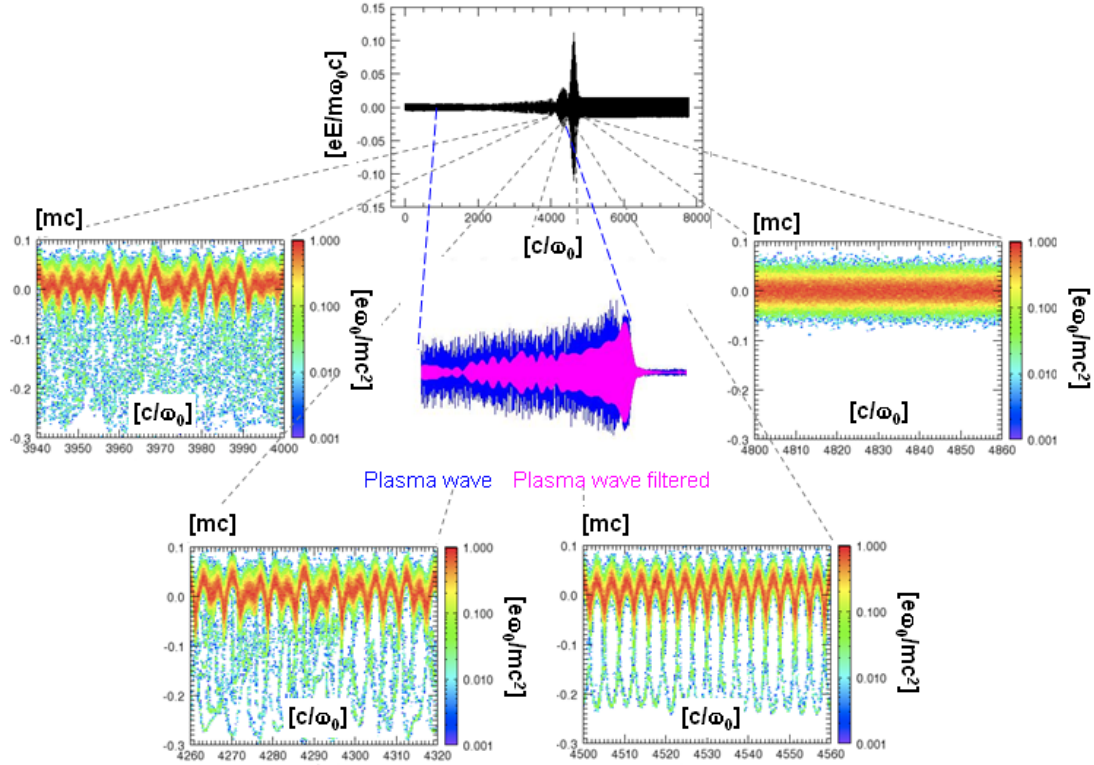


Figure 3.8: Case II - Phase space features at different locations inside the seed pulse. The center image shows the plasma wave with amplitude  $a_2 = eE_2/m\omega_0 c = 0.007$ . Non-resonant wave vector components have been filtered out and shown with the initial unfiltered plasma wave. Reprinted with permission from T.-L. Wang, D. S. Clark, D. J. Strozzi, S. C. Wilks, S. F. Martins, and R. K. Kirkwood, Phys. Plasmas **17**, 023109 (2010). Copyright 2010, American Institute of Physics.

for our parameter set, namely phase velocity  $v_\phi/c = 0.067$ , thermal velocity  $v_{the}/c = 0.03124$ ,  $v_\phi/v_{the} = 2.1$ , trapping width  $v_T/c = (2\omega_b/k_2)/c = 0.064$ . For this case the plasma frequency is  $\omega_{pe} = 2.17 \times 10^{14} \text{ s}^{-1}$ , the wave vector of the plasma wave is  $k_2 = 1.08 \times 10^7 \text{ m}^{-1}$ , the Raman growth rate of the pump is  $\gamma_R = 4.09 \times 10^{12} \text{ s}^{-1}$ , and the Landau damping rate is  $\nu_L = -4.97 \times 10^{13} \text{ s}^{-1}$ . From the simulation the plasma wave grows to an amplitude of  $eE/m\omega_0c = 0.0017$ , which gives an estimated bounce frequency of  $\omega_b = 1.03 \times 10^{14} \text{ s}^{-1}$ . From

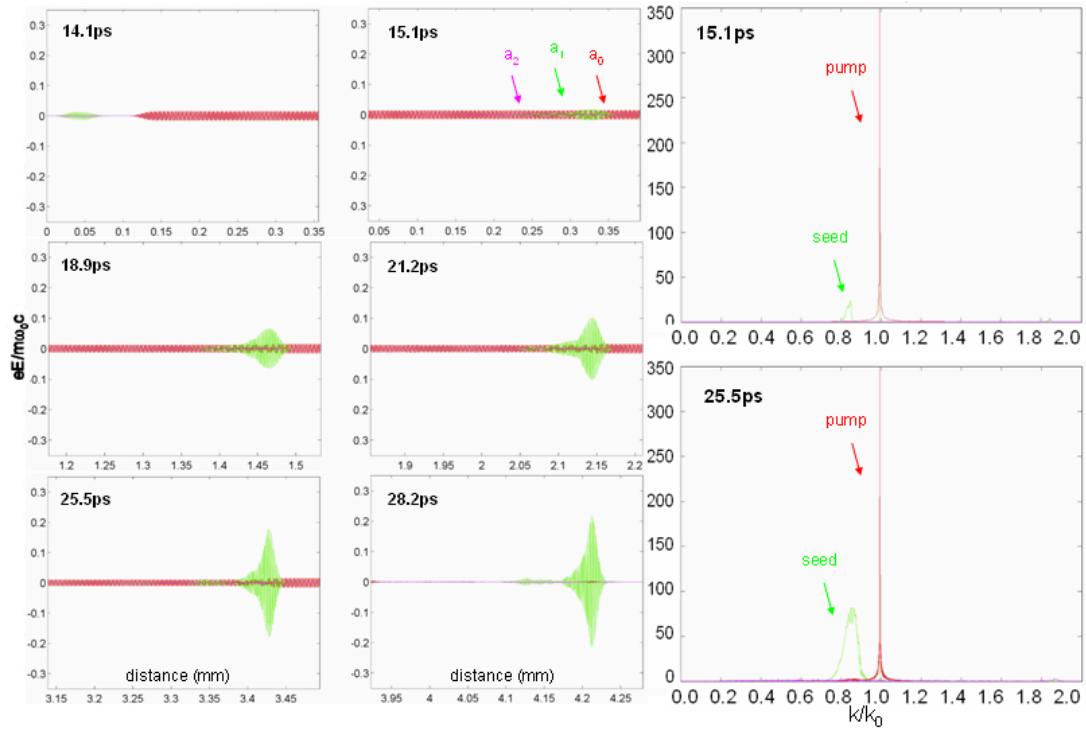


Figure 3.9: Case III - Snapshots of the seed at various times during amplification (left panels) and k spectrum of the pump, seed, and electrostatic waves (right panels). Reprinted with permission from T.-L. Wang, D. S. Clark, D. J. Strozzi, S. C. Wilks, S. F. Martins, and R. K. Kirkwood, Phys. Plasmas **17**, 023109 (2010). Copyright 2010, American Institute of Physics.

these calculations we find that the ordering of quantities goes as  $\omega_{pe} \geq \omega_b \geq \nu_L > \gamma_R$ . Since  $k_2\lambda_D = 0.467$ , the plasma exhibits a large degree of kinetic behavior and we see that most of the bulk particles are trapped causing the plasma wave to undergo wavebreaking. The major difference in this case from the previous two cases is that  $\nu_L$  is approximately  $10\times \gamma_R$ , which makes the entire Raman backscatter process strongly damped. The plasma wave is localized in the immediate region where the seed and pump overlap and has minimal amplitude elsewhere. In addition this case shows the least amount of pump depletion implying that the amplification does not reach the nonlinear regime over the simulated interaction region, thus explaining why the seed does not

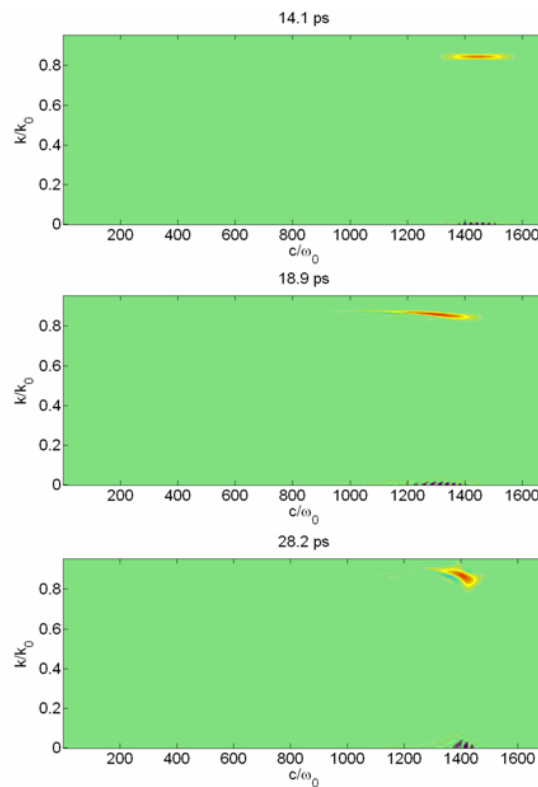


Figure 3.10: Wigner transform of the seed pulse undergoing amplification for Case III.

compress and form a  $\pi$ -pulse structure.

### 3.1.4 Case IV

$$n_e = 0.015 n_{cr}, \omega_0/\omega_{pe} = 8.2$$

$$T_e = 200 \text{ eV}, k_2\lambda_D = 0.298, \text{ seed } \lambda = 1.236 \text{ } \mu\text{m}$$

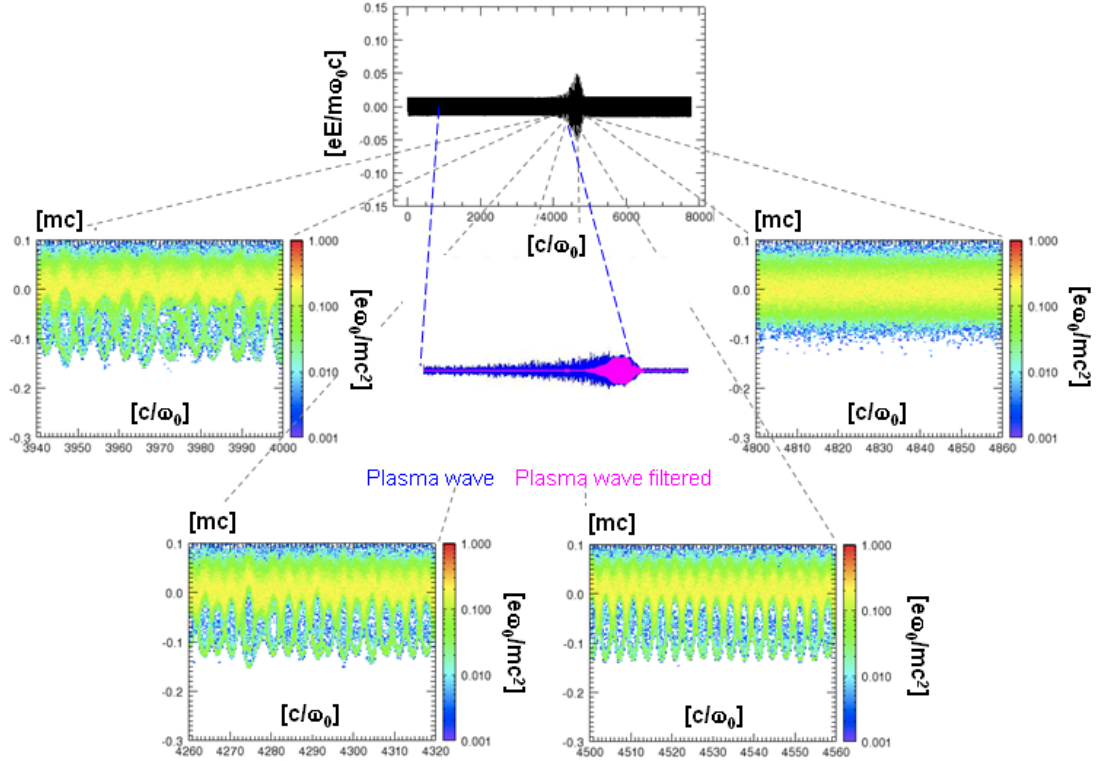


Figure 3.11: Case III - Phase space features at different locations inside the seed pulse. The center image shows the plasma wave with amplitude  $a_2 = eE_2/m\omega_0c = 0.0017$ . Non-resonant wave vector components have been filtered out and shown with the initial unfiltered plasma wave. Reprinted with permission from T.-L. Wang, D. S. Clark, D. J. Strozzi, S. C. Wilks, S. F. Martins, and R. K. Kirkwood, *Phys. Plasmas* **17**, 023109 (2010). Copyright 2010, American Institute of Physics.

The six panels on the left of Figure 3.12 show the amplification of the seed at various times during the simulation. The plasma is present in the simulation until 28.2 ps when the seed leaves into the vacuum region. The seed in this case causes a small amount of pump depletion and no definite  $\pi$ -pulse structure develops since there are only tiny peaks behind the first. The amplification continues until the end of the simulation at 28.2 ps, with indication of onset of RFS just after the seed traverses the 4 mm of plasma. Like in Case III, RBS of the seed does not occur and the frequency modulations of the seed are minimal. The  $k$  spectra at early and late times again shows that there are no visible peaks corresponding to the seed wake or to seed RFS. The peak corresponding to the plasma wave is again barely visible. Figure 3.13 shows the Wigner transform. The seed initially has  $k = 0.8608 k_0$  at 14.1 ps. Again the seed does not show signs of break-up and remains relatively intact. There is somewhat more of a steeper redshift at the front of the seed than in Case III and even a tiny amount of blueshift at the rear but again these shifts are small. Thus we do not show the color-coded plots for this case because the  $k$  spectra do not exhibit a wide range of features that need to be identified. Figure 3.14 shows the phase space features associated with the behavior of the plasma particles during the amplification process. To support the interpretation of these features we calculated the relevant quantities for our parameter set, namely phase velocity  $v_\phi/c = 0.066$ , thermal velocity  $v_{the}/c = 0.01976$ ,  $v_\phi/v_{the} = 3.4$ , trapping width  $v_T/c = (2\omega_b/k_2)/c = 0.084$ . For this case the plasma frequency is  $\omega_{pe} = 2.17 \times 10^{14} \text{ s}^{-1}$ , the wave vector of the plasma wave is  $k_2 = 1.09 \times 10^7 \text{ m}^{-1}$ , the Raman growth rate of the pump is  $\gamma_R = 4.36 \times 10^{12} \text{ s}^{-1}$ , and the Landau damping rate is  $\nu_L = -5.14 \times 10^{12} \text{ s}^{-1}$ . From the simulation the plasma wave grows to an amplitude of  $eE/m\omega_0c = 0.003$ , which gives an estimated bounce frequency of  $\omega_b = 1.37 \times 10^{14} \text{ s}^{-1}$ . From these calculations we find that the ordering of quantities goes as  $\omega_{pe} \geq \omega_b \gg \nu_L \sim \gamma_R$ .

Since  $k_2\lambda_D = 0.298$ , the plasma exhibits milder kinetic behavior than in Case III and we see that the trapping in this case just brings the plasma wave close to the threshold of wavebreaking. Again the plasma wave is still localized in the immediate region where the seed and pump overlap. This case shows somewhat more pump depletion than in Case III but it's still not obvious that it reaches the nonlinear regime. However the seed does have tiny trailing peaks that hint at a  $\pi$ -pulse structure. As will be elaborated upon in the next section, the seed

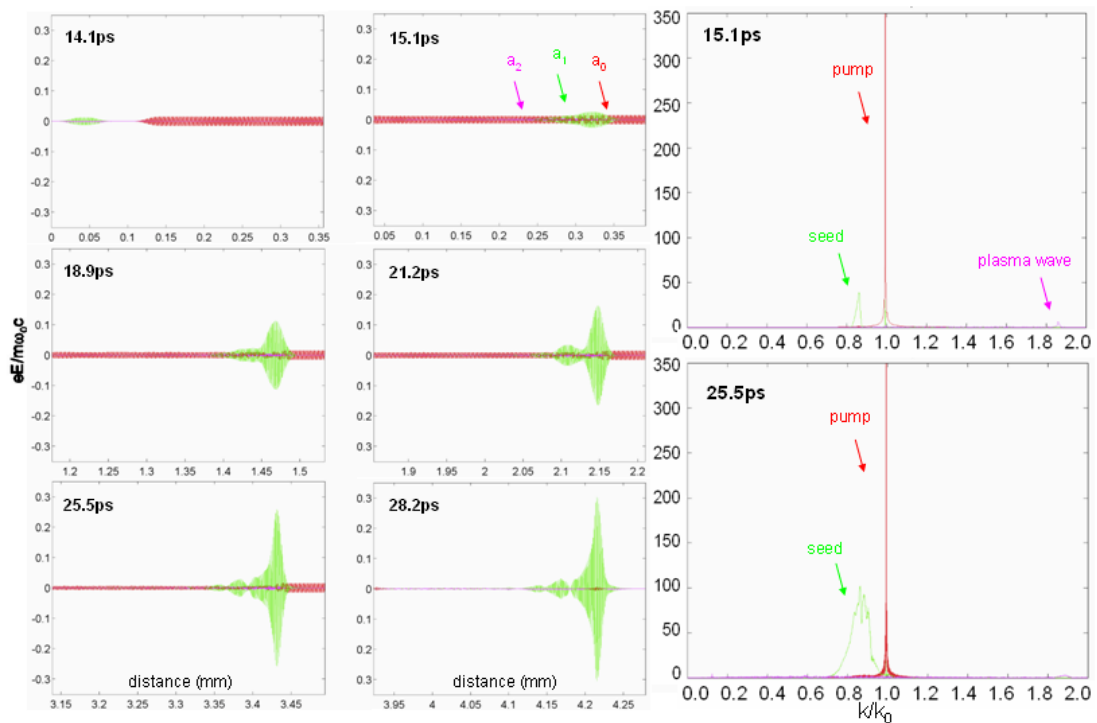


Figure 3.12: Case IV - Snapshots of the seed at various times during amplification (left panels) and k spectrum of the pump, seed, and electrostatic waves (right panels). Reprinted with permission from T.-L. Wang, D. S. Clark, D. J. Strozzi, S. C. Wilks, S. F. Martins, and R. K. Kirkwood, Phys. Plasmas **17**, 023109 (2010). Copyright 2010, American Institute of Physics.

in this case falls in the region of optimal amplification in our parameter scan.

### 3.2 Optimal plasma conditions for amplification

Cases I, II, III, and IV discussed above were selected from a set of 100 simulations that were performed to scan density and temperature parameters to find the optimal seed amplification conditions. The result of this scan is shown in Figure 3.15, which plots the measured amplitude of each seed just before the onset of seed RFS for each density and temperature case. We followed this metric to identify the end of amplification so that the amplitude is measured before the seed goes

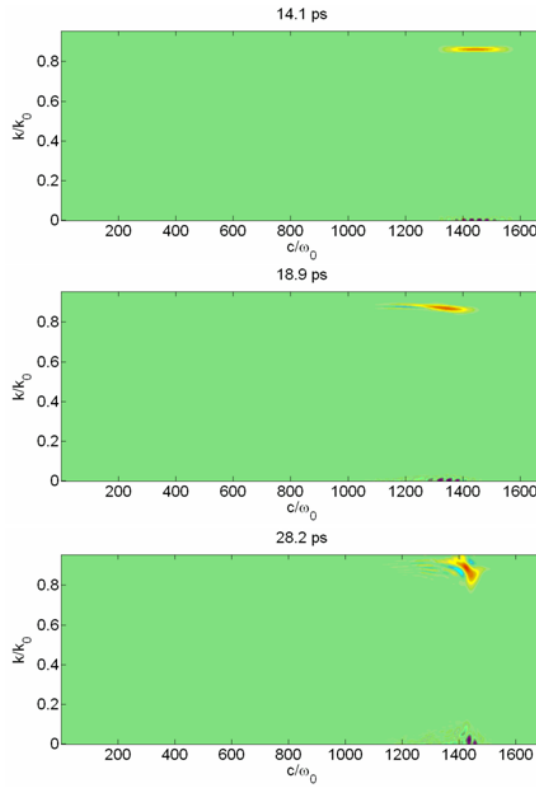


Figure 3.13: Wigner transform of the seed pulse undergoing amplification for Case IV.

unstable. A survey of this plot indicates that the optimal amplification condition occurs for plasma densities between  $0.01 n_{cr}$  and  $0.015 n_{cr}$  and temperatures up to 200 eV, which is towards the lower left corner of the plot, and Case IV lies this region. We find the results from this case to agree reasonably well with the predictions of 1D theory for  $\lambda = 1.064 \mu\text{m}$  and  $a_0 = 0.015$ , which gave  $n_e/n_{cr}$

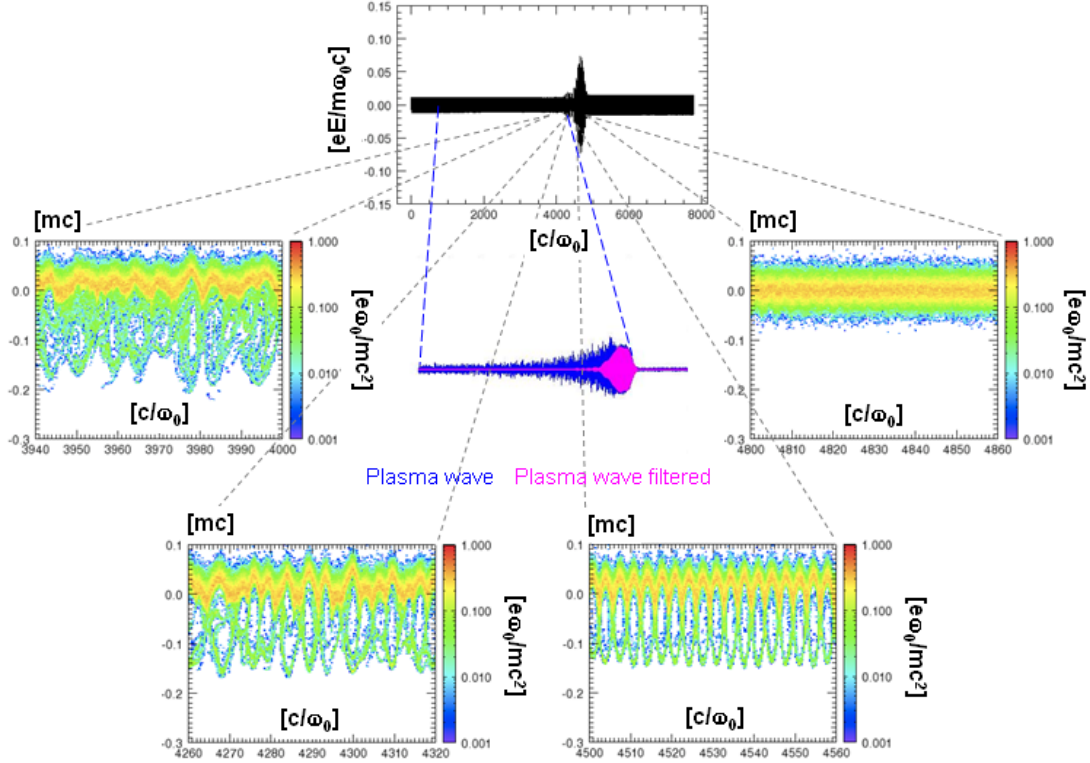


Figure 3.14: Case IV - Phase space features at different locations inside the seed pulse. The center image shows the plasma wave with amplitude  $a_2 = eE_2/m\omega_0 c = 0.003$ . Non-resonant wave vector components have been filtered out and shown with the initial unfiltered plasma wave. Reprinted with permission from T.-L. Wang, D. S. Clark, D. J. Strozzi, S. C. Wilks, S. F. Martins, and R. K. Kirkwood, Phys. Plasmas **17**, 023109 (2010). Copyright 2010, American Institute of Physics.

$\sim 0.015$  for the optimal density,  $a_1 \sim 0.4$  for the the final seed amplitude, and  $I \sim 2 \times 10^{17} \text{ W/cm}^2$  for the final seed intensity. The final seed amplitude for the optimal amplification cases all reach  $a_1 \sim 0.3$ . Although the gain in  $a_1$  is a modest  $20\times$  for the best case scenario, the corresponding intensity gain is  $400\times$  before the seed saturates due to instabilities. Assuming a  $500 \mu\text{m}$  spot diameter for the seed beam, a quick estimate using this value for intensity gain gives an output intensity of  $I \sim 8.1 \times 10^{16} \text{ W/cm}^2$ , while noting that the initial intensity was of order  $I \sim 10^{14} \text{ W/cm}^2$ . Because this is an unfocused intensity, in principle if large beams on the order of  $500 \mu\text{m}$  were to interact in a cm size preformed plasma with moderate temperature using large focusing mirrors in the geometry mentioned by Fisch [3], ultrahigh intensities could potentially be produced.

Another point to be mentioned is that the seed in Cases I, II, and III all amplify to approximately the same amplitude  $a_1 \sim 0.2$ . What this suggests is that there is flexibility in the choice of plasma conditions that can produce similar results, as the density/temperature in the three cases are all different. But taking a closer look we see that for Case I we are able to get amplification in the shortest period of time. We quantify this by calculating the RFS growth time ( $t_{RFS}$ ) of the seed in different plasma conditions to estimate the time right before it saturates due to instabilities [53]. We get  $t_{RFS} \sim 5 \text{ ps}$  for Case I,  $t_{RFS} \sim 6.6 \text{ ps}$  for Case II, and  $t_{RFS} \sim 12.4 \text{ ps}$  for Cases III and IV. Because Case I gives similar amplification to Cases II and III, but in the shortest time, this implies having to use less plasma interaction length to achieve the same result. The extra benefit is that the seed pulse also compresses and develops the  $\pi$ -pulse shape since it depletes the pump.

Also shown in Figure 3.15 is the labeling of the transition into wavebreaking of the plasma wave. As mentioned earlier optimal amplification requires the use of a low enough plasma density to delay the onset of seed RFS, but yet high enough

to avoid wavebreaking of the driven plasma wave. This serves to illustrate the fact that there is competition among processes such as seed growth instability and wavebreaking as we scan along different pairs of density and temperature points. We also know that the transition into wavebreaking of a uniform plasma wave in a cold plasma is well-defined, but in a thermal plasma the transition is less obvious and entering the wavebreaking regime is more gradual over den-

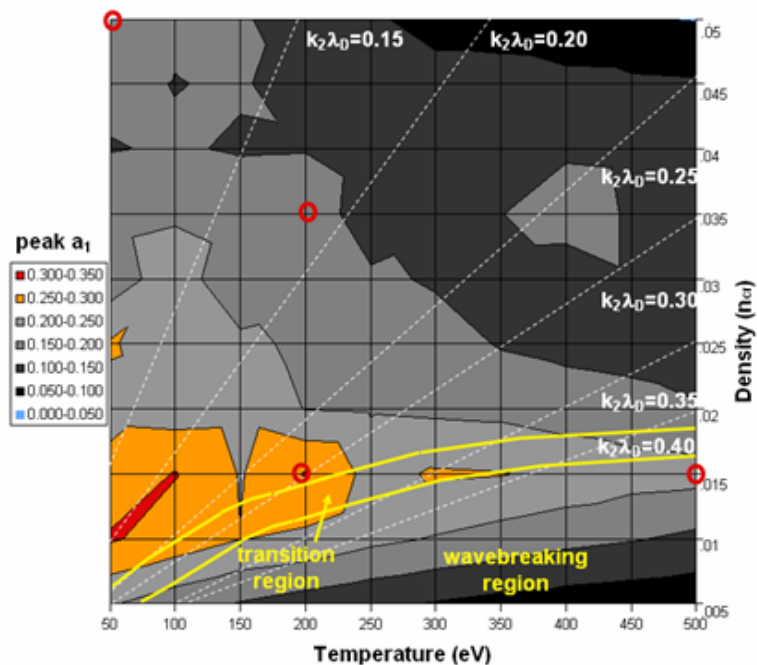


Figure 3.15: Density vs temperature plot showing parameter regime for optimal seed amplification. The four cases presented earlier are indicated by the circles. Optimal amplification of the seed is shown to be possible for plasma densities between  $0.01 n_{cr}$  and  $0.015 n_{cr}$  and temperatures up to 200 eV. Reprinted with permission from T.-L. Wang, D. S. Clark, D. J. Strozzi, S. C. Wilks, S. F. Martins, and R. K. Kirkwood, Phys. Plasmas **17**, 023109 (2010). Copyright 2010, American Institute of Physics.

sity and temperature. So to quantify this as much as possible, we inspected the phase space plots for the simulation cases and made a heuristic determination of wavebreaking by estimating which cases showed trapping of the largest number of electrons. From this we identified the wavebreaking region in Figure 3.15 and showed that transition into wavebreaking occurs in a gradual manner. Furthermore we find that our optimal amplification region falls near the border of the wavebreaking region, which agrees with the concept of driving the plasma wave up to the wavebreaking limit for best amplification. In addition, this serves to show that the minimum allowable density we can use for amplification without wavebreaking is a function of temperature.

In this study we found that the best amplification cases are the ones where no  $\pi$ -pulse forms and pulse compression is not obvious. While it is true that high densities and low temperatures allow the seed to quickly enter the nonlinear pump depletion regime and form a  $\pi$ -pulse, they do not yield the best amplification primarily due to the earlier onset of seed RFS. Also, realistic experimental factors such as heating and thermal expansion of the plasma will render several regions of our density and temperature plot inaccessible. This is because one typical method of creating preformed plasmas for BRA experiments is to collisionally ionize a supersonic gas jet using a nanosecond-scale heater beam [20], with the resulting plasma acquiring finite temperatures on the order of 100's of eV. As we will mention in later chapters, the gas jet ionizes within the first few 100 ps of the heater beam while the rest of the beam contributes to the heating and subsequent radial hydrodynamic expansion of the plasma due to the higher electron pressure on axis. Fortunately the region of plasma densities between  $0.01 n_{cr}$  and  $0.015 n_{cr}$  and temperatures around 200 eV, which we identified as having the best amplification, is realizable in experiments. Therefore with the pump wavelength we have chosen, we would need a seed wavelength in the range

of 1200 nm to 1300 nm to access the resonance. We must reiterate that this study was done entirely in 1D, with the purpose of comparison to 1D theory from the three wave model for BRA. In order to establish better guidelines for experiments, simulation studies in 2D need to be performed using large finite spot sizes so that effects such as refraction, transverse filamentation, and beam spray of the pump and seed beams can be better understood.

Finally we should note that we identified RFS as the primary mechanism which causes the seed to break apart as it creates a wake behind it. On the other hand it is well-known from research on laser wakefield accelerators that ultrashort laser pulses having a pulsewidth less than half of a plasma wavelength will not undergo RFS while making a wake to accelerate electrons. Since the densities we simulated in this chapter range from  $5 \times 10^{18} \text{ cm}^{-3}$  to  $5 \times 10^{19} \text{ cm}^{-3}$ , a 100 fs seed pulse is respectively 4 times and 12.5 times larger than half the plasma wavelength associated with those densities. Thus it will be interesting to simulate BRA with a shorter pulsewidth, say 25 fs if the plasma density is  $5 \times 10^{18} \text{ cm}^{-3}$ , to determine the amount of amplification. However one should consider the level of coupling associated with using lower density plasmas and also the validity of the three wave model when considering that scenario.

## CHAPTER 4

### Creating Seed Laser Pulses

#### 4.1 Description of the experiment

From the previous chapters we know that in order for energy transfer from the pump laser to the seed laser to occur via resonant Raman scattering in a plasma, it is necessary to have a seed frequency that is down-shifted from the pump frequency by the plasma frequency. In our seed amplification experiment which we will discuss in Chapter 5, we use a pump laser wavelength of 1054 nm. Therefore the seed laser wavelength must be down-shifted further into the infrared in order to be in resonance with the plasma frequency, which is dictated by the plasma density and temperature conditions. In this chapter we will review our seed creation experiment to generate down-shifted wavelengths using the phenomenon called nonlinear optical frequency down-conversion. The specific mechanism that we use for this frequency down-conversion is molecular Raman scattering in a gaseous medium. To achieve this we employ a specially designed Raman gas cell that was assembled at LLNL.

A Raman cell or a Raman convertor is a device that is designed to perform optical frequency conversion of an incident wavelength via the mechanism of molecular Raman scattering. Because spontaneous scattering is weak and stimulated Raman scattering is an intensity-dependent process, a laser is the ideal optical source to use. The Raman cell is filled with a high pressure gas and

the intense laser beam has an adequately high power density to excite the gas molecules, thus activating the nonlinear optical effect. The cell basically acts as a quantum amplifier, taking one photon starting from the noise at the down-shifted frequency and giving it gain. This happens because intense light momentarily interacts with gas molecules to generate new virtual excited energy levels which are different from the usual electronic energy levels of atoms. These new virtual states are in the vibrational-rotational manifold so called because diatomic and polyatomic gas molecules have extra vibrational and rotational degrees of freedom that are not present in ordinary atoms. For diatomic molecules each electronic energy level  $E_e$  now contains a set of nearly equally spaced vibrational energy levels  $E_v$  and each vibrational energy level contains a subset of unequally spaced rotational energy levels  $E_J$  governed by the rules  $eE_v = \hbar\omega_{vib}(v+\frac{1}{2})$  and  $eE_J = \frac{\hbar^2}{2}I_{mol}J(J+1)$  respectively. The notation is such that  $v$  is the vibrational quantum number,  $J$  is the rotational quantum number,  $\omega_{vib}$  is the vibrational frequency, and  $I_{mol}$  is the rotational moment of inertia. These rules follow from using the harmonic oscillator model for vibration and dumbbell model for rotation in a diatomic molecule. Vibrational and rotational levels can all potentially appear in a polyatomic gas and some can be preferentially excited over others depending on the polarization of the incident laser light. Potential energy curves showing the electronic, vibrational, and rotational levels of a molecule are schematically depicted in Figure 4.1. The output from a Raman cell comes in the form of photon energy released when the molecule transitions from the higher (virtual) excited energy levels down to the lower levels. The output consists of the incident laser frequency at  $\omega_0$  and shifted frequencies at  $\omega_0 \pm n\omega_R$  corresponding to Stokes and anti-Stokes lines, where  $\omega_R$  is the frequency of the Raman-active vibration of the scattering gas molecule and  $n$  are integer values representing higher order harmonics of the frequency shift. The light that remains at  $\omega_0$  is the byproduct

of elastic or Rayleigh scattering while the desired shifted wavelengths are due to inelastic or Raman scattering from the gas molecules as the process of excitation and subsequent transitions between the vibrational and rotational energy states occurs. An example of a transition is given by the green arrows in Figure 4.1. We should also keep in mind a few of the features in this figure. First,  $R$  is the spacing between the atomic nuclei of the molecule. Second, the ground state has a finite width  $\Delta R$  due to the natural nonzero vibrational energy  $\frac{1}{2}\hbar\omega_{vib}$  that the molecule possesses. Third, the vibrational energy levels are the long horizontal lines within the troughs of the curves representing the electronic energy levels. Fourth, the rotational energy levels are shown in the inset as short horizontal

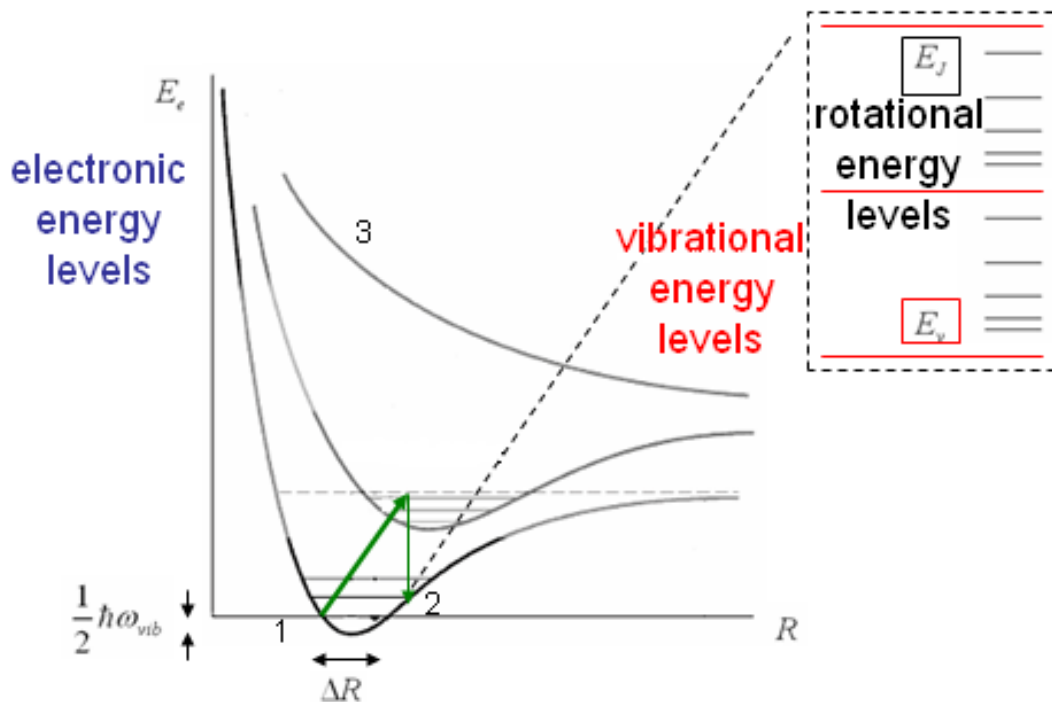


Figure 4.1: Potential energy curves showing the electronic, vibrational, and rotational levels of a molecule.

lines occupying the area between the longer vibrational lines in red. Finally, the dashed horizontal line just above the bottom-most potential energy curve indicates the dissociation energy of the molecule. The incident photon energy must not be greater than this energy or else the molecule will dissociate rather than produce Raman scattered light.

To go into more detail about the properties of the output light, we refer to simplified energy level diagrams given in Figure 4.2. The energy levels labeled 1, 2, and 3 in these diagrams correspond to the energy levels labeled in Figure 4.1. A sufficiently strong pump will excite gas molecules from the ground state level 1 to a virtual state A, and stimulated emission of Stokes radiation occurs when there is sufficient population in A relative to that in a lower level 2. On the other hand if there is already a significant population on level 2 with respect to level 1 the pump photon can instead give rise to anti-Stokes scattering in which the excitation starts from level 2 to an even higher virtual state B before relaxing back down to level 1. For Stokes scattering the result is a lower photon energy

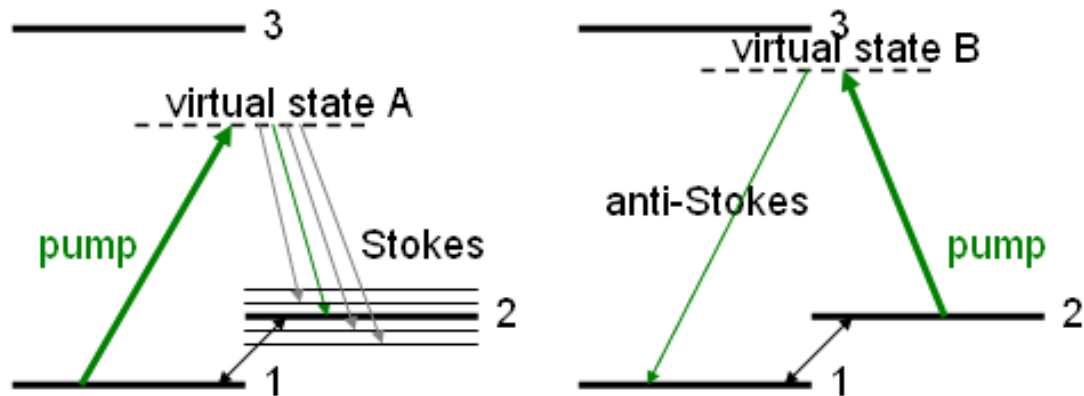


Figure 4.2: Simple energy level diagram showing Stokes and anti-Stokes transitions.

out since energy is given to the gas molecule and for anti-Stokes scattering the result is a higher photon energy out since energy is taken from the gas molecule. However, the light produced by anti-Stokes scattering is typically much less intense than that produced by Stokes scattering and that is why Raman cells are mostly used to generate Stokes wavelengths inside the lab. The left hand diagram in Figure 4.2 has multiple arrows showing other transitions that lead to Stokes radiation. Having a group of arrows depicts the possibility of relaxation to an assortment of lower energy vibrational and rotational states. The intensity of individual output lines typically depends on the density of the gas, which can be adjusted by changing the gas pressure inside the cell. Theoretically the first Stokes line has the maximum conversion efficiency of 50% and the intensity decreases with increasing order of the lines since higher-order Raman conversion is a sequential process [54]. It's also logical to think that higher gas pressures lead to better conversion efficiencies. But in practice, conditions inside the cell such as local heat buildup from laser energy deposited during the Raman process and the dynamics of the internal gas circulation can have an impact on the results.

In our seed creation experiment we use a 2 meter long Raman gas cell. A sketch of the cell is shown in Figure 4.3 along with an inset that shows the positioning of its internal optics. Since high gas pressures are used inside the cell, the windows at each end of the cell are made of very thick  $MgF_2$  in order to contain the gas. Because of this requirement the input laser beam needs to have a large diameter so that its intensity is low enough to fall below the threshold of undesirable nonlinear optical effects such as B-integral that can cause transverse breakup of the beam or self phase modulation that can cause unwanted frequency modulation. In this way the thick windows will cause minimal distortion to the beam as it goes into the cell. Once inside the cell the beam can be down-collimated to higher intensities for efficient Raman conversion to oc-

cur. In our case the laser beam diameter is initially 4 inches and the internal cell optics comprise a 4:1 down-collimating telescope that focuses the beam to 1 inch in diameter for the interaction. Thus although the total length of the cell is 2 meters, the interaction length is only 1 meter because of space requirements of the telescoping optics installed at both ends. Generating Stokes light in the forward direction is an automatically phase matched process and having a collimated beam over 1 meter helps to confine the converted light within the area of the initial spot better than if the light were converging and diverging. At the rear end of the cell a 1:4 up-collimating telescope brings the beam diameter back to 4 inches to exit through the thick window. Gases for the Raman cell are chosen based on their characteristic frequency shift and Raman scattering cross section. The Raman cross section of a gas is an indicator of its conversion efficiency since the Raman gain depends on the product of the cross section, gas pressure, pump intensity, and the interaction length. Table 4.1 shows the gases that we evaluated for generating the seed wavelength. The table shows each gas

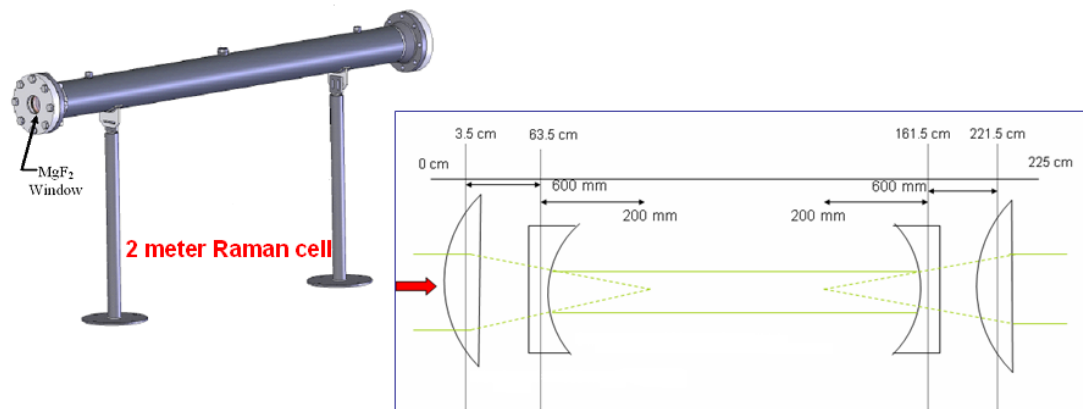


Figure 4.3: Schematic of the 2 meter long Raman gas cell. The inset shows the arrangement of the internal telescope optics.

Table 4.1: Candidate Raman gases for seed pulse generation.

Gas	Raman shift	Cross-section	Order	Output wavelength
$H_2$	$587 \text{ cm}^{-1}$	$2.2\sigma_{N_2}$	2	1201 nm
$N_2O$	$1287 \text{ cm}^{-1}$	$2.2\sigma_{N_2}$	1	1218 nm
$C_3H_8$	$867 \text{ cm}^{-1}$	$2.4\sigma_{N_2}$	1	1514 nm

along with some basic properties found from previous work that characterized Raman gases [55, 56]. The Raman shift of each gas is quoted in units of inverse centimeter or wavenumber. The output wavelength is calculated from the input wavelength, the Raman shift, and the order of the shift. The cross-section of a gas is given relative to the cross-section of the Nitrogen gas molecule, which is a common practice in scientific journals. We chose these gases primarily because they were readily accessible in the lab, but also because the literature reported their Raman frequency shifts (i.e. the Raman frequency  $\simeq$  the plasma frequency) to be adequate for downshifting 1054 nm light to the wavelength that we wanted. The next section discusses our experiment and the procedure we used to study these candidate gases.

## 4.2 Experimental layout and procedure

Our seed creation experiment was done using the Compact Multi-pulse Terawatt (COMET) hybrid CPA laser system [57] at LLNL. The COMET laser is in a room adjacent to Target Area 1 where we did the main seed amplification experiment. COMET consists of a Ti:Sapphire oscillator and a regenerative amplifier tuned to 1054 nm, followed by a four-stage Nd:Phosphate glass amplifier. The initial 400 fs pulse from the oscillator is stretched to 1 ns in a folded single-grating stretcher. After a single pulse is switched out of the regenerative amplifier, it is amplified in

16 mm and 25 mm diameter rod amplifiers and then split to form several beams which are further amplified in 50 mm diameter final amplifiers. The COMET laser system provides a total of four beam lines, of which two (Beam 1 and Beam 4) are used our experiments. Both beams initially have a wavelength of 1054 nm. Beam 4 is sent to an open air compressor and then frequency doubled to become a probe beam for plasma interferometry later in the amplification experiment. Beam 1 is sent to the Raman cell for generating the seed. Beam 4 is slightly less than 1 inch in diameter, has a pulsewidth of 0.5 ps, and its energy can reach up to 20 mJ. Beam 1 is approximately 4 inches in diameter coming out of the COMET vacuum compressor, has a nominal pulsewidth of 0.5 ps when fully compressed, and outputs a maximum energy of 6 J. Pulsewidths in Beam 1 of up to 5 ps can be generated by changing the stretcher grating angle before the vacuum compressor so that the non-optimal recompression by the compressor gratings yields a longer pulse.

Figure 4.4 shows a diagram of the experimental setup. Everyday at the beginning of the experiment the facility technicians aligned the COMET laser and then gave us a 10 Hz, 1054 nm alignment beam. We used this alignment beam along with IR cards, IR viewers, crosshairs, and cameras to make sure the beam went through the Raman cell. If the beam had strayed slightly from the center axis of the cell, it would not make it out the other end. Therefore this alignment was critical and we had to methodically go through many iterations of adjustments to the large dielectric high reflectivity 1054 nm mirror to make sure that a collimated beam went into and came out from the Raman cell. At the exit of the cell, we placed another large dielectric mirror but with high transmissivity around the neighborhood of 1200 nm to pass only the down-shifted wavelengths and dump the unconverted 1054 nm light. Since the output beam was back to its initial diameter of around 4 inches at the exit, we had to set up another

down-collimating 4:1 telescope to decrease the beam size back down to 1 inch diameter to make it a more manageable spot for transport by a series of silver steering mirrors. The mirrors were positioned to send the beam over to a diagnostics table where a fiber spectrometer, calorimeter, and autocorrelator were set up. Figure 4.5 shows photographs of the setup. More details regarding this set of equipment will be given in Chapter 5 since these diagnostics were used in the seed amplification experiment. The large red arrow at the top of the figure shows where the seed beam was redirected for that experiment. But for this experiment the diagnostics table was located several feet away from the Raman cell. On the diagnostics table we had a couple of other optics in addition to the equipment shown in Figure 4.4. We mounted a CVI Melles-Griot LPF-1100 long pass filter to block light below 1100 nm. This served as an additional assurance that any residual 1054 nm was filtered since there was a lot of unconverted light

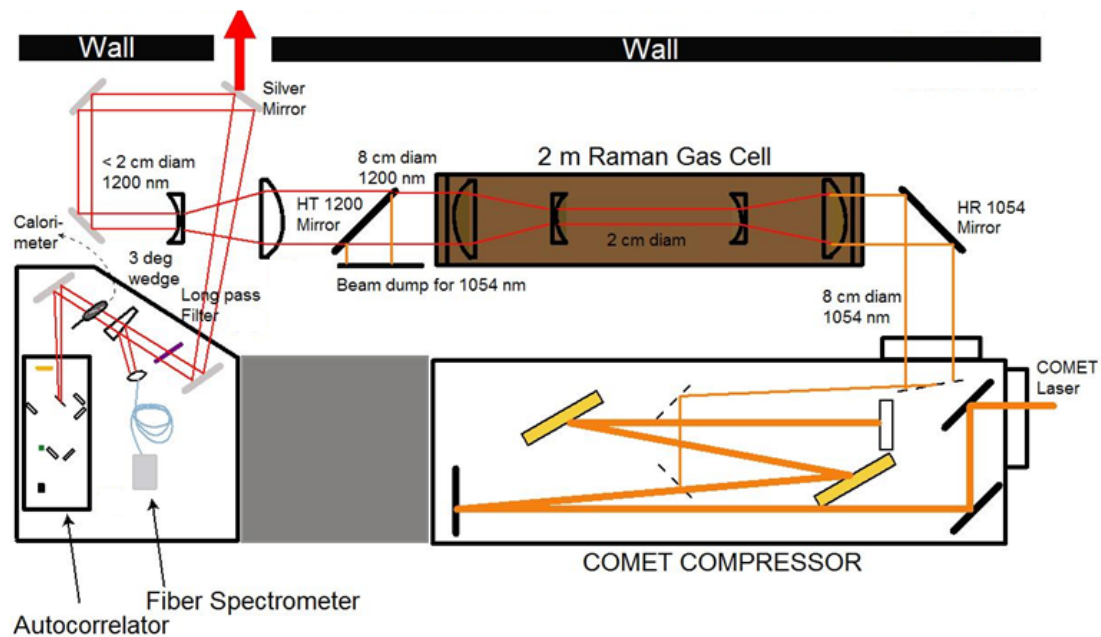


Figure 4.4: Schematic of the Raman cell.

due to poor conversion efficiency of the cell, which will be discussed in the next section. The LPF-1100 also blocked any anti-Stokes light since we only wanted to detect the down-shifted wavelengths. After the filtering optic a 3 degree “pick-off” wedge was used to reflect a small percentage of the light into a lens coupled to the fiber spectrometer. The remainder of the seed light was sent to either the calorimeter or the autocorrelator. We were unable to run both diagnostics simultaneously since we wanted the calorimeter head to measure the entire seed energy and autocorrelation measurements required as much energy as possible because of sensitivity issues. Nonetheless the main goal of this experiment was to evaluate the spectral properties of the seed laser pulse made from different gases so the spectrometer was the most important diagnostic.

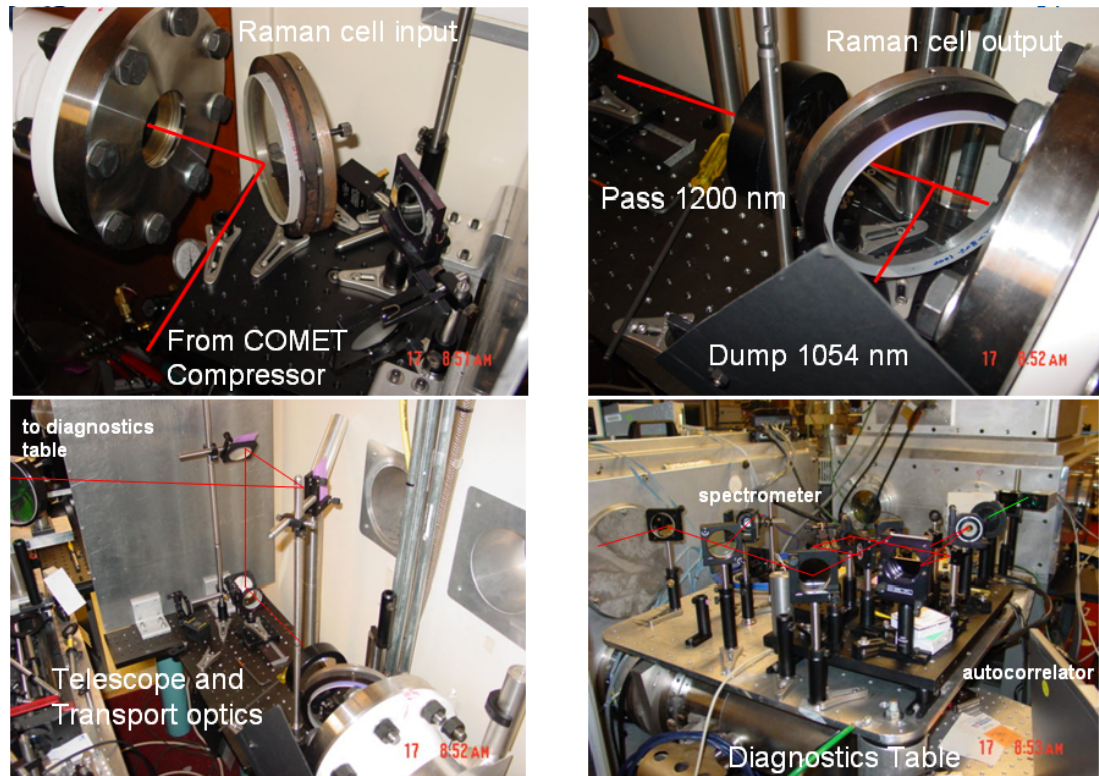


Figure 4.5: Pictures of the experimental setup.

The procedure of the experiment was to fill the Raman cell with one gas, shoot the COMET laser into the cell, adjust the pressure and laser energy from shot to shot, and acquire spectral information about the output light as well as its energy and pulsewidth. Since this was more of an exploratory study, we did not make adjustments in any particular order but rather changed parameters based on the results of the previous shot. The general idea was to identify a favorable spectrum that could potentially be used for the seed wavelength and then fire multiple shots to check for repeatability of the data. Since the COMET laser fired one shot every 4 minutes, we were able to take numerous shots. Thus we were able to acquire many spectra and also get a reasonable number of calorimeter readings and autocorrelation traces. After we finished our study with one gas we used pure Nitrogen to flush the cell before switching to the next gas. When adjusting the pressure of the gas we had to be aware of the maximum pressure rating of the Raman cell, which was 200 psi, as a safety precaution. Finally, we made sure to use a laser energy fluence that was below the damage threshold fluence of the cell's internal telescope optics. From doing fluence calculations that took into account the laser spot size, we determined that for the shortest pulsewidth of 0.5 ps we could safely use an energy of up to 300 mJ ( $60 \text{ mJ}/\text{cm}^2$ ), and for longer pulsewidths up to 5 ps we could safely use energies of up to 3000 mJ ( $592 \text{ mJ}/\text{cm}^2$ ).

### 4.3 Experimental results

The first gas we used was  $H_2$  and we found from the literature that the 2nd order rotational line would give a Stokes line at 1201 nm. Because we were looking for a rotational line, we needed circularly polarized light. So we mounted a quarter wave plate in front of the entrance window of the Raman cell and tuned the angle

of its optical axis to make it 45 degrees with respect to vertical. We then did a pressure scan with pressures of 75 psi, 125 psi, and 175 psi. From the many spectra that we obtained with  $H_2$  gas, we consistently observed rotational lines at 1124 nm (1st order), 1201 nm (2nd order), and 1293 nm (3rd order). We found that by increasing the gas pressure we could get the 2nd, 3rd, and even a small amount of 4th order to appear in the spectrum. We also saw a large 1st order vibrational line at 1870 nm, which we believe appeared because the polarized light was not purely circular and had residual linear components that could excite vibrational lines. Finally we saw a line at 2100 nm which we interpreted as being half of the frequency of the original 1054 nm light. Although we were unable to identify the nature of this line, the fact that it appeared indicated that a small portion of energy was being down-shifted by a significant amount.

The second gas we studied was  $C_3H_8$ , commonly known as propane. The immediate limitation we had with this gas was that it liquifies at slightly above 100 psi. Thus our pressure scan had to stay well below this value and we chose to use 25 psi, 60 psi, and 86 psi. We removed the quarter wave plate for this study and used linearly polarized light. We saw a large peak corresponding to the 1st order vibrational line at 1514 nm as well as a sizeable line at 1054 nm. We found that by increasing the gas pressure we could make the 1054 nm line smaller and transfer some of the energy into what appeared to be a bump in the spectrum at around 1100 nm, while the 1514 nm line remained relatively unchanged. No other spectral features were observed and for  $C_3H_8$  the generation of the Raman line at 1514 nm was robust and reproducible.

The last gas we studied was nitrous oxide ( $N_2O$ ), commonly called laughing gas. We used linearly polarized light because  $N_2O$  has a 1st order vibrational line at 1218 nm. Like in the case of  $H_2$  we did a pressure scan, but this time went all the way to 200 psi. What we found as we took laser shots was that the spectrum

was centered at 1218 nm but was much broader in width than the downshifted lines we obtained from the other gases. This happened at several different gas pressures. Since having a broad spectrum seed could be useful for a plasma with density inhomogeneities or a ramp density profile, we decided to fix the incident laser energy and gas pressure and took multiple shots to reproduce this result. After we convinced ourselves that the broad spectrum could be reproduced, we went back and reviewed the spectral data obtained from all three gases to make a decision as to which gas to use for the amplification experiment. Figure 4.6 summarizes the results of the Raman lines for the candidate gas that we studied.

The gas we ultimately chose to use was  $N_2O$ . With  $H_2$  we had multiple lines to choose from, but because each was quite sharp it was very likely that the one we intended to use could miss the resonance if it were off by say 20 nm which corresponds to a density difference of  $\delta n_e = 3.5 \times 10^{18} \text{ cm}^{-3}$ . Also the seed energy was spread over many narrow lines including the large line at 1870 nm, thus making the energy in the lines of interest quite small. Furthermore we found that circular polarized light was harder to work with because of the precision needed for angle tuning the quarter wave plate.  $C_3H_8$  would have been a convenient gas to use since all the energy was contained in a relatively narrow region around 1514 nm. However, as we'll mention in Chapter 5, the gas jet pressure that we used to make the plasma could not provide a density that was large enough ( $n_e \sim 10^{20} \text{ cm}^{-3}$ ) to push the resonance out to 1514 nm. Plus we had determined earlier that wavelengths down-shifted so far away from 1054 nm would be non-optimally amplified. Thus it was not feasible to use  $C_3H_8$ . Therefore we decided to use  $N_2O$ , being fully aware that we would have to work with a broad rather than a narrow line. Because of its broad spectrum we basically sacrificed getting the greatest amount of spectral energy at one particular wavelength in exchange for the guarantee that one of the wavelengths in the spectrum will match the

resonance. Figure 4.7 shows how the broad spectrum widens and grows as a function of incident COMET laser energy. We filled the Raman cell with  $N_2O$  at 150 psi, or roughly 10 atm, to avoid having to work at the maximum pressure rating of the cell. Although  $N_2O$  already has a low dissociation energy ( $D[N_2-O] = 1.57$  eV) the individual photon energy of 1054 nm light is 1.18 eV, which is still low enough to not cause dissociation of the molecules.

Having chosen  $N_2O$ , it behooved us to understand why it produced a broad spectral output. Typically Raman gas cells operate in the steady state regime where the laser pulses are on the order of several nanoseconds [58]. However

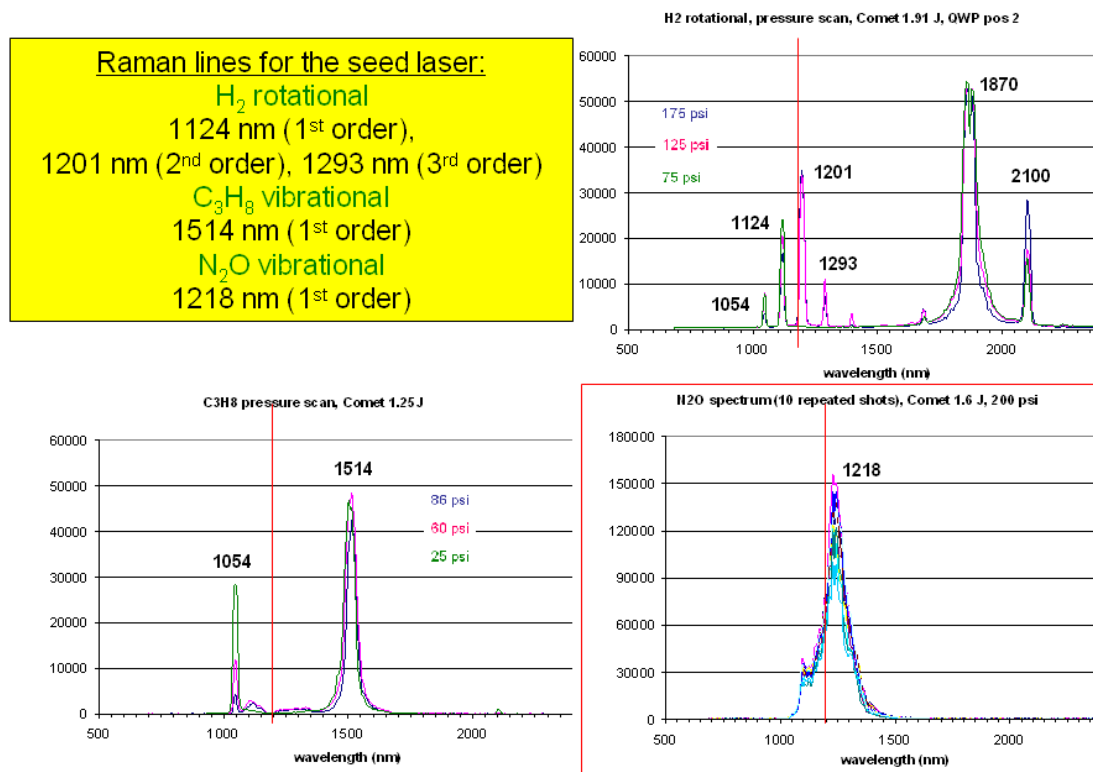


Figure 4.6: Results of Raman lines produced with  $H_2$ ,  $N_2O$ , and  $C_3H_8$  gases. The red vertical line is a reference marker for 1200 nm, showing where it falls in the seed spectrum. All vertical axes are in raw counts.

the COMET pulsewidth in our experiment was short enough to put the conversion mechanism in what's called the transient regime, explored originally using picosecond pulses [59, 60]. The transient regime occurs when the relation  $\tau_p < G_{SS}\tau_2$  is satisfied, where  $\tau_p$  is the laser pulsewidth,  $G_{SS}$  is the dimensionless steady state Raman gain of the gas, and  $\tau_2$  is the molecular dephasing time of the gas. So we made some calculations to determine if our seed pulsewidth in  $N_2O$  gas puts us in the transient regime:

$$2 \times \text{atomic weight N} = 2 \times 14.01 \text{ amu}$$

$$1 \times \text{atomic weight O} = 1 \times 16.00 \text{ amu}$$

$$N_2O \text{ molar mass M} = 2 \times 14.01 \text{ amu} + 1 \times 16.00 \text{ amu} = 44.02 \text{ amu}$$

Given the molar mass M and specifying a 10 atm gas pressure, we can obtain the number density (N), the cross section ( $\sigma$ ), the thermal velocity ( $\langle v \rangle$ ), and the dephasing time ( $\tau_2$ ) of  $N_2O$  using the formulas on p. 195 of [61] and the ideal gas law.

$$N = 3 \times 10^{16} \text{ cm}^{-3} / \text{Torr} \times 760 \text{ Torr} \times 10 \text{ atm} = 2.3 \times 10^{20} \text{ cm}^{-3}$$

$$\sigma \approx 3.9 \times 10^{-16} \text{ cm}^2 \text{ (from estimation using the characteristic atomic cross section)}$$

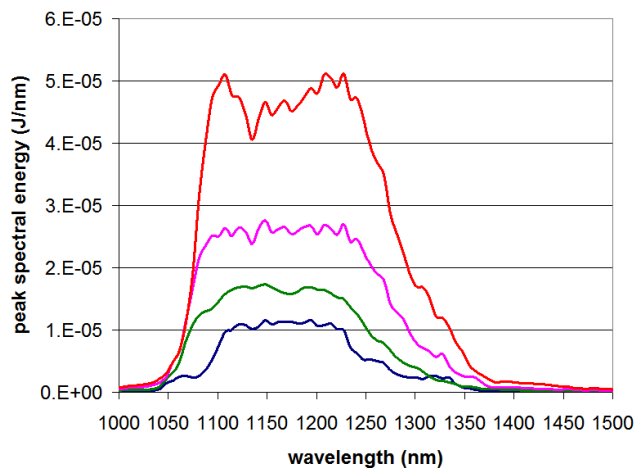


Figure 4.7: COMET laser energy scan for  $N_2O$  gas at 150 psi.

for Hydrogen  $\pi a_0^2 = 0.88 \times 10^{-16} \text{ cm}^2$  where  $a_0$  is the Bohr radius)

$$\langle v \rangle \approx [(8kT/\pi)(2/M)]^{-1} = 2.85 \times 10^5 \text{ cm/s}$$

$$\tau_2 = [N\sigma\langle v \rangle]^{-1} = [(2.3 \times 10^{20})(3.9 \times 10^{-16})(2.85 \times 10^5)]^{-1} = 39 \text{ ps.}$$

Therefore since  $\tau_2$  is 39 ps,  $G_{SS}$  is never less than unity, and our seed pulsewidths were on the order of a few picoseconds, we verified that Raman conversion in our case indeed occurs in the transient regime. The other aspect of Carman's research points out that a consequence of being in the transient regime is that Raman conversion results in the excitation of broad rather than narrow lines and that the reason could be due to short pulses having a broader bandwidth than what the Raman medium (the gas) can sustain. We believe that the results we observed with  $N_2O$  gas were consistent with this interpretation. In addition, we think that another reason for the broad line could be due to excited states relaxing and coupling to an assortment of lower vibrational and rotational energy states as was shown in Figure 4.2. Keeping these explanations in mind, it is important to note that all the frequencies in the broad line are not in phase. Thus they cannot be mode-locked to produce ultrashort pulses. The output pulsewidth of the cell remains fairly close to the input pulsewidth which we verified with autocorrelator measurements.

We mentioned earlier that the shortest pulsewidth coming from the COMET laser was 0.5 ps and that longer pulses of up to 5 ps could be produced as well. But all of this was subject to measurement by the autocorrelator. When we evaluated the three gases we did so using primarily the long pulse due to fear of damaging the optics in the Raman cell. From the autocorrelator we measured the pulsewidth to be 3.7 ps coming out of the cell. One typical trace is shown in Figure 4.8. This was followed by Raman generation using the short pulse where we measured the pulsewidth to be 0.67 ps, which was slightly longer than the stated nominal value of 0.5 ps from COMET. Figure 4.9 plots sample spectra

made by the 0.67 ps and 3.7 ps pulses. The spectra are normalized for the sake of comparison. Fluctuation in the peak position of each spectrum from shot to shot is expected since both spectra are broad. Also the spectrum made by the 0.67 ps pulse is seemingly wider than that of the 3.7 ps pulse at the half maximum location. This is most likely another indication of the transient nature of the

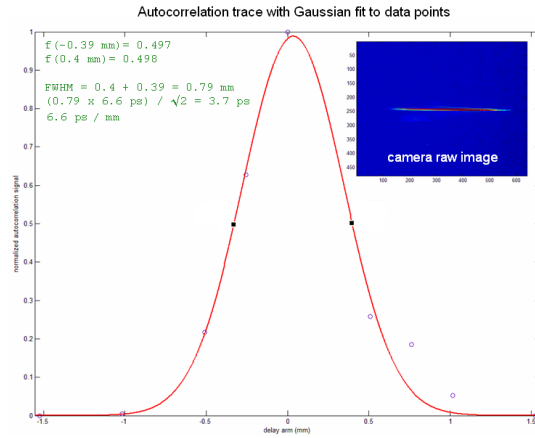


Figure 4.8: Typical autocorrelation trace giving a pulsewidth measurement of 3.7 ps for the laser pulse converted by  $N_2O$  gas.

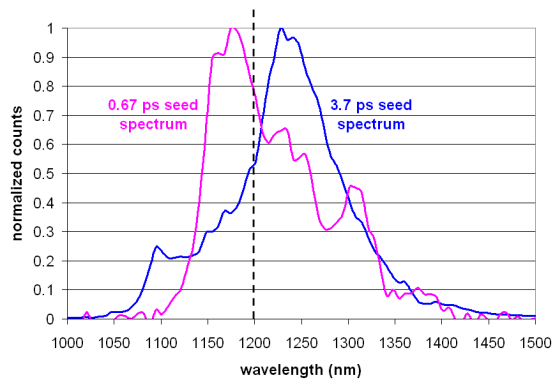


Figure 4.9: Comparison of normalized spectra for 0.67 ps and 3.7 ps pulses for  $N_2O$  gas.

conversion.

The last issue that we want to briefly touch upon is the conversion efficiency of the Raman cell. We knew to begin with that the Raman conversion in our cell could have a low efficiency resulting in a large amount of unconverted 1054 nm light, which was subsequently dumped. So our goal was then to get as much output energy as possible rather than to aim for high conversion efficiency. To give an idea of the efficiency we had, a 3.7 ps pulse from COMET with energy of 1.2 J gave an output energy of 3.2 mJ. This corresponded to a conversion of 0.26%. Similarly a 0.67 ps pulse from COMET with energy of 300 mJ gave an output energy of 0.6 mJ, which corresponded to a conversion of 0.2%. These were indeed very low conversion efficiencies even though we put in up to a few Joules of light. In the future higher Raman conversion efficiency could be obtained by a two-stage amplification approach where a first, short Raman cell operating at perhaps higher pressure/pump intensities could produce a seed that is then “amplified” in the longer cell such as that we have described.

# CHAPTER 5

## Amplifying Seed Laser Pulses

### 5.1 Introduction

In this chapter we report the results of our seed amplification experiment that we performed at LLNL in the Target Area 1 of the Jupiter Laser Facility. We amplified the downshifted COMET Beam 1 that was described in our seed generation experiment in the previous chapter. In the amplification experiment we brought in the Janus laser as the pump laser to interact with and transfer energy to the seed. The Janus laser system is a large Nd:Glass laser system [63] in the Jupiter Laser Facility that serves as the main workhorse laser for several different labs in the facility. The Janus laser beam that comes into Target Area 1 has a wavelength of 1054 nm and contains energies of up to 232 J in a 1 ns pulse. The focused spot size has a 500  $\mu\text{m}$  diameter and a Rayleigh length  $z_R = \pi w_0^2/\lambda = \pi(250 \mu\text{m})^2/(1.054 \mu\text{m}) = 186 \text{ mm}$ . These properties of the Janus laser allowed us to use the same pulse for several purposes: 1) to ionize the gas to create the plasma, 2) to heat that plasma to moderately hot temperatures, and 3) to serve as the pump laser to interact with the seed laser inside the plasma.

The plasma in our experiment was created by laser-induced collisional ionization of a supersonic stream of gas flowing out of the tip of a 3 mm diameter gas jet nozzle. The design concept behind our nozzle, which was fabricated at the machine shop at LLNL, is very similar to nozzle designs developed and charac-

terized by Malka that maximize gas flow uniformity [64]. The mechanical valve that regulated the speed of the gas flow from the gas cylinder to the base of the nozzle is a Parker Hannifin Series 9 pulse valve (Model 009-0181-900) with a maximum pressure rating of 1450 psi. The gas that we used in this experiment is Helium and adjusting the backing pressure of the gas allowed us to change the eventual plasma density. Plasma densities on the order of  $1 \times 10^{19} \text{ cm}^{-3}$  were used in our experiment. Since the pump laser had a pulsewidth of 1 ns, the typical ionization process using these types of long laser pulses is collisional. In collisional ionization the laser field accelerates electrons which collide with and scatter from neutral atoms and ions both elastically and inelastically. This in turn produces more ions and also allows the exchange of energy with other electrons, thus producing a plasma with a distribution of electron energies that can be quantified as a temperature.

Computer simulations show that during the course of ionization by the large energy 1 ns pump pulse, the plasma gets heated to moderately hot temperatures which indicates that electron thermalization occurs well within the laser pulsewidth. HYDRA, a fluid hydrodynamics code commonly used at LLNL [65], was used to model the plasma density and temperature in our experiments. HYDRA assumes local thermodynamic equilibrium (LTE) and includes radiation transport and radiation losses. The laser beam is deposited and evolved using ray tracing routines and the computational space is arranged in an Euler-Lagrangian mesh where the cells can deform as a response to the laser pressure. The code takes neutral Helium gas at a fixed pressure and uses a LTE Thomas-Fermi model for ionization by an incident laser with a large spot 500  $\mu\text{m}$  diameter phase plate. The Thomas-Fermi model is a statistical model that approximates the many-electron structure of an atom by a free-electron gas surrounding the nuclei with interactions based on Coulomb forces [66]. The results indicated that

the gas ionizes within the first 200 ps of the pump pulse and the remainder of the pulse contributes to further heating and radial hydrodynamic expansion of the plasma [20]. For 1450 psi gas, the code predicted a density of around  $1 \times 10^{19} \text{ cm}^{-3}$  and a temperature of somewhere between 250 eV and 300 eV. Since HYDRA has been successfully benchmarked against many past experimental results [67, 68], this gave us confidence in its predictions for our experiment. As a further corroboration of our plasma conditions we took the results from an experiment by Gregori on nonlocal transport that was performed in Target Area 1 with the same Janus laser system in 2003 [69]. Their plasma conditions were similar to ours and they made actual measurements of the plasma temperature using the Thomson scattering diagnostic. Although their plasma conditions were not exactly identical to ours (they had a slightly higher pump laser intensity, longer pulsewidth, and shorter plasma), their measurements of density and temperature were within the range of our values by approximately 30%. Thus we assume that our computed temperature of between 250 eV to 300 eV was reasonably accurate. That temperature value taken along with our own plasma interferometry measurements, allowed us to determine the  $k_2 \lambda_D$  for our plasma conditions. Of course we need to emphasize that realistically we did not expect the plasma profile to be very uniform in either the radial or axial directions. Non-uniformities in the flow of the gas coming out of the nozzle, a common occurrence in laser plasma experiments involving gas jets, and the heat flow and subsequent expansion of the hot plasma due to higher electron pressures on axis, will cause the plasma profile to evolve over the course of 1 ns. Furthermore, for higher densities we can expect higher temperatures since more of the heater laser gets absorbed and there will be larger radial blast waves that can cause additional heating and more channel digging inside the plasma [70, 71]. However in our case, because the seed only takes 20 ps to traverse the plasma, during that time interval we can think

of the plasma profile as being roughly static.

Although a dynamically evolving and non-uniform plasma is not the ideal plasma for seed amplification this is the byproduct that we end up with when using a large energy long pulse pump laser for ionization and amplification. As mentioned previously in Chapter 3, seed amplification requires the plasma length to only be half of the spatial length of the pump beam to ensure complete interaction between the pump and the seed when the timing is such that the seed enters one edge of the plasma just as the leading tip of the pump begins to exit that edge. Thus the 1 ns pump in our case will theoretically call for a 15 cm plasma which, to our knowledge, has not been created and maintained in a laboratory to have densities as high as  $1 \times 10^{19} \text{ cm}^{-3}$ . Because many research groups around the world have successfully fabricated gas jet nozzles of several mm in diameter for use in laser plasma experiments at these densities, we know that at least the 3 mm nozzle that we used is based on a realistic and mature design that could produce a plasma that we needed. However amplification in a 3 mm plasma will ideally require access to a 20 ps pump laser pulse. The experiments at Princeton modified their laser system to produce a 20 ps pulse by purposely imposing a non-optimal grating pair separation in their compressor so that the output would be 20 ps instead of transform-limited. In our case the beam from the Janus laser arm that was available to us was fixed at 1 ns and therefore we could only change our experimental setup to incorporate this type of laser pulse. But one benefit that this pulse gave us was that its Rayleigh length is much longer than the plasma size, which guaranteed us a very long depth-of-focus. So the physical picture of our experiment that we designed is that the pump first enters the gas jet and begins creating the plasma through collisional ionization. After about 200 ps, when the plasma is fully ionized and heated, the seed is sent into the plasma and interacts with a local 20 ps portion of the pump over the

3 mm interaction distance. Once the amplified seed exits the plasma and clears itself from the latter part of the pump, it leaves the target chamber to be measured while the remnants of the pump finish their path through the jet and get discarded onto a beam dump. The plasma state is maintained throughout the course of the interaction since the 1 ns laser, corresponding to a spatial dimension of 30 cm, continuously ionizes the 3 mm region of gas as new portions of the pulse constantly enter the jet. Therefore it is apparent that the plasma only exists when the pump laser is present.

Table 5.1 shows a list of parameters that describe the plasma conditions in our experiment, calculated using linear plasma theory and the equations from Kruer [1]. While it is possible that a fully kinetic calculation of certain parameters will yield slightly different values, it will not change the order of magnitude comparison among them. First off, from the calculations, we estimate that  $k_2\lambda_D$  is between 0.4 and 0.5 which tells us that kinetic effects play a dominant role in this plasma. Next, we can characterize the plasma as weakly coupled ( $\gamma_R \ll \omega_{pe}$ ), underdense ( $\omega_{pe} \ll \omega_0$ ), and moderately hot ( $kT_e \ll mc^2$ ). In addition we expect any plasma wave to be strongly damped since  $\gamma_R < \nu_L$ . Calculating the electron-ion collision frequency  $\nu_{ei}$ , which also tells us the electron-electron collision frequency  $\nu_{ee}$  and the electromagnetic wave damping rate  $\nu$ , we find that the plasma is collisionless since  $\nu_{ei} \ll \omega_{pe}$  and collisional damping of electromagnetic waves is negligible. To address the issue of collisional absorption we use the NRL plasma formulary [72] to calculate the inverse bremsstrahlung absorption coefficient  $\kappa$ . We find that  $\kappa = 0.0143$  which corresponds to a characteristic absorption length of  $1/\kappa = 69.716$  cm. Since our plasma scale length of 3 mm is much less than this absorption length, proportionality tells us that both pump and seed lasers will traverse the plasma and retain more than 99% of their energy. This simple estimate was made with a plasma density that's uniform at around

Table 5.1: Plasma parameters for the seed amplification experiment.

Parameter	Value
$k_2\lambda_D$	0.4-0.5
$\omega_{pe}$	$1.60 \times 10^{14}$
$\gamma_R$	$2.19 \times 10^{12}$
$t = 1/\gamma_R$	0.46 ps
$\nu_L$	$2.35 \times 10^{13}$
$\nu_{ei}$	$6.39 \times 10^{10}$
$\nu = \nu_{ei}\omega_{pe}^2/\omega^2$	$5.12 \times 10^8$
$\nu_{ee} \sim \nu_{ei}/\sqrt{(2)}$	$4.52 \times 10^{10}$
$1/\kappa$	69.716 cm
$\omega_b$	$2.27 \times 10^{13}$
$\tau_b = 2\pi/\omega_b$	0.28 ps
$v_{the}/c$	0.0235
$v_\phi/c$	0.0476
$v_T/c$	0.014

$1 \times 10^{19} \text{ cm}^{-3}$  and a nominal temperature of 280 eV. But we know that when the plasma is first created it starts out cold and takes a finite amount of time to heat to 280 eV, and since colder plasmas have smaller scale lengths for inverse bremsstrahlung, the pump laser could be affected by this absorption. However, as outlined in the next section, the seed is timed to enter the plasma when the resonant density and temperature have been reached. And since it only interacts with 20 ps of the pump once the plasma is fully heated, it is not expected to be affected by absorption in the plasma. The remainder of the table contains estimates of quantities that are less straightforward to interpret and call for guidance from experimental data. These quantities relate to the kinetic behavior of

the plasma, namely wavebreaking and particle trapping. Initial calculations with guidance from 1D PIC simulations of our plasma allow us to obtain values for the phase velocity of the plasma wave  $v_\phi$ , the bounce frequency  $\omega_b$  of possible trapped particles, and their trapping width  $v_T$ . A quick survey of values in this table indicates that the plasma wave amplitude will be below the wavebreaking threshold since  $\omega_{pe} > \omega_b$ . As for evidence of trapping, comparisons that yield  $v_\phi/v_{the} = 2$ ,  $\omega_b \sim \nu_L$ , and  $|v_\phi/c - v_T/c| = 1.4v_{the}/c$  indicate that some degree of trapping will occur. The last section of this chapter will present the data from the amplification experiment we performed in 2009 with short 0.67 ps seed pulses. Some pertinent results from the amplification experiment in 2008 with long 3.7 ps seed pulses [62] will also be shown and compared with the short pulse data. The data sets together with the trends they exhibit may help explain the behavior of short and long seed pulse amplification.

## 5.2 Experimental layout and procedure

Most of the seed amplification experiment setup was in Target Area 1. The gas jet was mounted at the center of the interaction chamber in Target Area 1. The 1054 nm Janus pump and the downshifted Beam 1 COMET seed lasers enter through separate ports to illuminate the target. Figure 5.1 shows a schematic of the entire experiment. The pump beam is transported to the target via a pneumatic, vacuum-tight mechanical arm that attaches directly onto the interaction chamber. The arm contains transport optics, a mounted phase plate, and a final focusing lens, that deliver the beam onto the target. The pump is electronically timed and its temporal offset with respect to the seed was adjusted from the main control room (thus the “delay” of the seed in entering the pump really comes from the adjustment of the pump timing). The electronic timing system provided a

coarse scan with a 100 ps resolution and had a jitter of  $\pm 100$  ps. The seed, as discussed in Chapter 4, comes into Target Area 1 from the COMET laser lab next door and is steered by mirrors into the chamber. The 527 nm Beam 4 COMET laser shoots transverse to the pump and seed interaction direction, serving as the probe for interferometry. The various diagnostic equipment for this experiment,

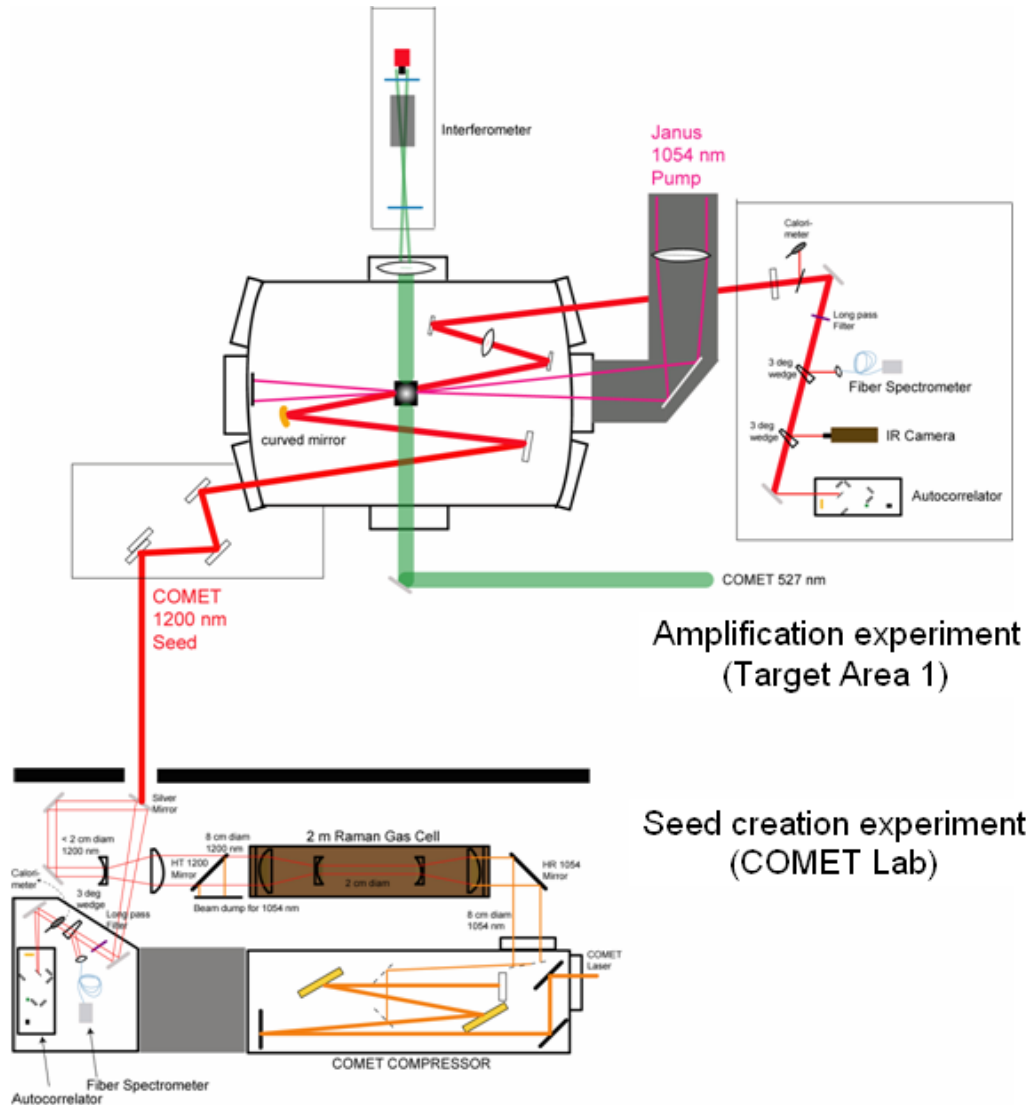


Figure 5.1: Overall schematic of the seed amplification experiment.

such as the autocorrelator, calorimeter, spectrometer, and infrared camera, were set up on the optical tables surrounding the outside of the chamber as shown in Figure 5.1.

For our description of the experimental procedure we refer to Figure 5.2 which shows just Target Area 1 and Figure 5.3 which shows actual photos of the setup. Everyday at the start of the experiment, the facility technicians aligned both the Janus and COMET laser systems before giving us the 10 Hz, 1054 nm alignment beams from each system. We then proceeded to align the COMET beam through our entire system beginning with the Raman cell and ending on the diagnostics table outside of the chamber. We used IR cards, IR viewers, crosshairs, and

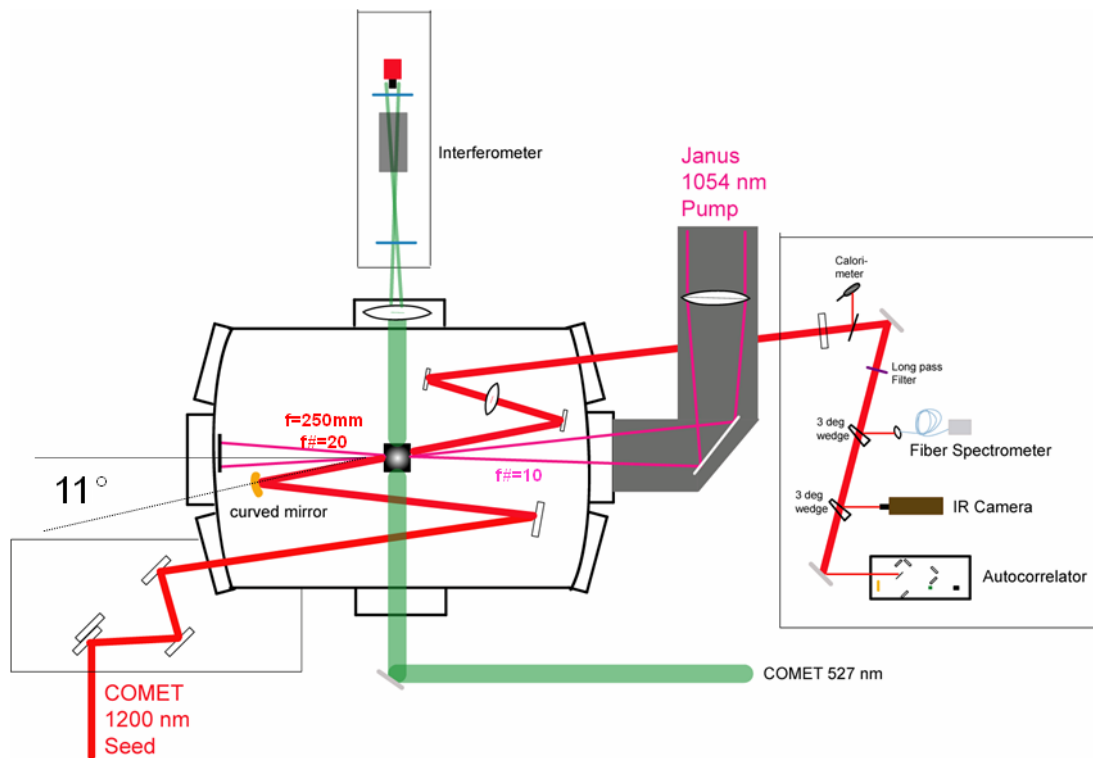


Figure 5.2: View of the various laser beam paths in Target Area 1.

cameras for this important step. The steering mirrors (shown as slanted rectangles in Figure 5.2) used for alignment and beam transport are custom-made triple-stacked dielectric mirrors from CVI Melles-Griot, specifically coated for high reflectivity at the 1054 nm and 1200 nm to 1300 nm wavelengths, and were arranged to preserve the linear polarization direction of the seed beam to stay in parallel with the pump polarization. The Raman cell is shown in the top left of Figure 5.3 along with the beam transport tubes that direct the beam from the COMET lab into Target Area 1. The top right of Figure 5.3 shows the respective ports from which the seed beam (in red), the interferometry beam (in green), and the pump beam (in orange) enter the chamber. The bottom left of Figure 5.3

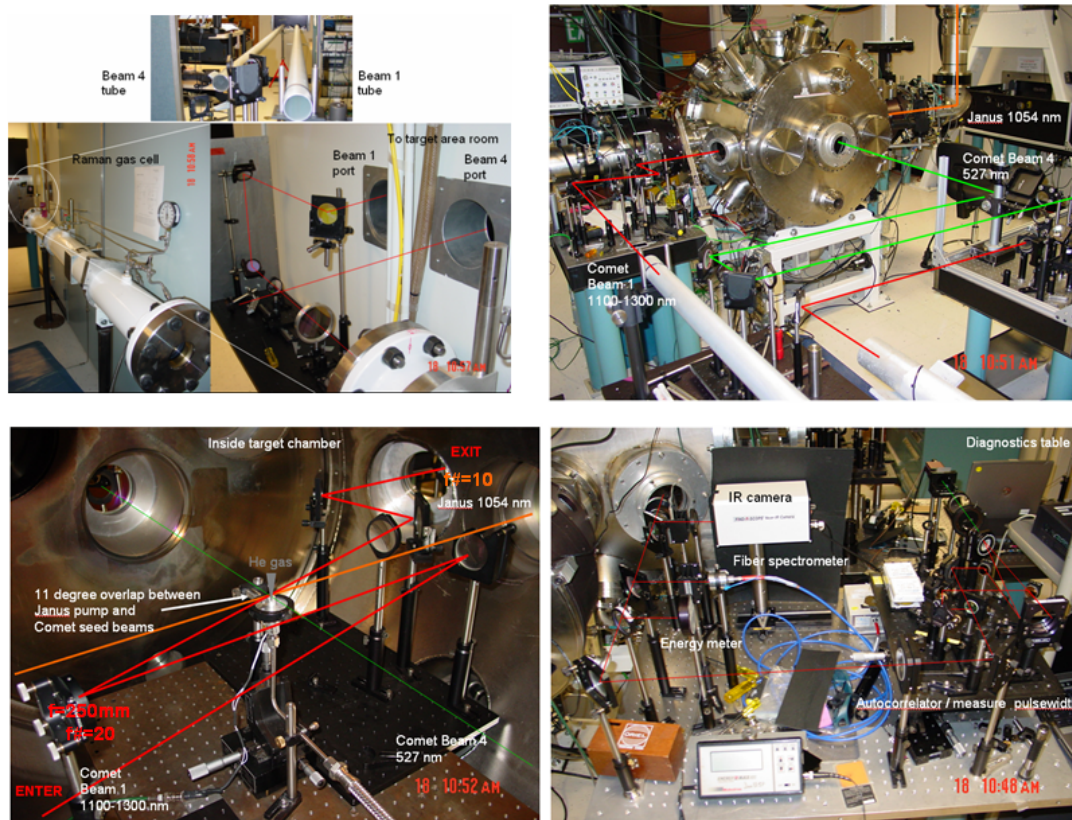


Figure 5.3: Pictures of the experimental setup.

shows the inside of the target chamber. The gas jet is situated in the center and the seed beam follows a zig-zag path as it comes to a focus in a  $f/20$  geometry to the chamber center, where it meets the Janus pump beam that comes to a focus in a  $f/10$  geometry. The spot diameter at focus for both lasers is  $500\ \mu\text{m}$ . To ensure spatial overlap of the pump and seed beams we placed a  $500\ \mu\text{m}$  ceramic pinhole on top of the gas jet nozzle during the alignment and used a camera to check that the beams from both Janus and COMET intersected at the pinhole. We also measured the temporal overlap between the beams using an Electro-Optics Technology ET-3500 InGaAs PIN photodiode placed at the chamber center. After the seed passes the gas jet it zig-zags out of the chamber onto a diagnostics table shown on the bottom right of Figure 5.3. A small percentage of the seed energy was split off into a FJW Optical Systems Model 85700 infrared camera and an Ocean Optics NIR256-2.5 fiber spectrometer for spot profile and spectral measurements respectively. The remainder of the energy was sent to either one of two diagnostics: 1) a J50LP-1 detector head attached to a Moletron EnergyMax EM400 calorimeter for seed energy measurements or 2) a home-built autocorrelator with frequency doubling KD\*P crystal tuned to the phase matching angle for 1200 nm light for seed pulsewidth measurements. The reason for not being able to use both energy and pulsewidth diagnostics simultaneously is that the sensitivity of both diagnostics require that they receive the maximum amount of energy possible, and thus we had to delegate the measurements from shot to shot. Interferometry data is obtained by a Mach-Zehnder interferometer installed on an optical table outside of the target chamber along the path of Beam 4. Both autocorrelator and interferometer setups used an Allied Vision Technologies AVT Stingray F-033B externally-triggered firewire camera to capture the images.

The procedure of the experiment was to first take a pump-only shot with Janus to measure the SRS noise level and spectrum from the plasma. In princi-

ple for a Raman amplification experiment there should be almost undetectable traces of SRS noise since the seed should be created to assume that role and induce the energy transfer. But in practice it is necessary to measure a finite amount of noise to identify the resonant wavelength in order to ensure that the seed laser wavelength can match that resonance. After finding the resonance, we next took a seed-only shot with COMET to measure the seed energy, spectrum, and pulsewidth. Because the plasma exists only when the pump is present, the seed-only shot has the seed going into target chamber and passing through vacuum before exiting to be characterized by the diagnostics. Finally we took a full system shot, where both pump and seed lasers are present, and collected the entire set of measurements to look for evidence of seed amplification and save the data for post-processing. Once we established the routine of taking system shots, we performed a timing scan where we adjusted the arrival of the pump so that the seed would cross it inside the plasma at different times within 1 ns. This was an important step because the onset time of the SRS noise signal during that interval was unknown and had to be found since the plasma conditions continually change over the course of 1 ns. By doing this we identified the optimal “delay” for the seed and verified that the seed was indeed coincident with the onset of SRS noise and could be amplified at the appropriate time for resonance. Setting up an experiment of this complexity was a very time-consuming process and took several weeks to complete. The COMET seed laser could fire once every 4 minutes which allowed us to take many seed-only shots and consistently reproduce the broad seed laser spectrum with 150 psi of  $N_2O$  gas that we chose to use inside the Raman cell. But the Janus pump laser was designated to firing on average one system shot per hour since the laser system must cool down after shots and the beam is time-shared with other labs in the facility. Therefore, out of the limited number of system shots we took, most were dedicated to properly

setting up the experiment, changing the Helium gas jet pressure and pump laser energy to search for the SRS noise signal, and doing the timing scan once that signal was found. We note that we were just aiming to find a large enough signal to work with and did not have enough shots to conduct a comprehensive timing scan to make a plot of signal level versus delay.

After we identified the best “delay” for the seed laser we fixed that particular timing (keeping in mind the possibility of timing jitter) and moved on to the primary data collection part of our experiment, which was a seed energy scan. From the tedious process of searching for the SRS noise, we found that maximizing the pump laser energy at 232 J and maximizing the gas jet pressure at 1450 psi allowed us to observe the noise, so we fixed those settings and the rest of the settings in the experiment. Then for the energy scan we fixed the original COMET laser energy entering the Raman cell and varied the converted seed energy by placing combinations of neutral density filters in the beam path just before the seed entered the target chamber. With this arrangement our experiment was set up to address the issue of how seed amplification changes with increasing seed energy and if saturation of the energy gain could occur at higher seed energies. All in all we took slightly less than 70 Janus shots and a little over 130 COMET shots during our entire experiment, and we were fortunate to be able to work through the problems and collect some meaningful data points towards the end of the experiment.

### 5.3 Experimental results

In this section we present the primary results of the seed amplification experiments. The file-naming convention was established so that each shot is labeled as Shot [Janus shot number] -- [COMET shot number], e.g. Shot 67 -- 132. The

data is collected to help identify in energy gain scaling for short 0.67 ps and long 3.7 ps seed pulses. The autocorrelation measurements taken in the seed generation experiment have produced these respective pulsewidths coming out of the Raman cell. We start with Figure 5.4 which shows a sample interferogram from one of the data shots. The raw interferograms were quite distorted, especially at the edges, which made it very difficult to analyze the fringes to obtain a phase map. We suspect that this distortion comes about because the plasma is strongly perturbed and heated by the large energy, long pump laser. The final density profiles in Figure 5.5 were taken as lineouts at 11 degrees from the longitudinal axis of the Abel-inverted phase map to best reproduce the density structure that the seed propagated through. But because we had to make some assumptions about the fringe positions, the sharp drop on both edges of the post-processed density profiles may not be the actual drop-off in the real plasma. Figure 5.5 shows the density profiles Besides the uncertainty in density at the edges of the plasma the density profiles in the middle show consistent nonuniformities from shot to shot, with an overall decrease in density from the side of the plasma that the pump laser enters. We could not pinpoint a specific reason for this result but expla-

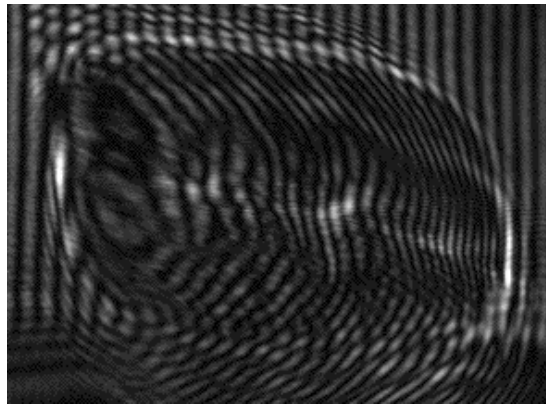


Figure 5.4: Typical plasma density interferogram.

nations ranging from laser pressure causing expansion of the plasma to practical inhomogeneities in the gas flow from the nozzle were considered. Nonetheless, knowing this we were still interested in seeing if a nonuniform plasma could still support seed amplification.

Figure 5.6 shows the four most meaningful short pulse amplification shots which we collected that provided evidence of seed amplification. Each shot shows the initial seed spectrum, the SRS noise spectrum, and the final seed spectrum. Although the intention was to take a noise spectrum measurement with each system shot, time constraints prevented us from doing so and thus Shot 61 -- 123 is plotted with one noise spectrum and Shot 64 -- 126, Shot 65 -- 129, and Shot 67 -- 132 is plotted with another noise spectrum. The vertical axis in all these spectral plots are given in raw counts. On the top right of each spectrum, we show oscilloscope photodiode traces corresponding to the time of arrival of

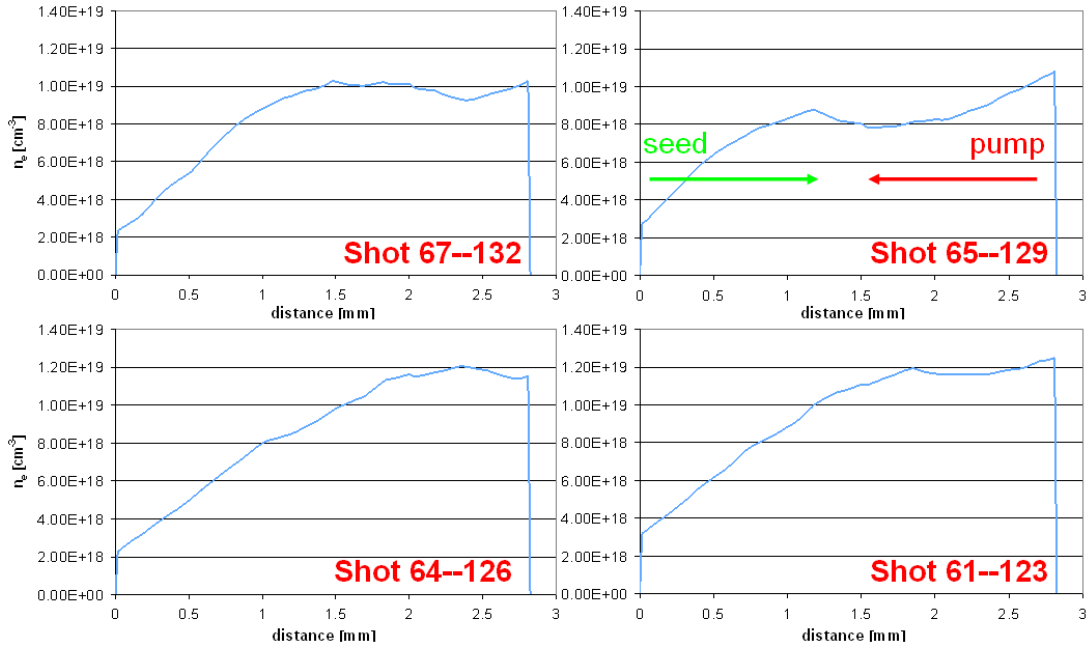


Figure 5.5: Post-processed plasma density profiles.

the Janus pump (in green), the SRS noise (in purple), and the COMET seed (in yellow). Since the photodiodes all have a very long response time compared to the pulsewidths of the lasers, we look at only the time of the initial rise of the waveform. This allows us to compare the relative timing between signals. As we mentioned earlier, we expected that a seed entering the plasma at a delay of around 200 ps would be best for amplification and these waveforms agree with our expectations, keeping in mind the  $\pm 100$  ps timing jitter. To look at the data from another perspective, Figure 5.7 overlays the initial and final seed spectra from three of the shots along with the SRS noise on top of each other. Again

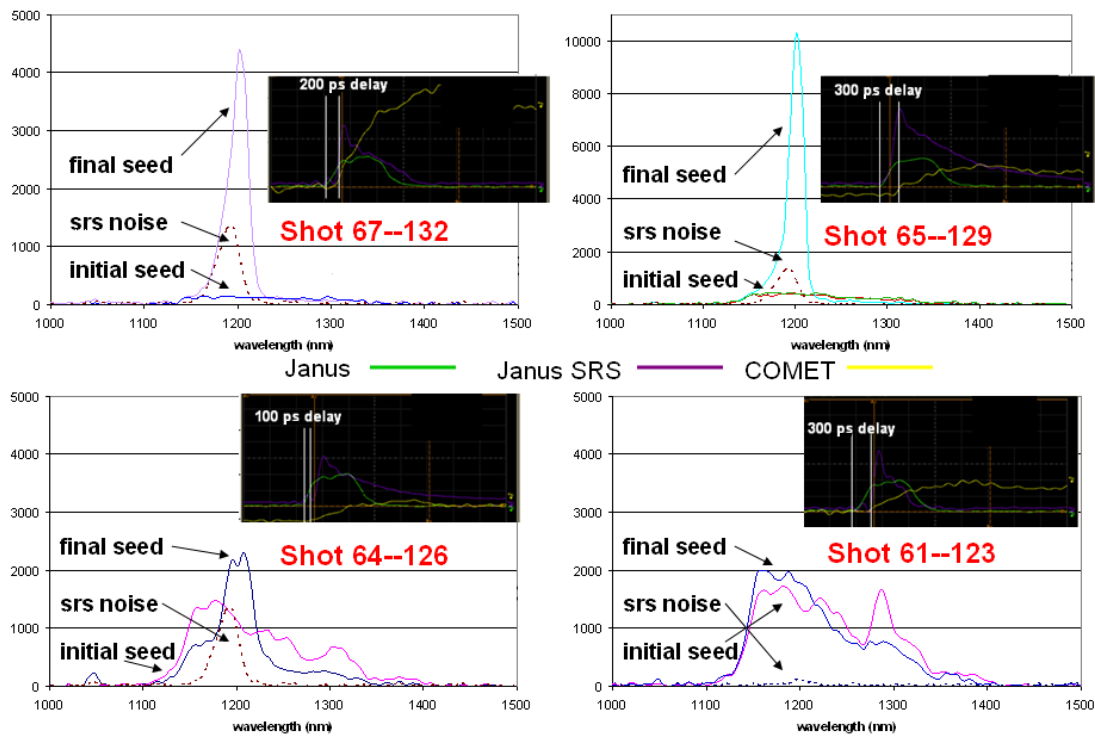


Figure 5.6: Experimental results of short pulse seed amplification with vertical axis in raw counts. The initial seed energies are:  $5.88 \mu\text{J}$  (top left),  $54.4 \mu\text{J}$  (top right),  $160 \mu\text{J}$  (bottom left),  $228 \mu\text{J}$  (bottom right)

the vertical axis is in raw counts. Since the energy we get from the calorimeter reading is distributed over the entire broad spectrum of the seed, plotting in counts rather than energy allows us to directly overlay multiple seed spectra for purposes of comparison. Doing this makes it clear that the final seed spectra of the higher amplification shots are narrower and have more of a Lorentzian line-shape than those of lower amplification shots. Furthermore we find that the peak of all the spectra are centered around 1200 nm, which verifies the wavelength of the resonance. Although the peak of the SRS noise is shifted by about 7 nm, we checked that the resolution of our fiber spectrometer is 7 nm, so for all practical purposes we can take these peaks to be the same and call 1200 nm our resonant wavelength.

In order to quantify the amplification and determine the energy gain for each shot we had to convert raw counts into a quantity called peak spectral energy with units of J/nm. We can show how we did this with an example using the SRS noise signature from a pump-only shot. As shown in Figure 5.8, we integrated the area underneath the raw spectrum to get the value in units of counts-nm. We then took the calorimeter energy reading on that shot and divide it by this area to end up with a scale factor in units of J/(counts-nm). Finally we took the original raw spectrum in counts and multiply through by this scale factor to get the peak spectral energy. We followed this same procedure to convert the rest of the data shots into J/nm, and this allowed us to obtain the amount of energy at one particular wavelength, namely 1200 nm. The reason we used the SRS noise spectrum as our example is that to properly quantify the energy gain we must subtract out the noise energy from the total output energy at 1200 nm. In our experiment we observed that the SRS backscatter goes in many directions so that the energy must have been sprayed backwards at various angles. Since the collection optics for transport out of the chamber were set up only along the

beam path of the seed, we only collected the fraction of the overall noise that followed the seed out of the chamber. It was this amount of energy that was subtracted from the final seed before calculating the net output seed energy and the energy gain. Figure 5.9 shows these results for output seed energy plotted versus input seed energy for the short pulse amplification. The shaded green diamonds represent the peak spectral energy plot, but we also plotted the integrated output seed energy versus input seed energy to see if the results would be different. The integrated energy was obtained by integrating over a 40 nm bandwidth around 1200 nm instead of just taking the peak energy at 1200 nm. What we verified was that Shots 67 -- 132, and 65 -- 129 show narrow spectral amplification while Shots 64 -- 126 and 61 -- 123 show broad spectral amplification. This was apparent since the former two data points had a larger discrepancy between the peak spectral point and the integrated point, while the latter two data points had better agreement between those points. This is consistent because we expect the peak energy gain to deviate from the integrated gain if the spectrum were narrow, and converge towards the integrated gain if the spectrum were broad. Unfortunately, limitations on our user time in the facility prevented us from being more thorough in our energy scan and taking multiple shots at each energy to get better statistics on shot to shot fluctuations of energy gain. Knowing that the plasma density may be nonuniformly changing on each shot and that there is jitter in the timing system, it is very possible that the energy gain could fluctuate if we had multiple shots at one energy. The two obvious cases of this are Shots 64 -- 126 and 61 -- 123 have output energies approximately equal to their input energies which suggest there was no gain on those shots. We believe that density nonuniformity rather than seed absorption in the plasma plays the dominant role for these no gain results, but we will study the possibility of absorption via simulations in the next chapter. If there is some absorption of the seed, we will

need to redefine amplification to mean the energy gain relative to the partially absorbed seed instead of the energy gain relative to the unattenuated seed. Doing this will actually give energy gains greater than what we have shown in our data. But the overall behavior we have observed is that the amplification seems to saturate for higher initial seed energies much like the behavior observed in the long pulse experiments which we show in Figure 5.10 plotted only in terms of peak spectral energy. We are also left to speculate that there may be a correlation between larger gain and narrow spectral amplification (Shots 67 -- 132, and 65 -- 129) and smaller gain and broad spectral amplification (Shots 64 -- 126 and 61 -- 123). Saturation of amplification becomes more clear when we plot the data from both short pulse and long pulse experiments together. To do this we have to convert everything into intensity in order to factor in the pulsewidths. Since the autocorrelation measurements from the shots indicated that the amplified pulsewidths did not change very much from the initial pulsewidths of 0.67 ps and 3.7 ps for short and long pulses respectively, it is straightforward to make an output peak intensity versus input peak intensity plot which we show in Figure 5.11. We use a log-log plot for the intensities to show how the seed intensity gain decreases for increasing input intensities when both short and long pulses are employed. Because the short pulse is approximately 5 times shorter than the long pulse we find that this saturation can occur on both faster and slower time scales. The circled short pulse points are the ones which we claim some uncertainty in gain but the overall trend from all the points is still suggests that saturation does indeed occur, which is the main finding of our experiments.

Figure 5.12 shows a side by side tabular comparison of the parameters and results from the three previous Princeton experiments in blue columns [8, 9, 10] and our 2008 long pulse [62] and 2009 short pulse experiments at LLNL in yellow columns. The Princeton experiments were discussed back in Chapter 1 so

here we will just point out some aspects that differentiate our experiment from theirs. Besides the different pump and seed wavelengths, we have a much larger energy pump and a larger spot size. Our pump laser has a significantly longer pulsewidth which produces hotter temperatures in our plasma. Because of this we operate primarily in the strong damping regime with a  $k_2\lambda_D$  at least twice as much as theirs. We need to keep in mind that the term Raman amplification technically refers to the seed beam growing large enough to deplete the pump beam and amplifying to intensities at least several times the initial pump intensity coupled with some amount of pulse shortening. The 2005 and 2008 Princeton experiments claim to be in the pump depletion regime by measuring shorter output pulsewidths, but otherwise it's not very straightforward to prove that pump depletion has occurred. In our case the initial seed is not intense enough and the plasma is strongly damped, so we do not expect any global depletion of the pump. But bright intensity speckles could perhaps cause local depletion of pump in several tiny speckle areas to get gain in various parts of the seed beam. This issue is addressed in the next chapter through simulations.

As a lead-in to the next chapter, we show Figure 5.13 which on the left gives a seed spot size lineout taken with a 1D Hamamatsu C8061 InGaAs photodiode detector. Because it's a linear array we deduce the spot transverse profile by means of circular symmetry. Filamentation of the pump beam is a serious issue in these types of experiments since it will cause spatially non-uniform amplification and spraying of the seed pulse. We will calculate the intensity threshold for pump filamentation and show that our pump intensity is below that threshold. Figure 5.13 lends some support of this conclusion by showing that the amplified seed profile is similar to the initial seed-only profile. It also shows from earlier measurements that the amplified bandwidth is about 40 nm FWHM which verifies the width of our amplified seed spectra. From here we will try to provide

more insight into our experimental results in Chapter 6 using 2D simulations.

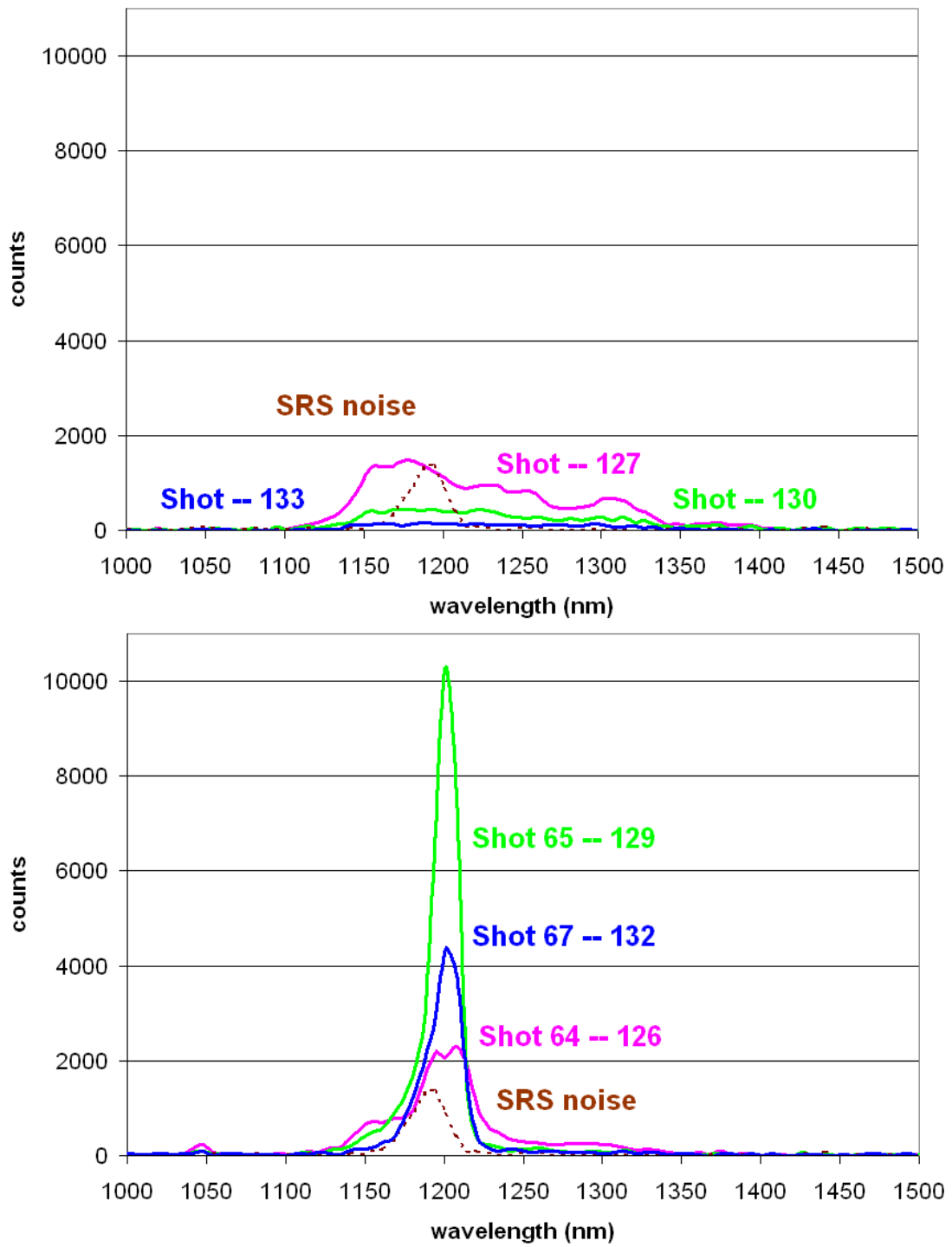


Figure 5.7: Overlaid raw seed spectra for shots 64 -- 126, 67 -- 132, and 65 -- 129 along with SRS noise spectrum before (top) and after (bottom) amplification.

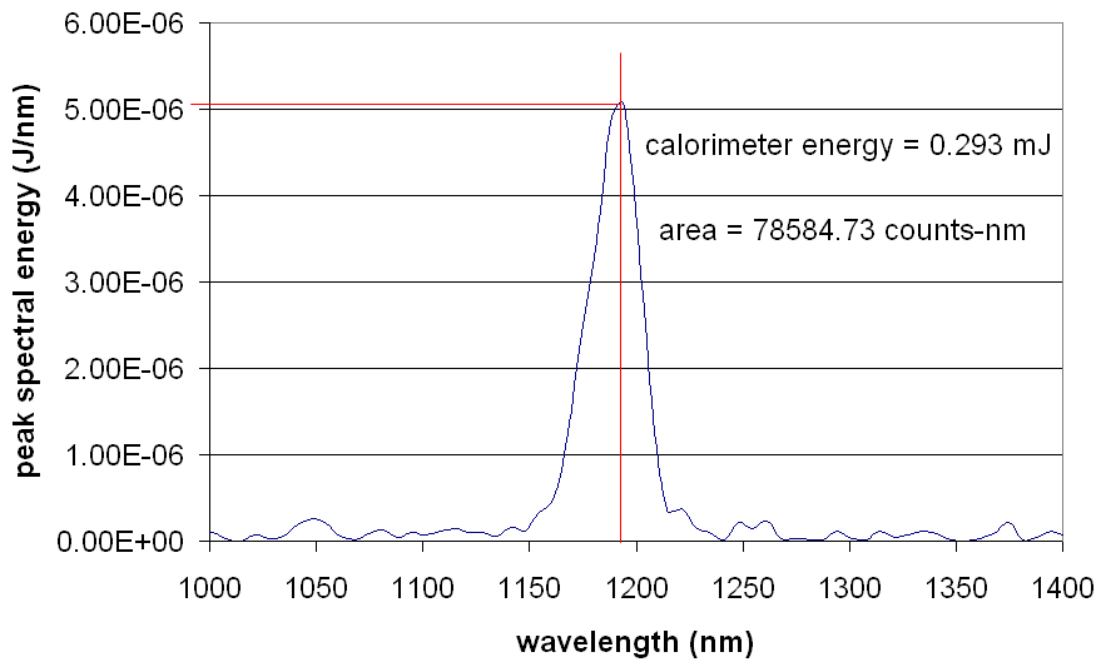


Figure 5.8: SRS noise spectrum in terms of peak spectral energy.

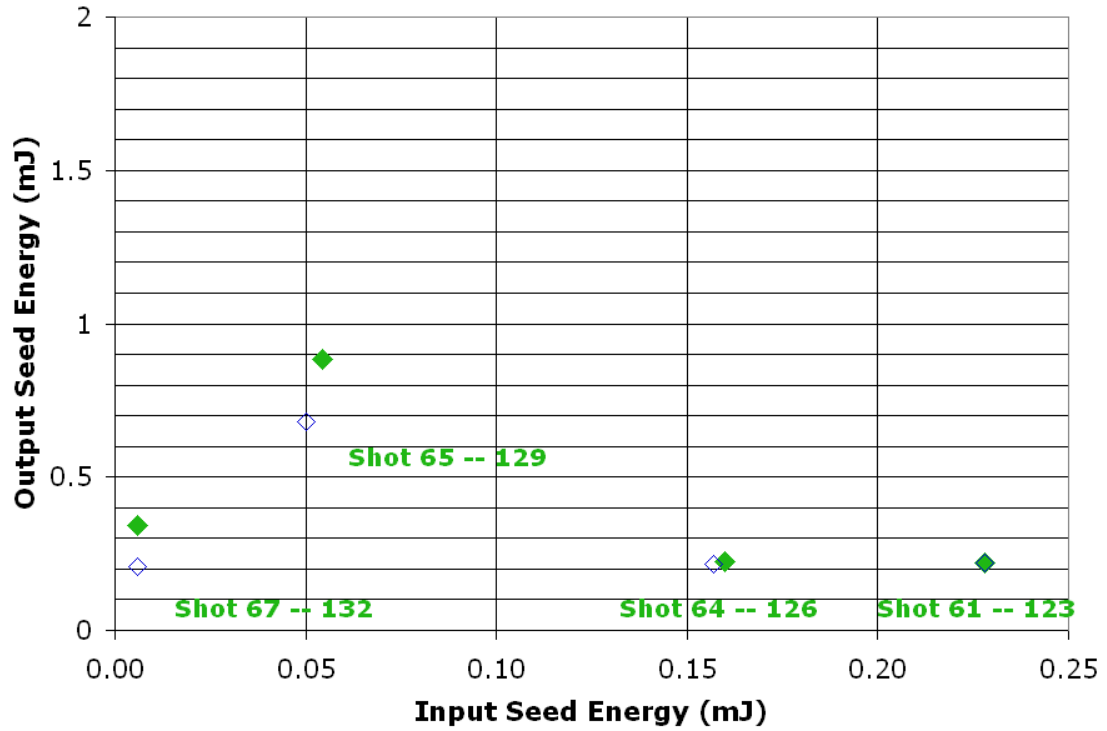


Figure 5.9: Short pulse seed amplification results. Peak spectral energy is shown in shaded green diamonds and integrated energy is shown in blue outlined diamonds.

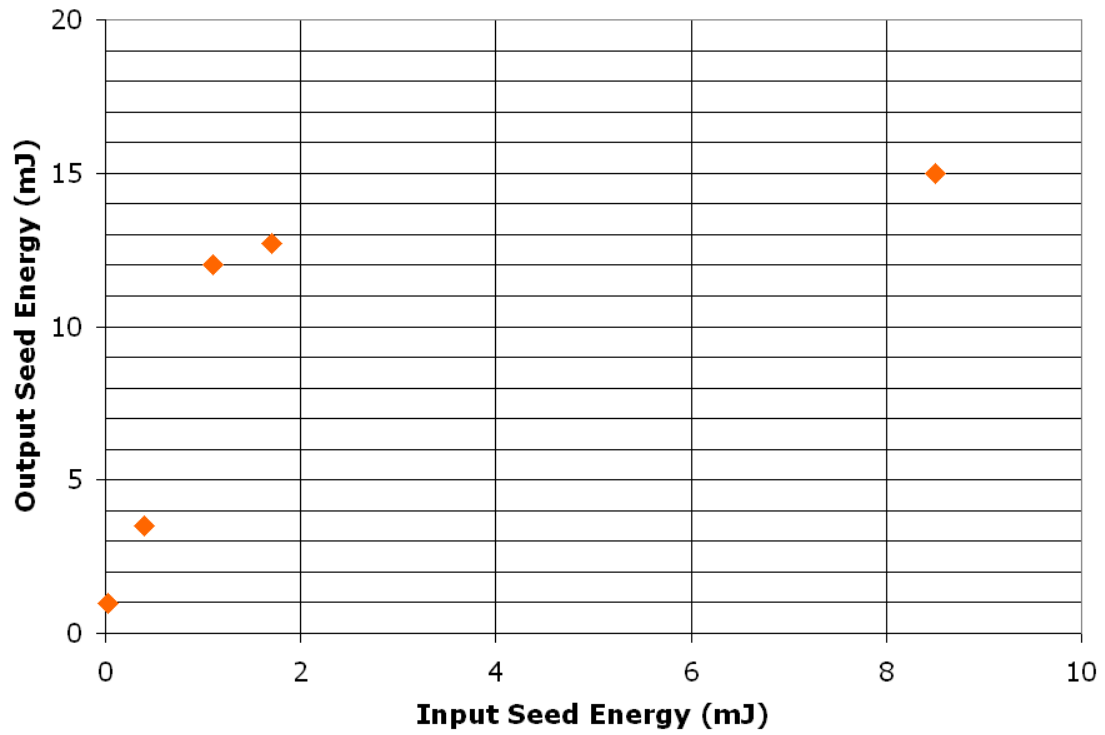


Figure 5.10: Long pulse seed amplification results. Peak spectral energy is shown in shaded orange diamonds.

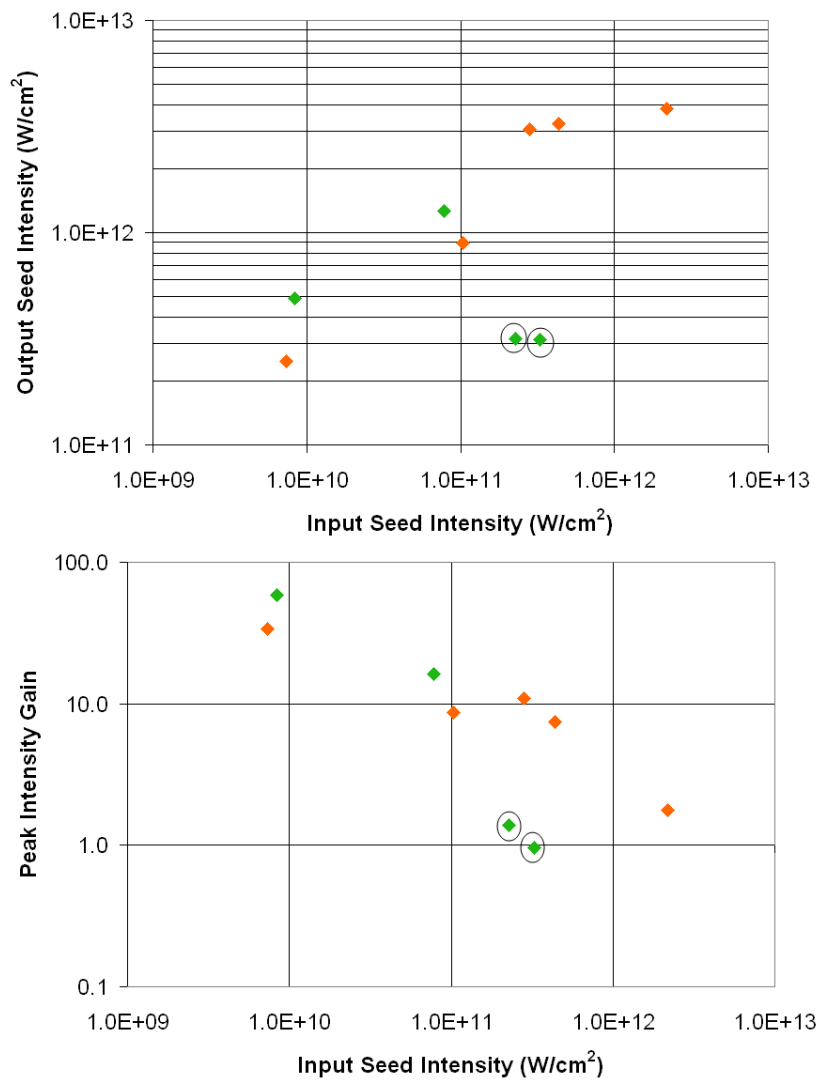


Figure 5.11: Plot of output peak intensity (top) and intensity gain (bottom) versus input peak intensity. Short pulse data are shown in shaded green diamonds and long pulse data in shaded orange diamonds. The two short pulse points with uncertainty in the gain are circled.

	Y. Ping et. al. PRL 2004	W. Cheng et. al. PRL 2005	J. Ren et. al. PoP 2008	2008 LLNL Experiment	2009 LLNL Experiment
Pump $\lambda$ (nm)	800	800	803	1054	1054
Seed $\lambda$ (nm)	860	873	878	1220	1194
Pump $\tau$ (ps)	10	10	20	1000	1000
Pump energy (mJ)	15 $w_0=15 \mu\text{m}$	40 $w_0=15 \mu\text{m}$	90 $w_0=27.5 \mu\text{m}$	232,000 $w_0=250 \mu\text{m}$	232,000 $w_0=250 \mu\text{m}$
$k \lambda_D (T_e)$	<0.24 (<50 eV)	<0.24 (<50 eV)	<0.24 (<50 eV)	<0.4 (<300 eV)	<0.5 (<300 eV)
Initial seed energy (mJ)	0.005 $w_0=15 \mu\text{m}$	0.0075 $w_0=15 \mu\text{m}$	0.016 $w_0=27.5 \mu\text{m}$	1.7 $w_0=250 \mu\text{m}$	0.0544 $w_0=250 \mu\text{m}$
Final seed energy (mJ)	0.048 $w_0=15 \mu\text{m}$	0.45 $w_0=6.5 \mu\text{m}$	5.6 $w_0=7.5 \mu\text{m}$	12.7 $w_0=250 \mu\text{m}$	0.884 $w_0=250 \mu\text{m}$
Pump intensity (W/cm <sup>2</sup> )	$1.5 \times 10^{14}$ $a_0=.0083$	$1 \times 10^{14}$ $a_0=.0068$	$2.3 \times 10^{14}$ $a_0=.01$	$1.11 \times 10^{14}$ $a_0=.0094$	$1.11 \times 10^{14}$ $a_0=.0094$
Initial seed intensity (W/cm <sup>2</sup> )	$1.5 \times 10^{11}$ $a_0=.00028$	$1.6 \times 10^{12}$ $a_0=.00094$	$1.3 \times 10^{12}$ $a_0=.00085$	$4.36 \times 10^{11}$ $a_0=.00068$	$7.77 \times 10^{10}$ $a_0=.00028$
Final seed intensity (W/cm <sup>2</sup> )	$1.44 \times 10^{12}$ $a_0=.00088$	$1.7 \times 10^{15}$ $a_0=.03$	$4 \times 10^{16}$ $a_0=.15$	$3.26 \times 10^{12}$ $a_0=.0019$	$1.26 \times 10^{12}$ $a_0=.0011$

Figure 5.12: Comparison of parameters between the Princeton and LLNL experiments.

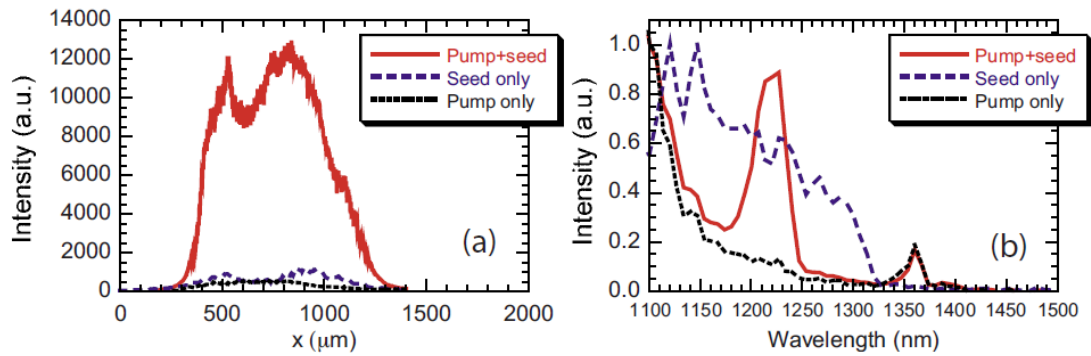


Figure 5.13: 1D photodiode lineout of the seed spot profile and amplifier bandwidth measured from a pump and seed spectrum. Reprinted with permission from Y. Ping, R. K. Kirkwood, T.-L. Wang, D. S. Clark, S. C. Wilks, N. Meezan, R. L. Berger, J. Wurtele, N. J. Fisch, V. M. Malkin, E. J. Valeo, S. F. Martins, and C. Joshi, *Phys. Plasmas* **16**, 123113 (2009). Copyright 2009, American Institute of Physics.

## CHAPTER 6

### Experimental Results Compared to Simulations

In this chapter we develop scaled-down 1D and 2D models of our experiment and employ computer simulations to produce numerical amplification data that may be compared to the experimental data points. Since we mentioned in Chapter 5 that a specialized optic known as a phase plate was used with the pump beam in our experiment, we start this chapter by discussing speckles in laser beams and describing what a phase plate is and how it works.

#### 6.1 Description of phase plates

One of the natural phenomena associated with coherent light is that the light reflecting from or transmitting through a surface with roughness features larger than an optical wavelength will acquire various intensity patterns known as speckles [73]. In a typical high power laser system, techniques such as spatial filtering are used to clean up the laser beam so that the intensity is as uniform as possible and high intensity fluctuations will not damage the optical components in the system. However, even though the laser beam coming out of the final amplifier of a laser system has a relatively uniform intensity, its phase is nonuniform. This is because the beam has only a finite coherence and a transverse coherence length much less than the aperture size at the output. In addition this nonuniform phase profile can vary from shot to shot. Because of this phase nonuniformity in the

near field, the beam can develop regions of intensity hot spots in the far field [74]. These local increases in intensity can result in filamentation and self-focusing of the beam thereby resulting in intense speckles that can activate SRS instabilities in LPI if the intensity reaches above a certain threshold [75].

To counteract this effect specialized fused silica optics called phase plates were developed to provide a certain degree of spatial smoothing in intensity to the beam in the far field. Phase plates installed in laser systems introduce a prescribed optical phase shift that varies across the beam's transverse dimension. The individual phase plate elements will shift the phase of the light at each transverse location by different amounts in accordance with the varying thicknesses of the elements. Each element acts as a diffracting aperture that splits the beam into many beamlets, and since phase plates are commonly used in conjunction with a focusing lens, the interference between all the dephased coherent beamlets results in a statistical re-distribution of intensities in the far field. The distribution is deterministic, resulting in many diffraction-limited speckles arranged in a fine-scale pattern in the beam spot with modulation by a large-scale intensity envelope. The resulting beam profile is therefore much smoother than the original beam, since the intensity in the original hot spots have been re-distributed throughout the beam. Figure 6.1 gives a schematic of a generic phase plate along with a focusing lens and speckles in the far field. The F-number is defined as  $F = f/D$ , where  $D$  is the diameter of the laser beam and  $f$  is the effective focal length of the lens. As drawn in the figure each speckle has a characteristic longitudinal correlation length  $z_c$  and a radial correlation width  $\rho_c$  [76]. The speckle parameters  $z_c$  and  $\rho_c$  are defined based on the size of the lens and the lens aperture shape. The general relations that we use to estimate the speckle size in our pump beam are  $z_c = 8F^2\lambda = 8(10)^2(1.054 \mu\text{m}) = 843 \mu\text{m}$  and  $\rho_c = F\lambda = (10)(1.054 \mu\text{m}) = 10.5 \mu\text{m}$ . Using phase plates allows the creation of large diameter beams much larger

than the diffraction limit. Otherwise the spot size is determined primarily by the F-number of the focusing optic. Since the final spot size is inversely proportional to the size of the beam at the phase plate element, spots of various diameters can be produced by changing the beam size. Large spots provide more speckles for better statistical averaging and can also reduce the intensity on target for a fixed amount of power. Another benefit of phase plates is that they can be used to create a super-gaussian or a flat-top intensity profile resulting in better beam uniformity without having to move the lens to defocus the beam.

The phase plate design method takes a desired intensity profile in the far field and uses modern optics theory to back-calculate what the phase profile in the near field should be in order to produce that result. The design process usually involves many iterations that eventually converge on the best way to tailor the phase information of the beam so that most of the intensity is contained within a desired region. The first ever phase plate was a random phase plate (RPP) [77]

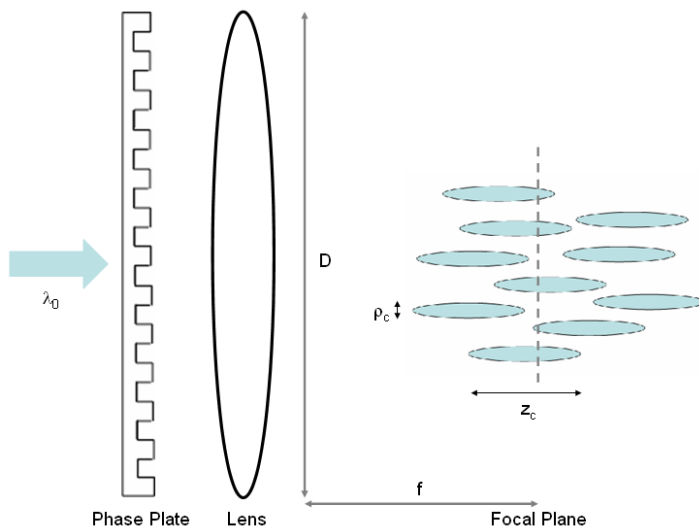


Figure 6.1: Cartoon drawing of a phase plate with a focusing lens and speckles at focus.

developed in Japan. The RPP is a binary phase plate providing either a 0 or  $\pi$  phase shift using a two-dimensional array of square elements arranged in a checkerboard pattern to systematically scramble the phase of the beam in the near field. An upgrade to the RPP was later developed at LLNL and named the kinoform phase plate (KPP) [78], which uses smoothly varying instead of discontinuous phases so the shape of the focal spot could be better controlled. The continuous phase plate (CPP) also made at LLNL is similar to the KPP but has its substrate carved in a more continuous fashion, allowing the intensity in the tail to be diffracted toward the middle to make a better flat-top profile. Since KPPs and CPPs are typically hard to fabricate, the phase zone plate (PZP) was developed [79]. Its geometry consist of tiny Fresnel zone plates embedded inside hexagonal elements. It overlaps focusing and defocusing beams to make a flat-top profile based on intensity averaging, and thus provides similar functionality to the KPP while being much easier to fabricate.

In the next section we will show the results of 1D and 2D computer simulations that use our experimental parameters. When doing the 2D simulations we include a random phase plate on the pump beam in an attempt to model the experiment more realistically. We will show that when a RPP is used the pump does not filament or spray thus maintaining the integrity of the amplified seed. Because in principle the seed should have as smooth of a profile as possible with minimal intensity non-uniformities, we model the seed as a perfect Gaussian beam in our simulations.

## 6.2 1D OSIRIS and 2D pF3d simulations using experimental parameters

In addition to our experiment we also took a computational approach to study seed amplification. To do this we ran sets of computer simulations in one and two dimensions. For the 1D simulations we used the PIC code OSIRIS. Because of the computational demands of PIC codes, we make a very reasonable assumption in order to use PIC to simulate our experiment, and that is to use a 20 ps top-hat pump pulse with a 5 ps rise and fall on both sides rather than the whole 1 ns pump pulse. This model is based on the reasoning that since the 1 ns laser is the same laser used to create the plasma in addition to acting as the pump, only the peak portion of the pulse actually interacts with the seed laser. With the length of the plasma being 3 mm, complete interaction of the two pulses in a counter-propagating geometry only requires 20 ps of the pump pulse to interact with the seed after the plasma is made via collisional ionization (which happens within the first couple of hundred picoseconds of the pump). We also had to make assumptions on some physical parameters, namely having a piecewise density ramp approximating the density profile obtained from interferometry and prescribing a uniform temperature throughout the plasma. Finally we note that the seed used in the simulation was monochromatic at the resonant wavelength instead of broad spectrum, and this may lead to over-estimation of the amplification in the simulation.

The simulation setup is as follows. The simulation box contains 925000 cells. The dimension of the box is  $95670.84 c/\omega_0$  in the x direction. Length units are normalized to  $c/\omega_0$  ( $0.17 \mu\text{m}$ ) and time units are normalized to  $1/\omega_0$  ( $0.56 \text{ fs}$ ) of the 1054 nm pump laser. The time step used is 0.055 fs and the total simulation time is 53.6 ps. The longitudinal cell size  $\delta x_1$  is  $0.1034 c/\omega_0$ , which corresponds

to 60 cells per pump laser wavelength. A 3 mm plasma piecewise density profile is located between  $38890.88 c/\omega_0$  and  $56779.96 c/\omega_0$  with vacuum regions on both sides. The density profile was modeled after the interferometry measurements in the experiment and ranges from  $2 \times 10^{18} \text{ cm}^{-3}$  at the low end to  $1.1 \times 10^{19} \text{ cm}^{-3}$  at the high end, as shown in Figure 6.2. The temperature is  $T_e$  is uniform at 280 eV. Inside the plasma region only the electrons are allowed to move and the ions serve as a fixed neutralizing background. The vacuum regions are wide enough to contain the entire pump and seed after they leave the plasma slab. The simulations are set up such that the peak of the seed pulse meets the beginning of the pump plateau at the left edge of the plasma slab (at  $38890.88 c/\omega_0$ ). Both lasers are linearly polarized parallel to each other with the seed going towards the right and the pump going towards the left. The pump intensity of  $1.11 \times 10^{14} \text{ W/cm}^2$  and  $a_0 = 0.0094$  is prescribed throughout the flat region with the scaling of energy in 20 ps that gives the same intensity as in 1 ns for a  $500 \mu\text{m}$  FWHM spot. Meanwhile the seed has a Gaussian longitudinal profile with either a 0.67

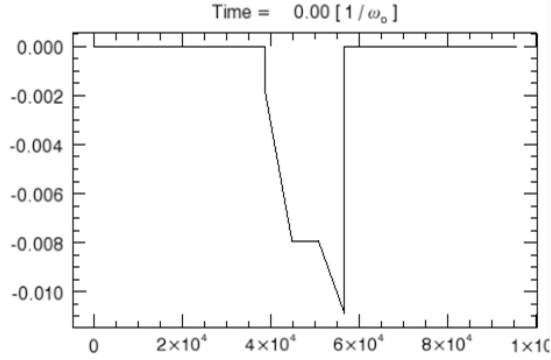


Figure 6.2: Piecewise density profile used in the simulations shown in Figure 6.3. Negative signs indicate that the values refer to the electron density. The vertical axis is in units of critical density, which is  $1 \times 10^{21} \text{ cm}^{-3}$ . Areas having zero density correspond to vacuum regions.

ps (short) or 3.7 ps (long) pulsewidth. The simulation box contained 64 particles per cell and features such as quadratic splines and current smoothing were turned on to reduce the intrinsic numerical noise.

We did a set of short pulse runs and long pulse runs. For short pulses we started with an initial seed energy of  $5.88 \mu\text{J}$  in a  $500 \mu\text{m}$  FWHM spot, giving an intensity of  $8.4 \times 10^9 \text{ W/cm}^2$  with  $a_1 = 0.000093$ . Subsequent larger energies of  $54.4 \mu\text{J}$ ,  $160 \mu\text{J}$ , and  $228 \mu\text{J}$  in a  $500 \mu\text{m}$  FWHM spot gave intensities of  $7.77 \times 10^{10} \text{ W/cm}^2$ ,  $2.29 \times 10^{11} \text{ W/cm}^2$ , and  $3.26 \times 10^{11} \text{ W/cm}^2$  respectively and those corresponded to  $a_1 = 0.000283$ ,  $a_1 = 0.00049$ , and  $a_1 = 0.00058$  respectively. For long pulses we did similar calculations to get the intensities of  $7.37 \times 10^9 \text{ W/cm}^2$  ( $28.7 \mu\text{J}$ ),  $1.03 \times 10^{11} \text{ W/cm}^2$  ( $400 \mu\text{J}$ ),  $2.82 \times 10^{11} \text{ W/cm}^2$  ( $1100 \mu\text{J}$ ),  $4.36 \times 10^{11} \text{ W/cm}^2$  ( $1700 \mu\text{J}$ ), and  $2.18 \times 10^{12} \text{ W/cm}^2$  ( $8500 \mu\text{J}$ ). This corresponded to  $a_1 = 0.0000875$ ,  $a_1 = 0.0003265$ ,  $a_1 = 0.0005414$ ,  $a_1 = 0.0006731$ , and  $a_1 = 0.0015$  respectively. Even though the intensities were calculated assuming a Gaussian profile in the transverse direction, the 1D OSIRIS simulation has infinite plane wave lasers and thus no transverse effects such as filamentation, diffraction, and focusing of the pump and seed beams are taken into account. Also the 1D nature of the simulation neglects the fact that the seed intersects the pump at a small angle from the direct counter-propagating direction. Hence we can only expect rough correspondence to within an order of magnitude between the predictions of 1D OSIRIS and the values measured in the experiments.

Figure 6.3 shows the initial and final seed waveforms for sample runs taken from the set of short and long pulse cases corresponding to the data points in our experiment. For each case a reference simulation was run without the seed pulse so that thermal Raman backscatter from the pump could be measured and later subtracted from the final seed before calculating the net gain. Upon doing this we found the backscattered noise to be very small and because of this the

peak intensity gain can practically be calculated as the ratio of the maximum of  $a_1$  for the final seed to the maximum of  $a_1$  for the initial seed and squaring the result. In regards to the thermal fluctuation level from the pump going at the near back scattering angle of 11 degrees, we expect that its spectral power density will deviate from that of direct back scattering by only a few percent and still be too small to have any impact on the calculation of the seed amplification. From these images we observe that the pump laser is hardly depleted which implies that the driven plasma wave amplitude is relatively small. This is consistent with our conclusion of what happened in the experiment since we did not obtain

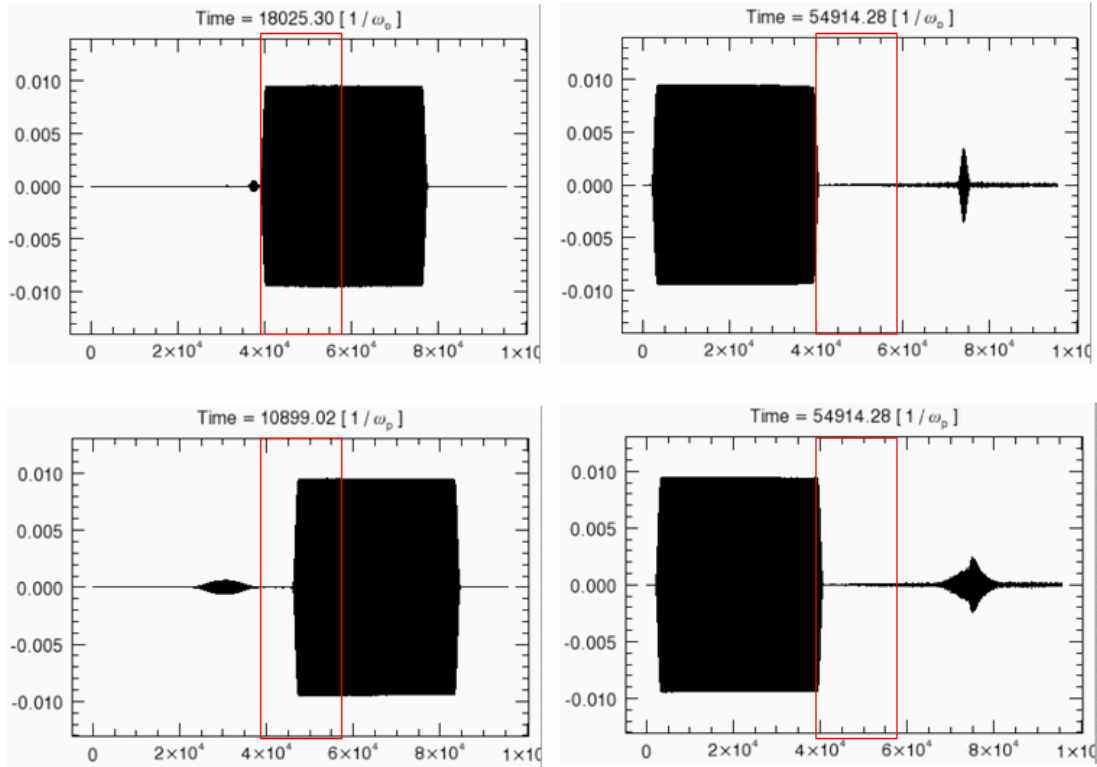


Figure 6.3: Initial and final seed amplification results in a 1D OSIRIS run for the 0.67 ps,  $3.26 \times 10^{11} \text{ W/cm}^2$  (top) and 3.7 ps,  $4.36 \times 10^{11} \text{ W/cm}^2$  (bottom) cases. The plasma slab is indicated by the red rectangle.

large seed amplification in any of our shots. As shown in the top of Figure 5.11 from the previous chapter, none of the final seed intensities surpassed the initial pump intensity of  $1.11 \times 10^{14} \text{ W/cm}^2$ . We are not surprised by this result since we have already characterized our plasma conditions and determined that the Raman backscatter process in our plasma would be strongly damped. It also doesn't help matters that we have a broad spectrum seed containing very low energy to begin with since the spectral energy at the resonant wavelength is not intense enough to induce pump depletion. After running the simulation for all of the energies in the short and long pulse data points we plotted the results to look for trends in the gain as a function of seed intensity. In Figure 6.6 the graph of peak intensity gain versus input seed intensity from 1D OSIRIS is plotted along with the experimental data points from the bottom of Figure 5.11. We find that for both the short and long seed pulses the gain appears to first increase and then decrease as the initial seed intensities get larger. Also shown in Figure 6.6 are the corresponding 2D pF3d results, which we will discuss next.

We use the fluid code pF3d (parallel filamentation 3D) [80] as another approach to simulate our experiment. The code is inherently 3D but we use the 2D version so that we will simulate just one of the transverse dimensions. Using pF3d allows us to simulate a larger-scale, multi-dimensional problem in a reasonable amount of time and we can obtain a first order understanding based on linear calculations and paraxial propagation. This is a useful tool for simulating the physics of wide laser beams as they propagate through long lengths of plasma where the beam diameters are several hundred  $\mu\text{m}$  (in our case 500  $\mu\text{m}$  FWHM). The code, which was developed at LLNL [81], is a massively parallel multi-dimensional code with a nonlinear fluid plasma model that simulates laser beam propagation to study dynamics such as filamentation, self-focusing, and bending of the laser as it interacts with large underdense thermal plasmas

in different ICF conditions. The code couples its plasma model with a paraxial model of the laser light and other stimulated electromagnetic waves, thus allowing for studies of the effects from stimulated Raman and Brillouin backscatter. Although pF3d is primarily used for single laser beam simulations, it has the capability to include monochromatic seeded SRS light and we turn on this feature for our studies of seed amplification.

The code takes initial laser and plasma conditions as input parameters. It takes the input electric field of the laser and the plasma conditions and self-consistently simulates the evolution of the laser beam as it travels through the plasma. The laser light propagates in the paraxial approximation and interacts with the plasma via the ponderomotive force and inverse bremsstrahlung absorption. The input near field laser profile can be prescribed as having passed through a final focusing lens and a phase plate on its way to interacting with the plasma. As mentioned in the previous section, phase plates perform smoothing of the laser beam by scrambling the phase of different portions of the beam to lessen the tendency for beam filamentation and spray in the far field. The code can simulate both ideal Gaussian intensity profile beams and beams fitted with phase plates [82]. For phase plates, in particular the RPP, the numerical model is a raised cosine function to the fourth power, which closely approximates a flat-top intensity profile. However we should mention that since pF3d is a paraxial code, it has a dominant wavevector in one direction for the light waves. Therefore the numerical advection portion of the code is correct for the primary longitudinal direction of laser propagation, but performs less accurately for lasers incident at steep transverse angles (i.e. angles greater than 15 degrees from the primary axis). For our case in which we have the pump and seed lasers crossing each other at a shallow 11 degree angle, the code is adequate since it is less than 15 degrees. In all of our simulation results the longitudinal direction is Z and the

transverse direction is Y, with the unit of distance being one pump wavelength (1054 nm). The pump enters the box from the  $Z = 0$  side (bottom) and propagates toward maximum  $Z$  (top) and the seed travels in the opposite direction. The pump and seed are both initialized to propagate at a 5.5 degree angle to the axis going down the middle of the box, thus making a 11 degree angle with each other. The pump enters the plasma in a  $F = 10$  geometry while the seed enters in a  $F = 20$  geometry and the Rayleigh length for both lasers is much longer than the plasma due to their large spot size. The initial plasma conditions can be specified based on experimental data or imported from radiation hydrodynamic codes such as HYDRA. In our case we use input from the former and set up a preformed plasma filling the entire box having a piecewise-linear density profile approximating that obtained from interferometry and a uniform plasma temperature throughout. The pump beam is modeled as a 0.5 ps rise followed by a long top-hat while the seed is a Gaussian with pulsewidth of 0.67 ps (short pulse) or 3.7 ps (long pulse). As in 1D OSIRIS we employ the assumption of a long top-hat pump pulse instead of the entire 1 ns pump pulse. The simulation box containing the 500  $\mu\text{m}$  FWHM spot is large enough by itself to make the simulation very large, so we stay with our 3 mm interaction length assumption. The interaction time in the plasma is then short enough that the plasma will not hydrodynamically expand by more than a few percent and inverse bremsstrahlung absorption of the laser beams is less than 1% under these conditions. The code also has an internal Langmuir wave source that can be activated so that the simulation starts with a small finite amount of Langmuir wave noise in the plasma, which is calculated from the fluctuation dissipation theorem [87].

However the pF3d code has one major drawback in that it uses a linear Landau damping operator that may not be very accurate in high  $k_2\lambda_D$  regimes. It doesn't take into account kinetic and nonlinear Landau damping effects such as particle

trapping and frequency shift of the plasma wave, both of which can modify the Landau damping rate. It also doesn't account for the possibility of wavebreaking. Because our main purpose in using this code is to study the dynamics of the laser beams in response to disturbances in the plasma, we will keep this discrepancy in mind when we look at its predictions for our experiment. Having said this we should point out that current efforts are underway [83] to use PIC simulations to explore the growth and saturation of parametric instabilities and to incorporate those results into developing reduced model kinetic mechanisms to put into pF3d to enhance its predictive capability in the nonlinear LPI regime [84]. It is anticipated that these efforts will enable better modeling of problems such as Raman backscatter, and in our case backward Raman amplification. Nonetheless the code has been benchmarked against earlier plasma flow experiments performed at the NOVA laser facility at LLNL [85] and more recent backscatter experiments with gas-filled hohlraums performed at the OMEGA laser facility at the University of Rochester [86]. The fact that it's a 3D wave-based LPI simulation code incorporating accurate hydrodynamic plasma profiles and linear plasma wave response has made it an integral part of the simulation effort at LLNL for modeling NIF target point designs in the linear regime where plasma waves are not saturated. Furthermore the NIF beams have very large spot sizes which keeps their overall intensity low to mitigate the development of nonlinear LPI as much as possible, and these conditions lead to more confidence in using pF3d.

Before doing the full runs, we performed a couple of checks regarding the SRS noise from the pump and the absorption of the seed inside the plasma. As a check of the amount of SRS backscattered noise, we ran the simulation with only the pump having an intensity of  $1.11 \times 10^{14} \text{ W/cm}^2$ . We did this to verify that the SRS noise level is below threshold for significant Raman growth, since the growth is exponential above threshold. As the left side of Figure 6.4 shows,

the code predicts that the SRS noise is almost negligible, being  $10^{-7}$  to  $10^{-6}$  times the initial pump intensity. Because the simulation did not show any SRS noise while the experiment measured a small finite amount, this indicates that the experimental diagnostics are more sensitive than simulations. We then did a seed-only run to check for possible attenuation of the seed due to collisional absorption as it travels through the plasma by itself without being amplified. Even though our calculation of the absorption coefficient suggested that the seed pulse is not absorbed in the plasma, this run was done for verification purposes since even moderate absorption can change how we quantify the amplification of the seed. The right side of Figure 6.4 shows 99% of the seed still transmitting through the plasma and we verified that any absorption is negligible and the amplification can indeed be taken as the ratio of the output seed intensity to the input seed intensity. We next ran a set of simulations for all of the energies in the short and long pulse data points. Figure 6.5 shows the images of the results for a sample short pulse case and long pulse case. In these runs we see that the speckles in the pump beam have lengths of about  $850 \mu\text{m}$  and widths of about  $10 \mu\text{m}$ , in agreement with the  $z_c$  and  $\rho_c$  calculated earlier. For a flat-topped RPP on the pump beam, the fraction of power at a certain intensity is given by the expression  $(1+I/\bar{I})\exp(-I/\bar{I})$ , where  $\bar{I}$  is the envelope intensity [75]. Because this intensity distribution follows negative exponential statistics, it's not surprising that a small percentage of laser power is contained in intensities that are several times higher than the average envelope intensity, and this is shown as the few brighter speckles in the images. The images also show that the pump beam neither sprays nor self-focuses, which would be disastrous for amplification. The reason why this issue is of concern is that the ponderomotive force from speckles can cause electrons and subsequently ions to evacuate from local regions of the plasma, leaving density depressions. Since light bends towards regions of lower

density, refraction of the light in these density wells may dominate over the laser beam's tendency to naturally diffract and cause filamentation and self-focusing to occur. This could happen if the light intensity reaches above a certain threshold, which is quantified by the relation  $(\frac{v_{osc}}{v_{th}})^2(\frac{n_e}{n_{cr}})(\frac{L}{\lambda})^2 > 1$  [75]. Here the quantity  $L$  is the same as  $\rho_c$ . Upon substituting values from our experiment (using  $\frac{v_{osc}}{c}$  and  $\frac{v_{th}}{c}$  instead of  $v_{osc}$  and  $v_{th}$ ) we obtain  $(.00944/.0235)^2(.00796)(10^2) = 0.13$ . Since

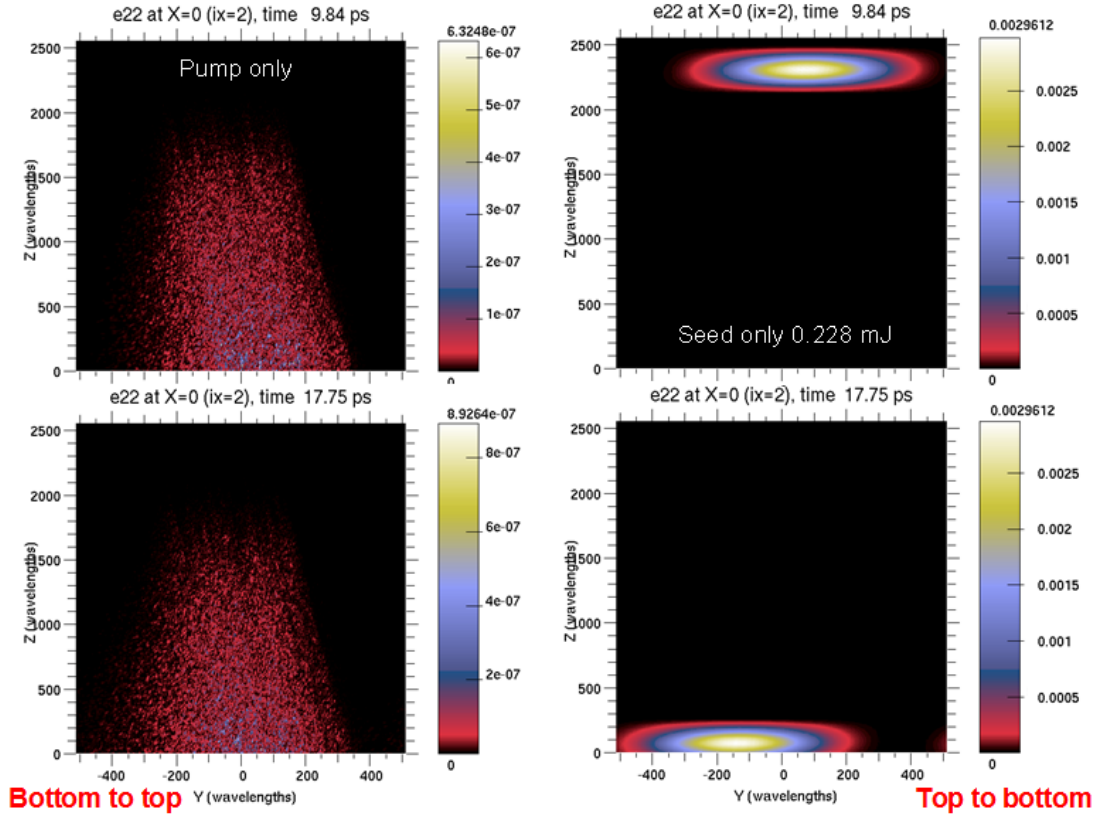


Figure 6.4: Simulations showing SRS backscattered light from the pump laser for an initial pump intensity of  $1.11 \times 10^{14} \text{ W/cm}^2$  (left) and 99% transmission of an unamplified 0.67 ps,  $3.26 \times 10^{11} \text{ W/cm}^2$  seed passing through the plasma (right). Length scales are in terms of pump wavelengths and intensities in the color table are normalized to the initial pump intensity of  $1.11 \times 10^{14} \text{ W/cm}^2$ .

the value is less than 1, this supports the observation that self-focusing does not occur. Even if the condition were satisfied, self-focusing of speckles can only happen over a time interval that's long enough for ions to be expelled and create a density depression. Ions will begin to move on a time scale of  $F\lambda_0/c_s$ , where  $c_s$  is the sound speed, and for our parameters we estimate this time to be around 35 ps. Because the interaction time of the lasers in the 3 mm plasma is less than 35 ps, ponderomotive self-focusing is not likely to occur in the pump and thus the seed. Another aspect that we noticed in the simulations pertains to the amplified seed structure. What we have is a static speckle structure in far field of the pump and because the longitudinal correlation length of each speckle is slightly less than 1 mm, a several mm plasma is not long enough for a direct counter-propagating

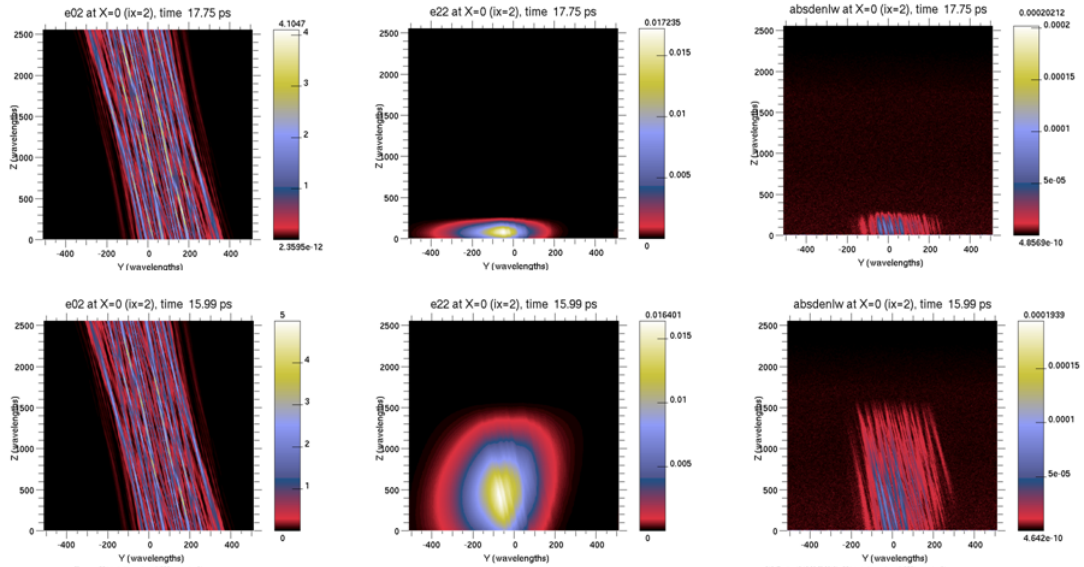


Figure 6.5: Final seed amplification results in a 2D pF3d run for the 0.67 ps,  $3.26 \times 10^{11} W/cm^2$  (top) and 3.7 ps,  $4.36 \times 10^{11} W/cm^2$  (bottom) cases. Length scales are in terms of pump wavelengths and intensities in the color table are normalized to the initial pump intensity of  $1.11 \times 10^{14} W/cm^2$ .

seed to average over many of these speckles to acquire a smoothly coherent structure. However in our simulations the seed crosses at an angle with respect to the pump and therefore effectively encounters more speckle surface area. This allows it more opportunities for averaging during its interaction with the pump beam and thus the result is a smoother intensity structure. This was the case in all the simulated data points. In Figure 6.6 we plot the results of the simulations in terms of peak intensity gain versus seed intensity to look for trends in the gain as a function of seed intensity for short and long pulse cases. The experimental data points and the 1D OSIRIS results are included for comparison. What we immediately notice is that 2D pF3d shows a nearly constant peak intensity amplification of 6 for both the short and long seed pulses. This gain is significantly lower than those of 1D OSIRIS but not so far off from some of the experimental data points. So after running both 1D OSIRIS and 2D pF3d simulations and comparing their results to the experimental data, it became apparent to us that these simulations do not quite reflect our observation of saturation of the gain for higher seed intensities. Although we would like to believe this observation and to even say that longer pulses will experience harder saturation than shorter pulses as the intensity is raised, we acknowledge that the data we obtained and the simulations we did do not provide strong enough evidence to justify this.

Although we demonstrated evidence of amplification, we were not able to take numerous data points to identify a clearer trend in the amplification. Also the seed energies that we had were very small, causing the ponderomotive force and thus the plasma wave amplitude to be small as well. So we did not have data from a wide range of energies to help us clearly identify a nonlinear saturation mechanism. We considered particle trapping as a probable contributor to saturation and analyzed our plasma density and temperature conditions to find that trapping could be a distinct possibility. Referring back to Table 5.1

from the previous chapter, we had calculated a bounce period of 0.28 ps. This makes the short pulse (0.67 ps) about 2 times the bounce period and the long pulse (3.7 ps) about 13 times the bounce period, both of which are long enough intervals to trap particles. In that event, particle trapping could be accompanied by nonlinear frequency shifts in the plasma wave frequency, which would detune the plasma frequency away from resonance. However the density profile we have is rather inhomogeneous so the degree to which bulk plasma particles are trapped may actually be smaller. On the other hand we are not surprised that some of the 2D pF3d points fall quite close to the experimental data points because the simulation is set up with parameters and geometry that more closely resemble the experimental setup, in particular its two-dimensional nature, the angle of interaction, and the RPP on the pump. As for the constant gain for all the data points, we believe that it could happen for both short and long seed pulses because there's only a linear model behind the pF3d code, and in the linear regime of BRA where there is no pump depletion, the output would be directly proportional to the input. The code will only show sizeable changes in gain for situations where the pump is significantly depleted. Therefore, as in 1D OSIRIS, we can only expect order of magnitude proximity between some of the pF3d predictions and the measured experimental results.

As another way of quantifying the discrepancy between 1D OSIRIS and 2D pF3d, we compare the plasma wave amplitudes from both codes by plotting them in terms of wavebreaking units,  $\frac{eE}{mv_\phi\omega_p}$ , where E is the electrostatic field amplitude. This is shown in Figure 6.16. What we immediately see is that 1D OSIRIS shows higher driven plasma wave amplitudes than 2D pF3d. This is actually expected because in Figure 6.6 we see that 1D OSIRIS overestimates the intensity gain because it is one-dimensional and doesn't incorporate transverse effects or phase plates. The 2D pF3d amplitudes are lower, in large part due to the

crossing angle geometry in an already inhomogeneous plasma and the dynamics of the RPP pump beam in driving the waves. Another aspect of this plot is the increased deviation among the amplitudes predicted by both codes at larger seed intensities, which leads us to suspect that the particle trapping threshold has been crossed. The wave amplitudes in long pulse OSIRIS have been driven to several times this threshold and thus are strongly interacting with the electrons to detune the wave frequency away from the ponderomotive drive. This could be responsible for the noticeable drop in the intensity gain. Conversely the long pulse pF3d amplitudes are relatively constant and below the threshold, which results in the lower constant gain. The wave amplitudes in short pulse OSIRIS exhibit similar behavior as they barely cross the threshold, and this is manifested in the slight flattening trend of the intensity gain at the larger seed intensities. On the other hand the short pulse pF3d levels out below threshold and hence the constant gain. Therefore because waves in OSIRIS cross the trapping threshold and waves in pF3d reside below it, and both models are valid in these respective regimes, it remains unclear whether particle trapping is a major factor in our experimental parameters. Thus what may be needed to be more conclusive about this issue is a simulation study using two dimensional OSIRIS with lasers crossing at an angle and a RPP on the pump.

Although we can accept the discrepancy between 1D OSIRIS and 2D pF3d results when compared to the experimental data points, we felt it was necessary to conduct another simulation exercise to compare the codes themselves since they showed disagreement when simulating the experiment. In the next section we show results from a comparative study strictly between the two codes but using a new set of simulation parameters so we can look at a case where they do agree as well as a case in which they disagree.

### 6.3 Additional BRA studies comparing 1D OSIRIS to 2D pF3d

From the previous sections in this chapter we found that both 1D OSIRIS and 2D pF3d predicted results that are quite different from one another. Whereas 1D OSIRIS indicated increasing amplification for increasing seed intensities as a result of its inherent modeling of kinetic effects, 2D pF3d showed practically constant amplification from its intrinsic linear calculations due to the fact that there was very little pump depletion. In this section we will provide further comparison between the two codes in the context of BRA in which significant pump depletion is achieved. We will present one test case in which both codes agree with each other in terms of intensity amplification and another case in which they disagree, providing explanations for the possible plasma behavior in each case. We will also include phase plates in these cases and evaluate their impact on the amplification. The parameters in the cases we choose are similar to those in Cases I and IV from Chapter 3. However, unlike in Chapter 3, where we used a plasma length long enough for the amplified seed to break apart in Case I, we use a plasma length of 1.3 mm so that the seed amplifies up a level just below the onset of breakup. This is done so that proper comparison between 1D OSIRIS and 2D pF3d can be made. We'll refer to the cases as the low  $k_2\lambda_D$  case and the high  $k_2\lambda_D$  case with the relevant simulation parameters summarized in Table 6.1.

We first show the results from 1D OSIRIS for the two cases. Figure 6.7 shows the squared electric field of the final amplified seed at the top, the amplitude of the plasma wave in the middle, and the squared electric field of the final pump at the bottom. The seed pulse is 100 fs FWHM traveling towards the right and the pump is a 100 fs rise followed by a flat-top traveling towards the left. The initial

Table 6.1: Parameters used for simulations comparing 1D OSIRIS to 2D pF3d

low $k_2\lambda_D$ case	high $k_2\lambda_D$ case
$n_e = .05 n_{cr}$	$n_e = .015 n_{cr}$
$T_e = 50$ eV	$T_e = 200$ eV
$v_\phi/v_{the} = 13.2$	$v_\phi/v_{the} = 3.4$
$k_2\lambda_D = .076$	$k_2\lambda_D = .298$
seed $\lambda_1 = 1.376$ $\mu\text{m}$	seed $\lambda_1 = 1.234$ $\mu\text{m}$
$\omega_0/\omega_p = 4.5$	$\omega_0/\omega_p = 8.2$
plasma period $2\pi c/\omega_p = 4.8$ $\mu\text{m}$	plasma period $2\pi c/\omega_p = 8.7$ $\mu\text{m}$
$\gamma_R = 6.1 \times 10^{12}$	$\gamma_R = 4.4 \times 10^{12}$
$\nu_L = 0$	$\nu_L = 5.2 \times 10^{12}$
$\nu_{ei} = 2.46 \times 10^{12}$	$\nu_{ei} = 1.74 \times 10^{11}$

seed intensity is  $1.8 \times 10^{14}$   $W/cm^2$  and the pump intensity is  $2.8 \times 10^{14}$   $W/cm^2$ . In the low  $k_2\lambda_D$  case the seed depletes the pump and forms a  $\pi$ -pulse structure. Because the  $k_2\lambda_D$  value is less than 0.3 and the ratio of  $v_\phi$  to  $v_{the}$  is greater than 10, the Landau damping rate is negligible in this case which allows the plasma wave to maintain most of its amplitude behind the seed. From this simulation we obtain a peak intensity amplification of 196, yielding a final seed intensity of  $3.5 \times 10^{16}$   $W/cm^2$ . The plasma behavior is in the fluid regime so we expect the predicted amplification to be consistent with that of a linear three wave model. This is in contrast to the high  $k_2\lambda_D$  case where the amount of pump depletion is lower and the seed develops into a single but less amplified peak. Because  $k_2\lambda_D$  is approximately 0.3 and the ratio of  $v_\phi$  to  $v_{the}$  is on the order of unity, the Landau damping rate in the plasma is comparable to the Raman growth rate as a result of a more heated plasma. We then expect that the plasma wave will have a smaller amplitude and be localized in the immediate vicinity of the seed. From this

simulation we obtain a peak intensity amplification of 67, yielding a final seed intensity of  $1.2 \times 10^{16} \text{ W/cm}^2$ . Because in this regime kinetic plasma behavior begins to take effect, it would not be surprising if the predicted amplification disagreed from that of three wave model. Therefore we run 2D pF3d simulations in order to quantify our comparison between the predictions of PIC and the three wave model.

When going to 2D pF3d we set up the simulations like in 1D OSIRIS, with the exception that both laser pulses have a  $500 \mu\text{m}$  FWHM spot diameter in the transverse direction. Because of this large spot size the Rayleigh length of the lasers is much longer than the plasma itself, and beam waists of the lasers stay constant throughout the box. In this arrangement the 2D simulation may resemble a 1D simulation along the longitudinal axis through the center of the box for runs where the lasers are directly counter-propagating. It is the value of the peak intensity along this lineout that we will take to compare to the results of 1D OSIRIS. The simulation is arranged so that the pump travels from the bottom of the box to the top and the seed travels from the top of the box to the bottom. Figure 6.8 shows the images of the pump, seed, and plasma wave at three separate times in the simulation. The pump is the leftmost column, the seed is the middle column, and the plasma wave is the rightmost column. This is the low  $k_2 \lambda_D$  case with both pump and seed having ideal Gaussian intensity profiles. We observe that there is significant pump depletion caused by the seed as it travels through the plasma. The amplified seed develops a structure that roughly resembles the horseshoe intensity profile shown in Chapter 2. This occurs because the edges of the seed are less amplified than the center since at larger radii the wings of the seed have delayed growth from the pump being less intense in those regions. In principle the intensity structure of the seed coupled with the shape of the plasma wave should be inverse to the intensity structure of the depleted pump.

But since the color scale automatically adjusts for each pump, seed, and plasma wave image, it is difficult to visualize. Thus Figure 6.9, showing color contour plots of the final seed and pump, serves as a helpful visualization aid. The seed is shown on top while the pump is shown on bottom. In this run we get a peak intensity amplification of 185, yielding a final seed intensity of  $3.3 \times 10^{16} \text{ W/cm}^2$ . Compared to the final seed intensity from 1D OSIRIS this value agrees very well, being within 6%. One interesting point we should mention is that unlike in 1D OSIRIS, the plasma wave in 2D pF3d does not extend throughout the entire plasma. This can be attributed to the fact that collisional damping occurs inside this plasma (the collisional damping rate is comparable to the Raman growth rate in this situation), which is an aspect that was not incorporated into the PIC model. Regardless, this did not impact the seed amplification very much because the damping occurred toward the region of the plasma left behind by the leading peak of the ultrashort seed. Figure 6.10 shows the result of the same simulation but with a RPP on the pump beam. The speckles in the pump have a length of approximately 850 wavelengths and a width of about 10 wavelengths. There are some particularly bright speckles, indicating that there is a small fraction of power at intensities of 4 to 5 times the average envelope intensity of the pump. We find that the shape of the amplified seed pulse does not resemble the horseshoe shape but instead has a random assortment of higher and lower amplified spikes across the diameter of the seed, varying with sections of the seed that intersect different regions of the pump. In this case there is also significant pump depletion, but the pattern of depletion is quite different from the Gaussian pump case. In addition the plasma wave looks to be partitioned into individual streaks with some streaks having higher amplitudes than others, but overall the collisional damping still manifests itself in this situation. Determining the peak seed intensity in this case is misleading because of the numerous spikes present in the seed. A

casual calculation gives a peak intensity amplification of 425, which is more than twice that of the final seed intensity in the Gaussian pump case. A more realistic estimate of the intensity amplification comes from taking a spatial average over the entire spot size and by doing so we obtain an amplification of 223, which is a factor of 2 lower. This difference between the peak and average intensities shows the complexity behind quantifying the gain when a phase plates are involved, not to mention their impact on the quality of the amplified seed wavefront as depicted in the contour plots of Figure 6.11.

For the high  $k_2\lambda_D$  case we ran similar simulations first with both pump and seed having ideal Gaussian intensity profiles and then with the pump having a RPP. Figure 6.12 shows the results when both pump and seed are Gaussian. This time we observe that there is less pump depletion and the amplified seed consists of primarily one single peak, consistent with the 1D OSIRIS result. Upon looking at the plasma wave we find its amplitude to be lower than that of the low  $k_2\lambda_D$  case and to be localized within the vicinity of the seed. Like in the 1D OSIRIS result the plasma wave does not extend throughout the rest of the plasma behind the seed, but this time the reason is not attributed to collisional damping (the collisional damping rate is 25 times less than the Raman growth rate in this situation). Landau damping may play a role in causing the plasma wave to be smaller in amplitude and damp away behind the seed because its rate is slightly larger than the Raman growth rate. Figure 6.13 shows the color countour plots of the seed and pump for this run. However the plasma wave is obviously driven larger to transfer more energy to the seed than its counterpart in 1D OSIRIS since the peak intensity amplification here is 152, giving a final seed intensity of  $2.7 \times 10^{16} \text{ W/cm}^2$ . This value is higher by almost 125%, which is clearly in disagreement with 1D OSIRIS. When doing the run with a RPP on the pump, we observed the results to be qualitatively similar to those of the RPP run for the

low  $k_2\lambda_D$  case. By looking at the images of the pump, seed, and plasma wave in Figure 6.14, we once again saw the same types of spikes in the intensity profile. Upon looking at the largest spikes we get a peak intensity amplification of 394, which is reminiscent of the intensities obtained in the low  $k_2\lambda_D$  case with RPP. Taking the spatial average over the entire spot size yields an amplification of 158, which is a factor of 2.5 lower and again shows the difference between peak and average intensities. The fact that streaks of plasma wave appear also reminds us of those in the low  $k_2\lambda_D$  case, but with Landau damping perhaps being the mechanism that damps those streaks away behind the seed. Figure 6.15 shows the contour plots which look similar to those in Figure 6.10 and not surprisingly shows that the amplified seed wavefront has spiky intensity features.

From this study we have found that 2D pF3d agrees very well with 1D OSIRIS for the low  $k_2\lambda_D$  case but disagrees significantly with 1D OSIRIS for the high  $k_2\lambda_D$  case as might be expected. To verify this expectation we inspected the peak plasma wave amplitude given by 1D OSIRIS and 2D pF3d (Gaussian pump) for both cases and converted the values into units of  $\frac{eE}{mv_\phi\omega_p}$  for comparison. For the low case we found the amplitudes to be within 6% of each other, matching the agreement in the intensity gain. For the high case we found the 2D pF3d amplitude to be twice as large as the 1D OSIRIS amplitude, which explains why the 2D pF3d predicts a higher gain. The code pF3d is founded upon the linear theory of LPI and although it's good to have an understanding based on linear calculations in the framework of a correct paraxial propagation model before addressing the nonlinearities, the results cannot be interpreted too literally. It is apparent that when kinetic effects inside the plasma play a role, 1D OSIRIS predicts less amplification than 2D pF3d because particle trapping and detuning mechanisms can prevent the plasma wave amplitude from growing large enough to completely transfer energy from the pump to the seed. From this it is clear that

more precise nonlinear modeling of SRS will be needed in pF3d if one wishes to continue simulating large scale problems involving plasma kinetic behavior. Since PIC codes have been shown to better model the nonlinearity, given that methods are implemented to reasonably suppress numerical noise, the results of both codes will have to continue to be studied together in this context. We also found that re-running the 2D pF3d simulations using a RPP on the pump beam did not provide added insight into the reason for the discrepancy between the two codes. Using a phase plate is beneficial for smoothing out intensity hot spots in a laser and lower its overall average intensity to decorrelate the coherent growth of instabilities such as SRS. But it's difficult to predict what will happen when using a RPP for BRA since the process involves stimulating backscatter with a strong coherent seed laser in an attempt to maximize gain, and the presence of a few bright speckles on the pump laser may introduce some higher intensity features on the seed. In this regard taking an average intensity may not be the best way to report gain when a beam has speckles and our simulation results with RPP is in contrast with previous fluid code results indicating that BRA can be insensitive to spatial intensity fluctuations of the laser beams in the pump depletion regime [43]. Finally we have to keep in mind that simulating BRA with a Gaussian beam represents an idealized situation. As far as the transverse profile of the amplified seed is concerned, understanding the consequences of pump beams with a RPP can help to establish a better picture of BRA.

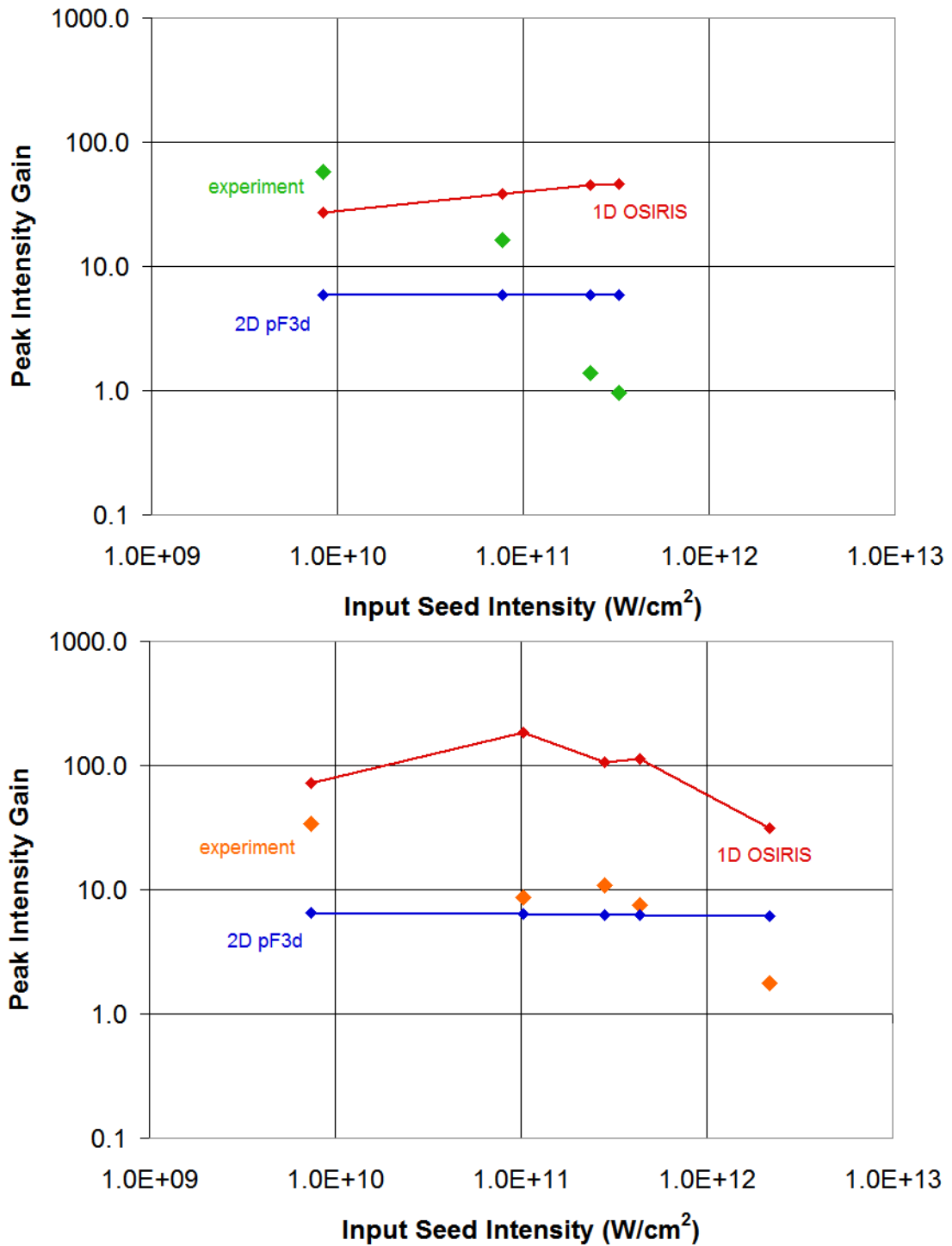


Figure 6.6: Simulation plots of intensity gain versus input peak intensity for 0.67 ps short pulse (top) and 3.7 ps long pulse (bottom) cases. Experimental data points are shown along with the 1D OSIRIS and 2D pF3d simulation data points.

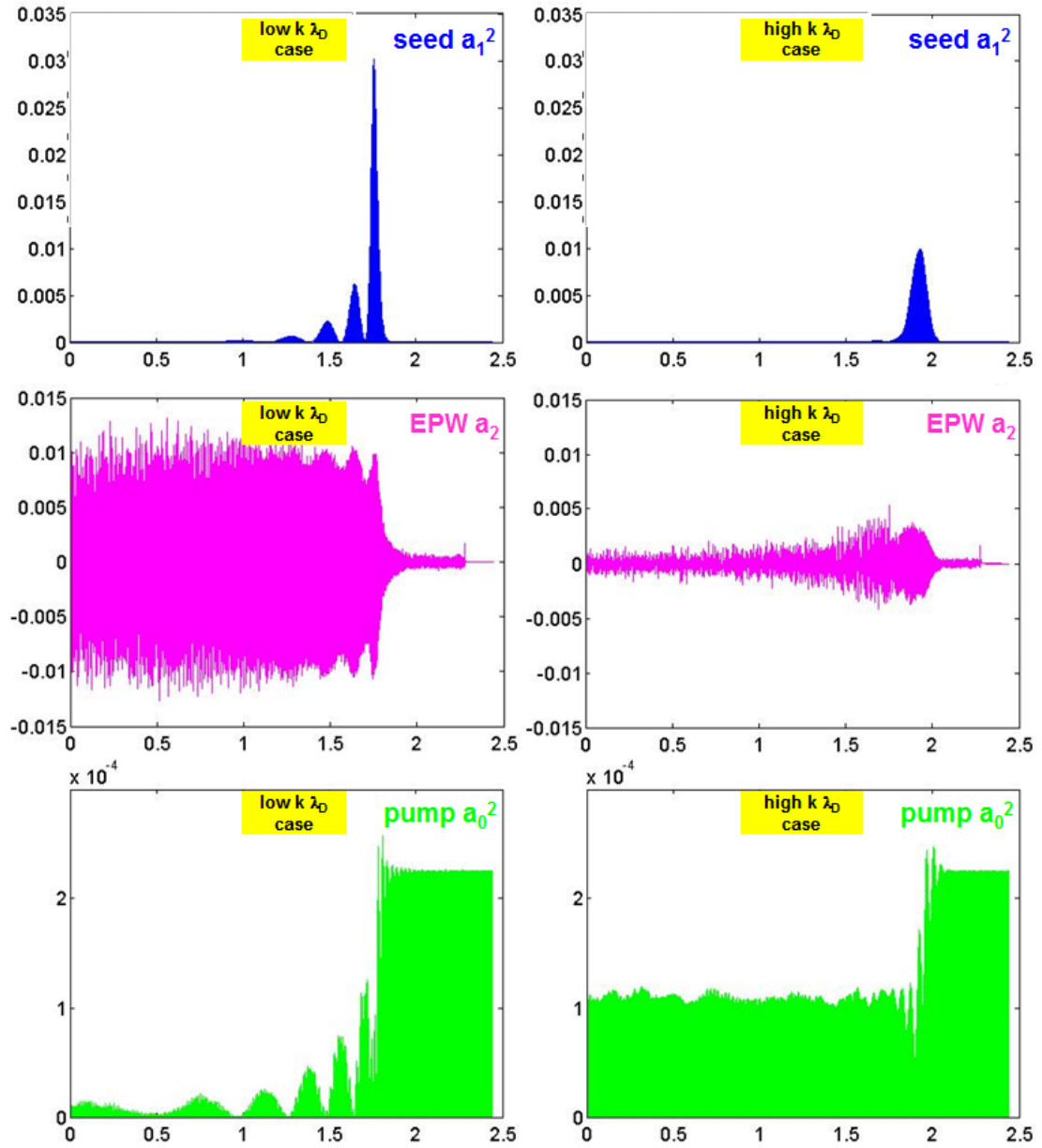


Figure 6.7: 1D OSIRIS results for both low  $k_2 \lambda_D$  and high  $k_2 \lambda_D$  cases. Shown are the squared electric field of the seed (top), the amplitude of the plasma wave (middle), and the squared electric field of the pump (bottom).

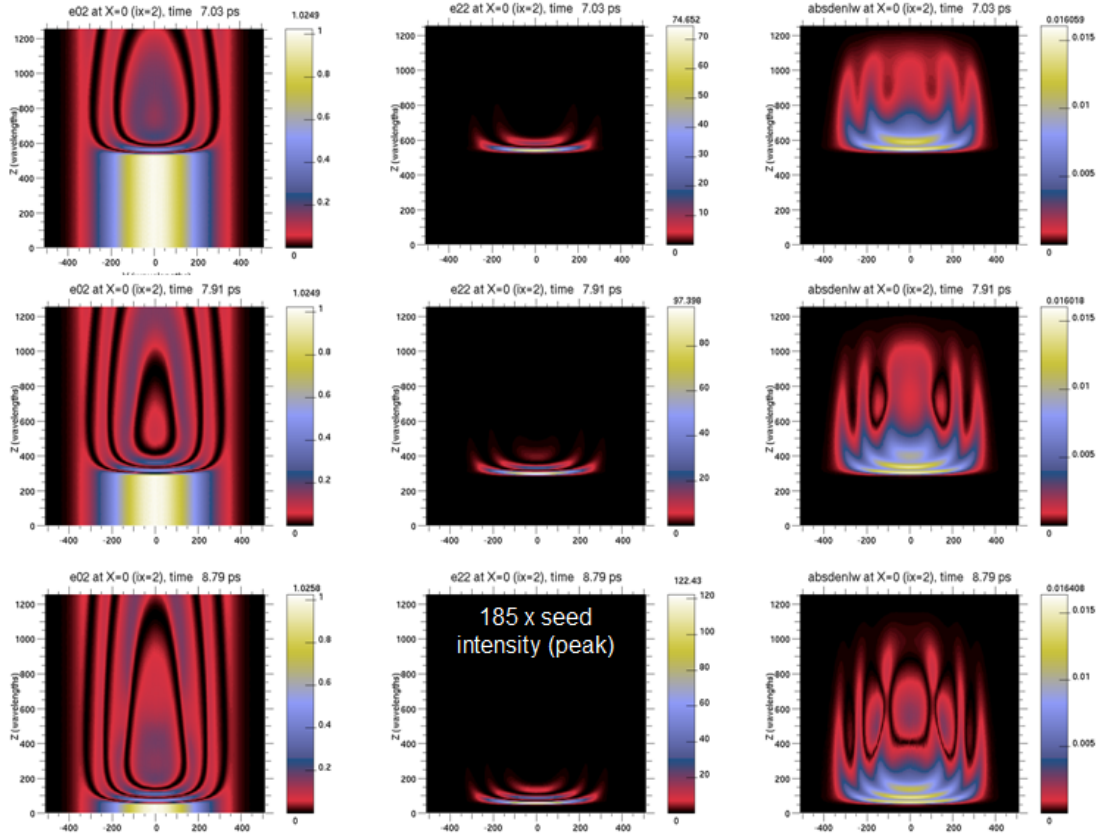


Figure 6.8: Low  $k_2\lambda_D$  case results for Gaussian pump (left column), Gaussian seed (center column), and driven plasma wave (right column). Intensities are normalized to the initial pump intensity of  $2.8 \times 10^{14} \text{ W/cm}^2$ . Plasma wave amplitudes are normalized to the critical density.

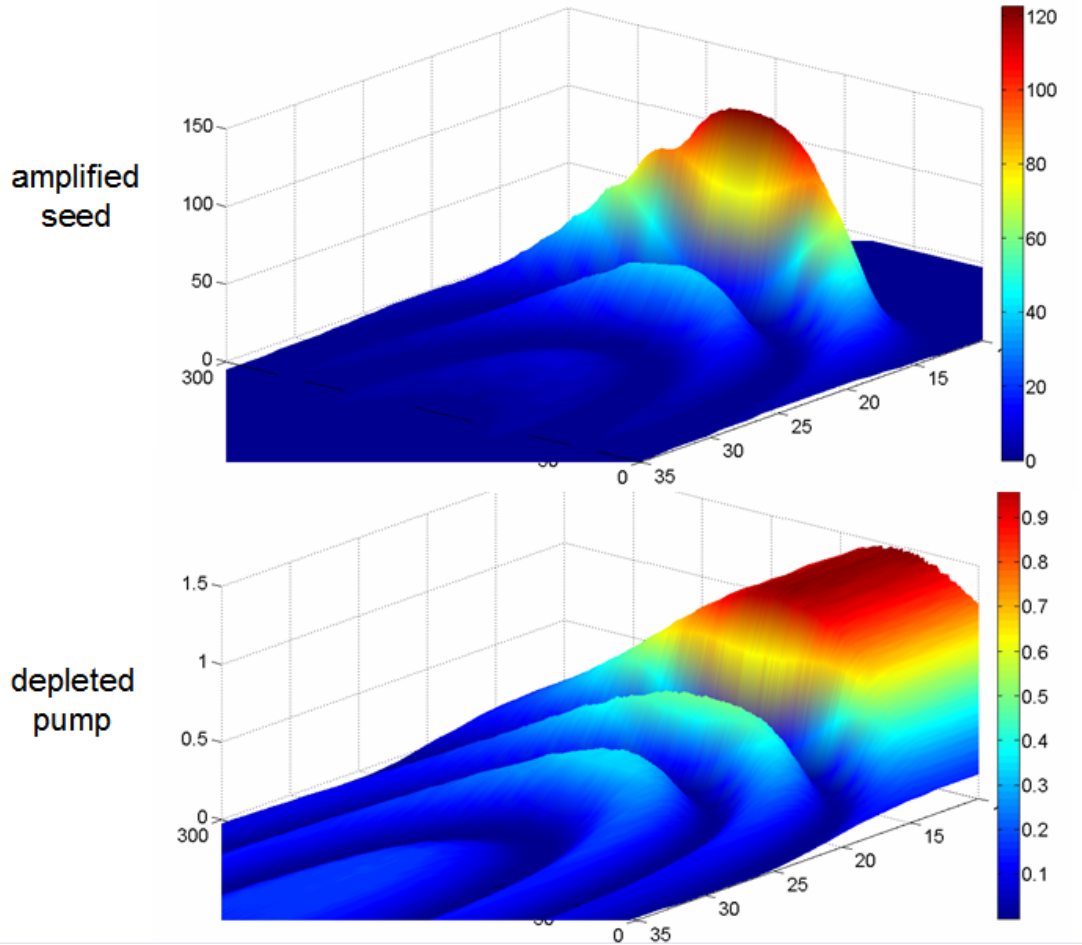


Figure 6.9: Low  $k_2\lambda_D$  case final contour plots for Gaussian pump (bottom) and Gaussian seed (top). Intensities are normalized to the initial pump intensity of  $2.8 \times 10^{14} \text{ W/cm}^2$ . The pump moves to the left in the sense of coming out of the page and the seed moves to the right in the sense of going into the page.

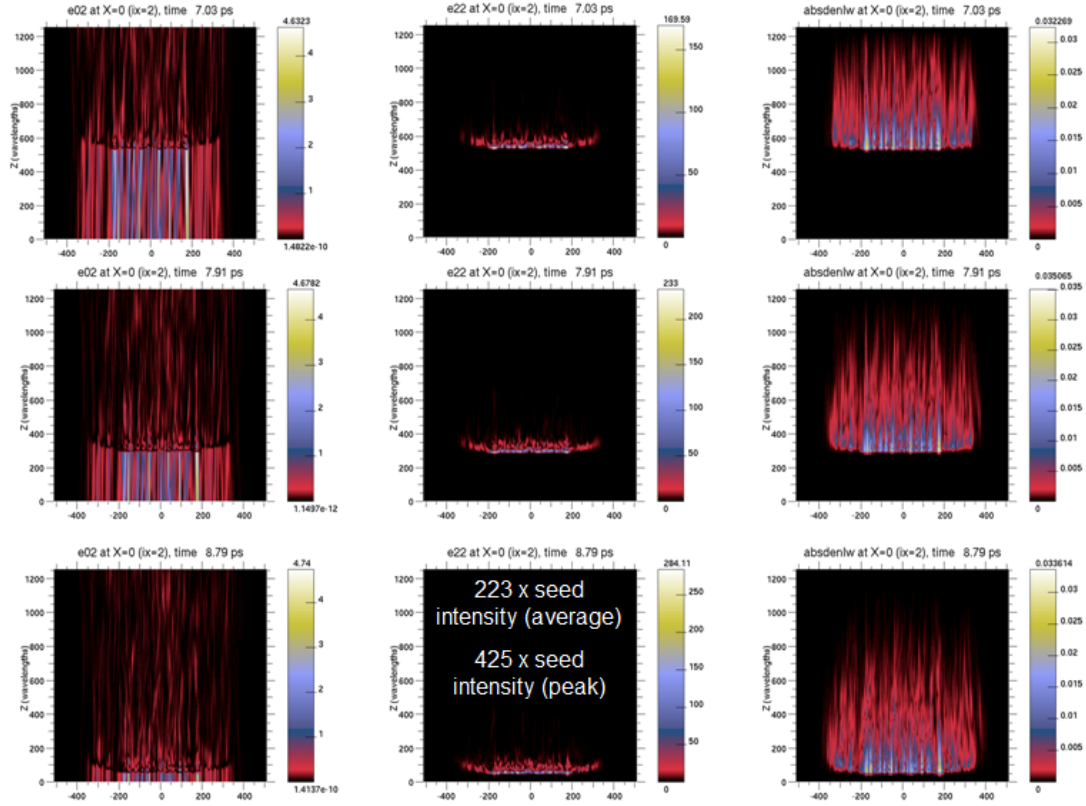


Figure 6.10: Low  $k_2\lambda_D$  case results for RPP pump (left column), Gaussian seed (center column), and driven plasma wave (right column). Intensities are normalized to the initial pump intensity of  $2.8 \times 10^{14} \text{ W/cm}^2$ . Plasma wave amplitudes are normalized to the critical density.

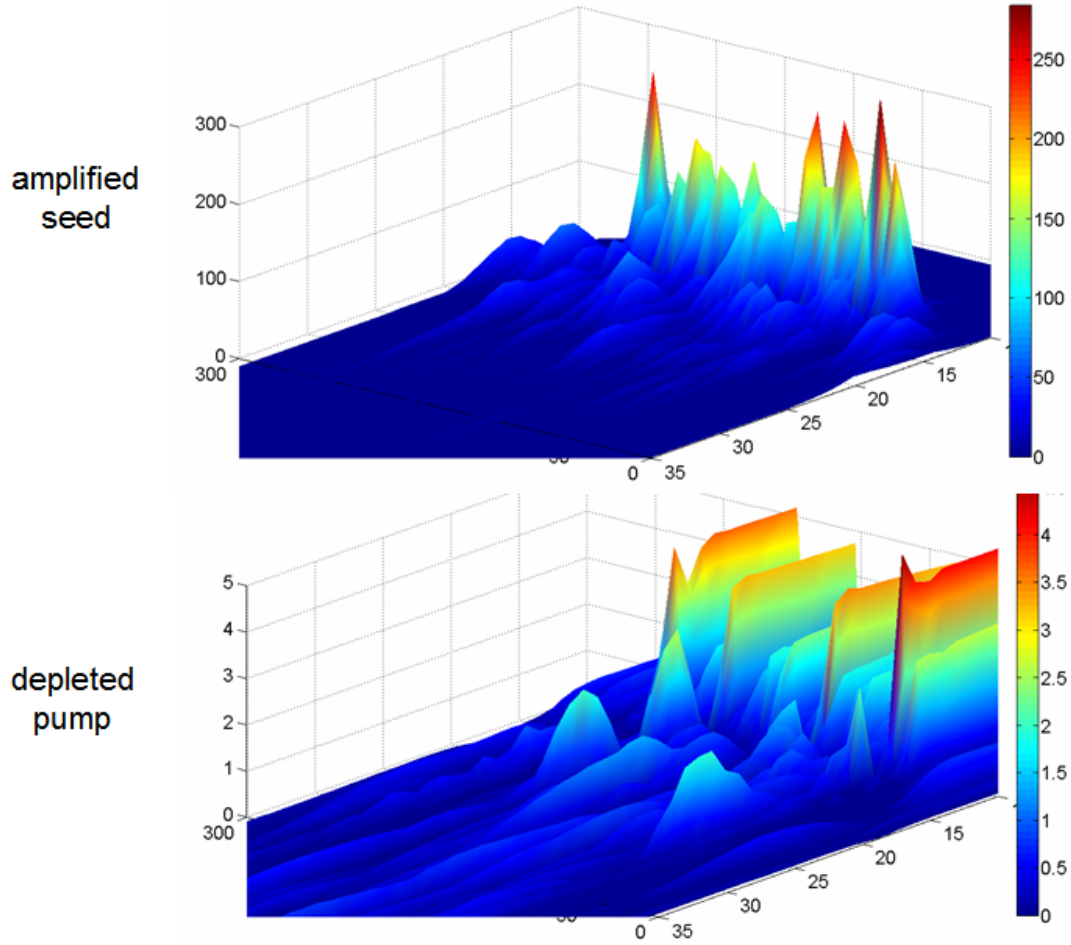


Figure 6.11: Low  $k_2\lambda_D$  case final contour plots for RPP pump (bottom) and Gaussian seed (top). Intensities are normalized to the initial pump intensity of  $2.8 \times 10^{14} \text{ W/cm}^2$ . The pump moves to the left in the sense of coming out of the page and the seed moves to the right in the sense of going into the page.

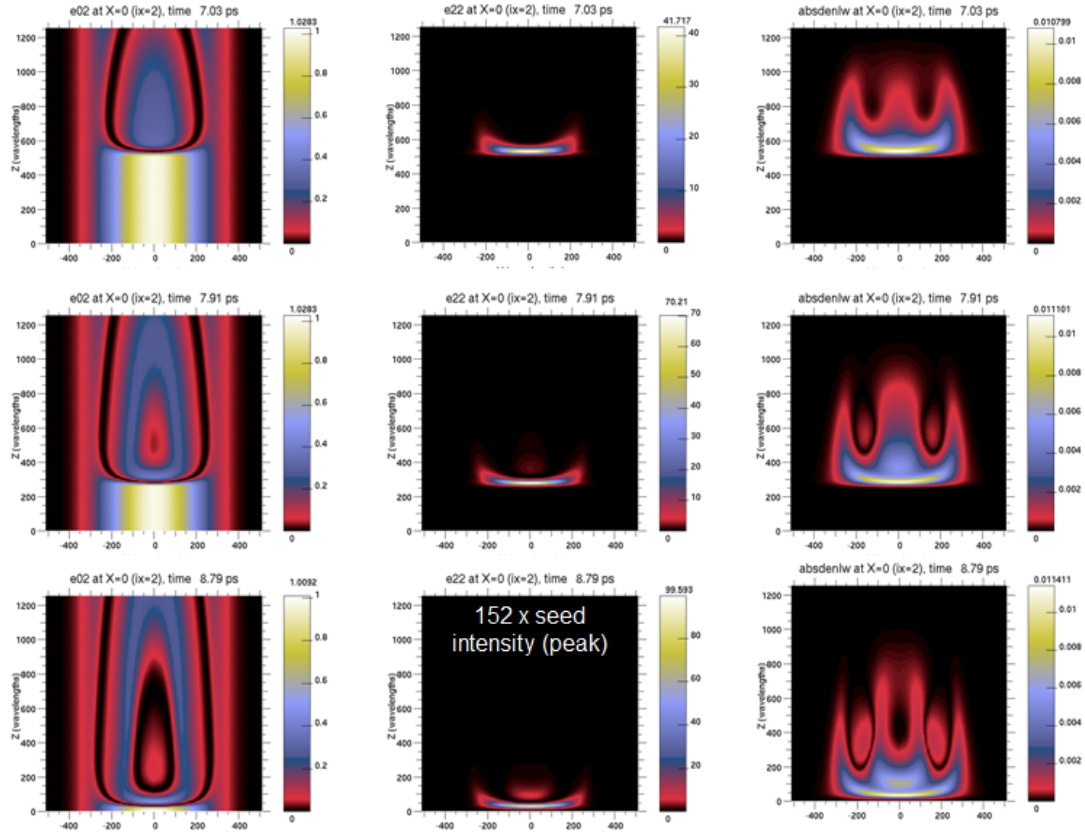


Figure 6.12: High  $k_2\lambda_D$  case results for Gaussian pump (left column), Gaussian seed (center column), and driven plasma wave (right column). Intensities are normalized to the initial pump intensity of  $2.8 \times 10^{14} \text{ W/cm}^2$ . Plasma wave amplitudes are normalized to the critical density.

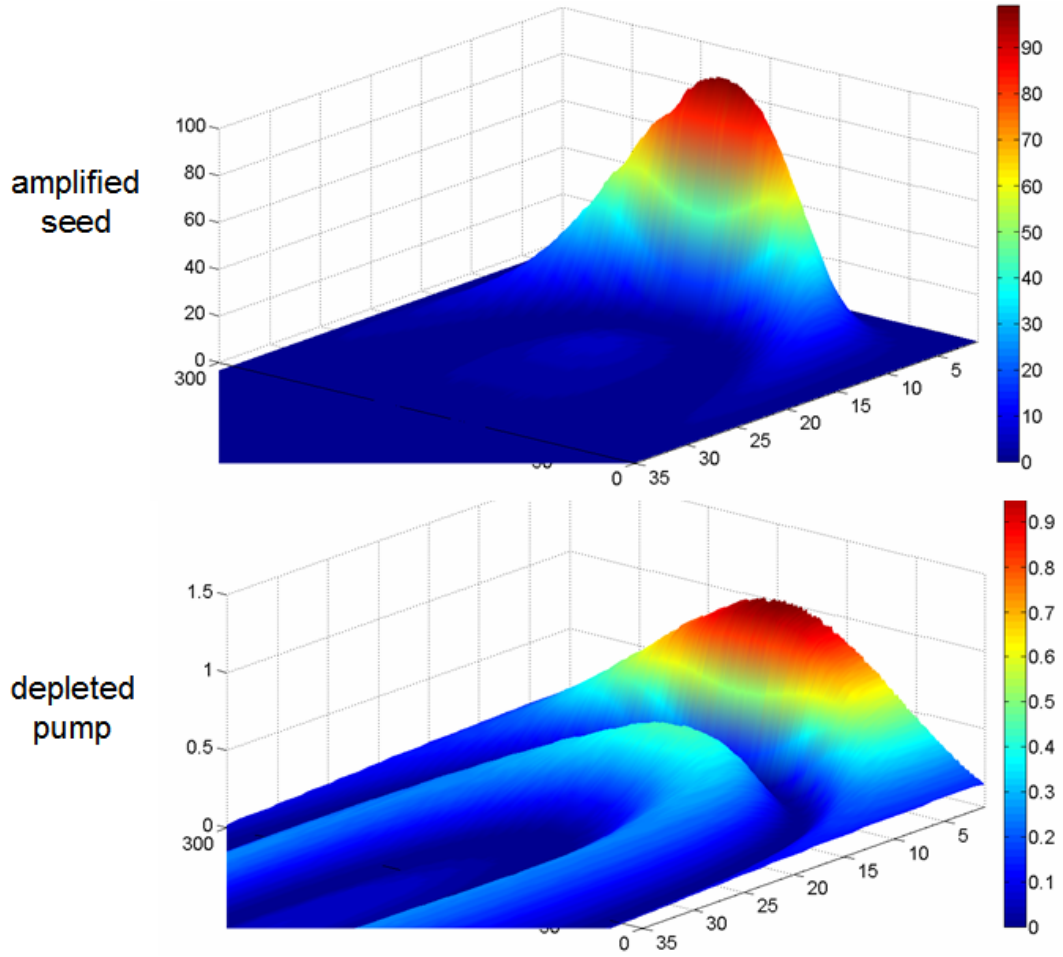


Figure 6.13: High  $k_2\lambda_D$  case final contour plots for Gaussian pump (bottom) and Gaussian seed (top). Intensities are normalized to the initial pump intensity of  $2.8 \times 10^{14} \text{ W/cm}^2$ . The pump moves to the left in the sense of coming out of the page and the seed moves to the right in the sense of going into the page.

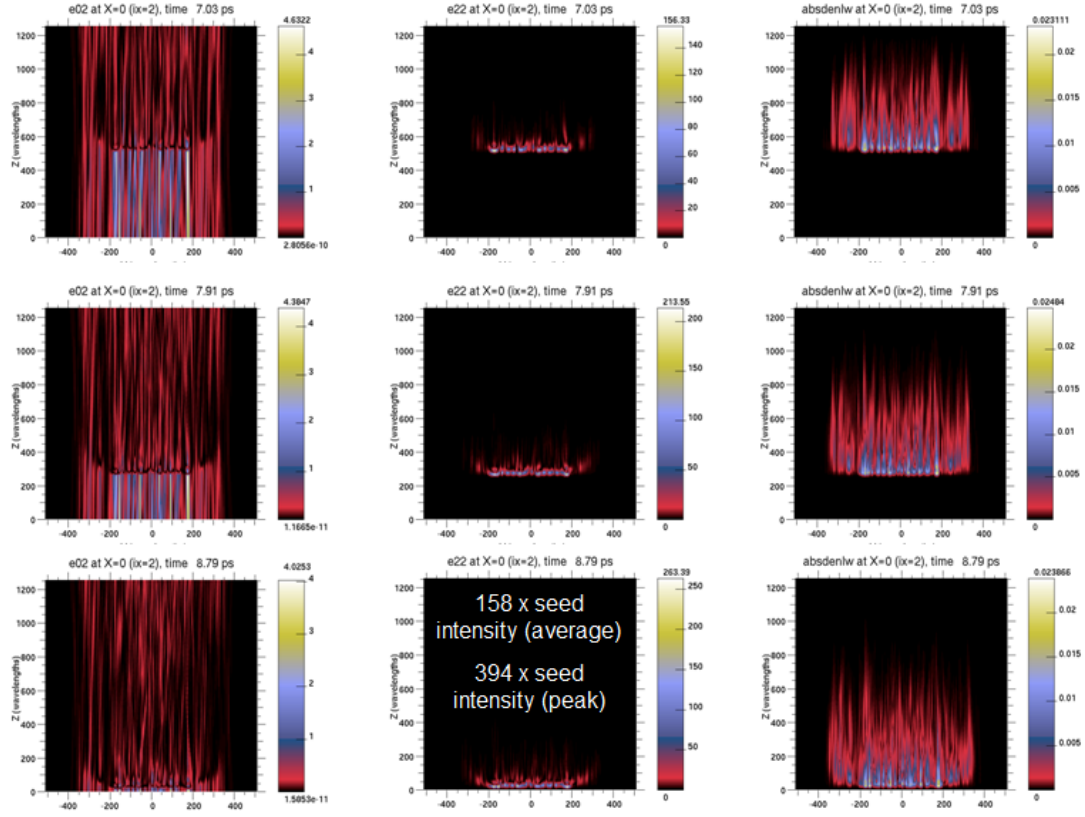


Figure 6.14: High  $k_2 \lambda_D$  case results for RPP pump (left column), Gaussian seed (center column), and driven plasma wave (right column). Intensities are normalized to the initial pump intensity of  $2.8 \times 10^{14} \text{ W/cm}^2$ . Plasma wave amplitudes are normalized to the critical density.

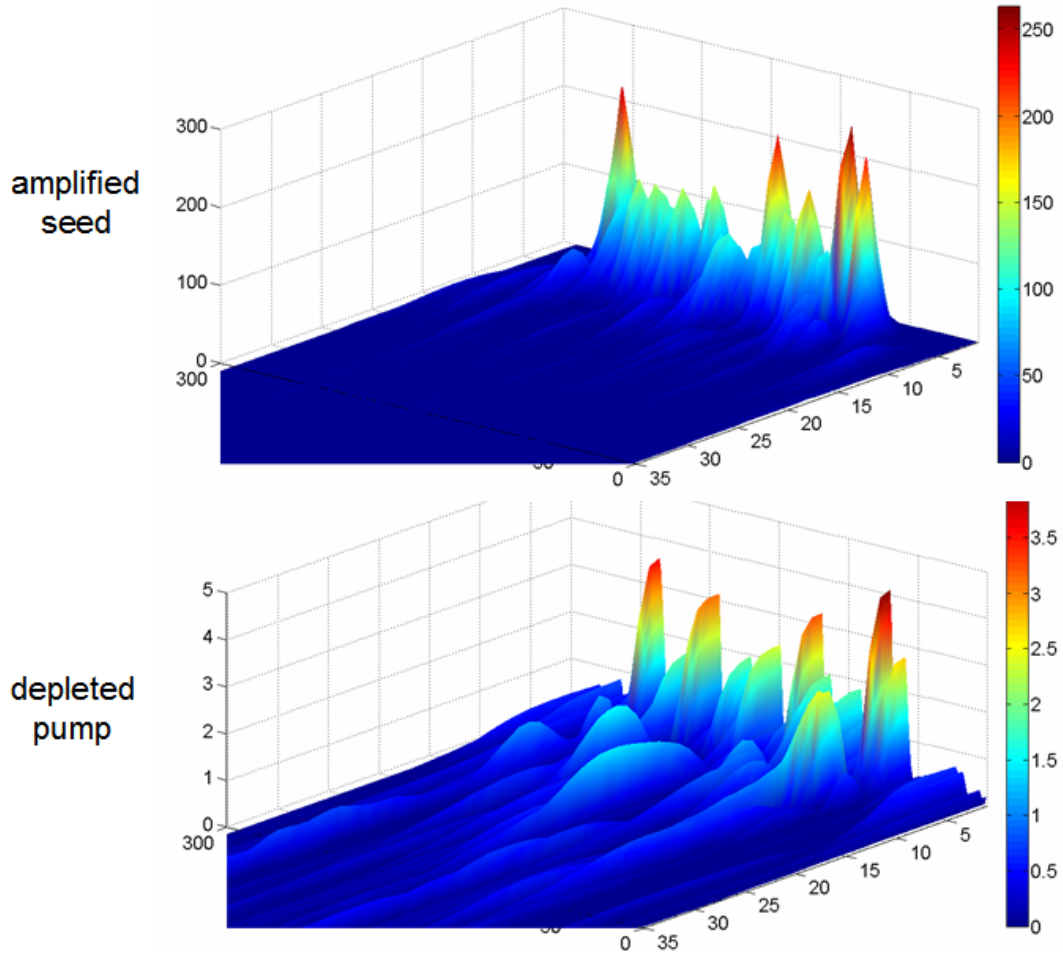


Figure 6.15: High  $k_2\lambda_D$  case final contour plots for RPP pump (bottom) and Gaussian seed (top). Intensities are normalized to the initial pump intensity of  $2.8 \times 10^{14} \text{ W/cm}^2$ . The pump moves to the left in the sense of coming out of the page and the seed moves to the right in the sense of going into the page.

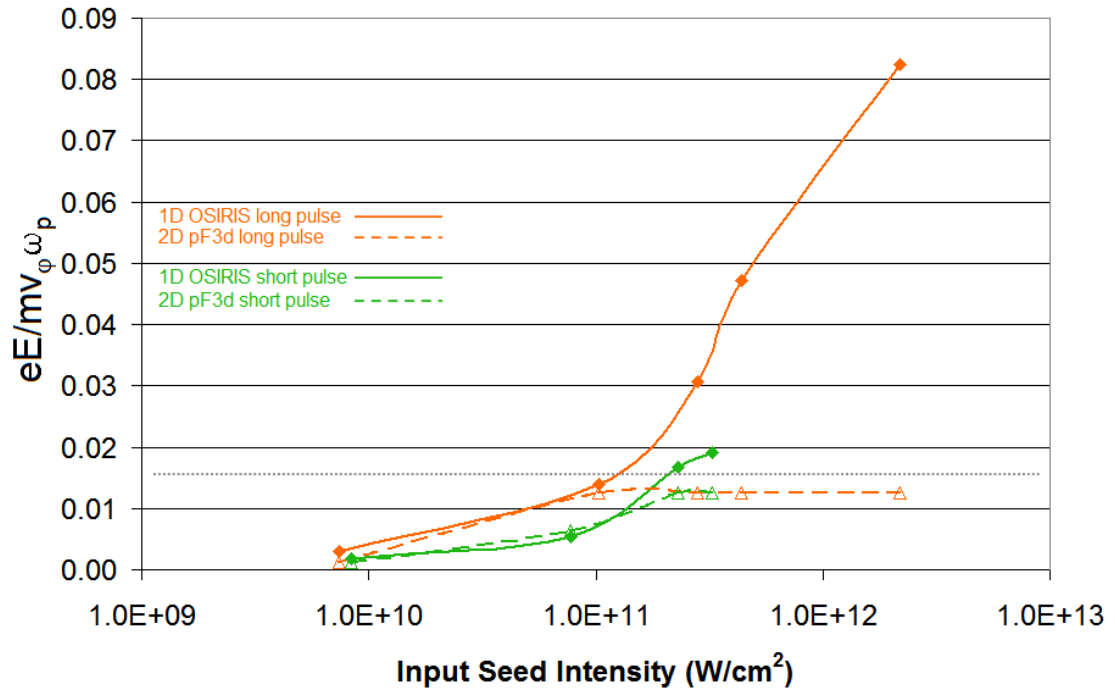


Figure 6.16: Plot of electrostatic field amplitude versus input peak intensity for 0.67 ps short pulse (green) and 3.7 ps long pulse (orange) cases in the 1D OSIRIS and 2D pF3d simulations. OSIRIS points are connected by solid lines and pF3d points are connected by dashed lines. The gray dotted line shows the trapping threshold.

# CHAPTER 7

## Summary and Ideas for Future Work

### 7.1 Summary

In this thesis we have conducted simulation and experimental studies of BRA for various plasma density and temperature conditions. We chose to focus on cases where the pump has a wavelength of  $1\ \mu\text{m}$  because of its availability and also because the results may be applicable to cross beam energy transfer in ICF targets. After discussing some of the previous work by other groups on this subject in Chapter 1 we reviewed the 1D theory of BRA and showed how it predicts a  $\pi$ -pulse structure for the amplified seed pulse in cold plasmas in Chapter 2. In Chapter 3 we conducted a 1D OSIRIS simulation study of BRA. After simulating the relatively cold case where seed evolution to a  $\pi$ -pulse was observed, we looked at three other cases by varying plasma density and temperature in order to see how kinetic effects can influence the shape of the seed pulse and affect its amplification. From doing these runs as part of a larger parameter scan, we identified a region in density versus temperature space that we believe is optimal for amplification. While in general higher densities and lower temperatures allow the seed to quickly enter the nonlinear pump depletion regime and form a  $\pi$ -pulse, our main finding was that the situation in which the best energy amplification occurs happens when the  $\pi$ -pulse does not form and the pump is not completely depleted over the given interaction length. In these cases most of the

energy could be contained within one peak of a somewhat longer seed that did not have a trail of decreasing amplitude spikes. We also saw that in a fixed length plasma the  $\pi$ -pulse seed was prone to earlier onset of the RFS instability causing it to break apart inside the plasma, but the single-peak seed could amplify all the way through and exit the plasma intact. Therefore while the leading peak of a  $\pi$ -pulse seed may be shorter and have higher powers, it does not contain as much energy as a seed which is longer but has all of its the energy contained in one single peak. In addition BRA of  $\pi$ -pulse seeds needs a cold plasma which may not be realistic because the process of creating preformed plasmas for BRA experiments via collisional ionization using a nanosecond laser beam will heat the plasma to moderately hot temperatures on the order of 100's of eV. Therefore, in going with the single-peak seed containing optimal energy, we identified plasma densities of around  $0.01 n_{cr}$  and temperatures between 200 eV to 300 eV as the plasma conditions giving the best energy amplification when using a  $1 \mu\text{m}$  pump laser.

In Chapter 4 we reported the results of our laboratory studies to create a seed pulse of wavelength around  $\sim 1.2 \mu\text{m}$  via Raman downshifting of  $1 \mu\text{m}$  wavelength photons in a gaseous medium. We used three candidate gases inside a custom-built Raman gas cell and studied how they each downshifted an incident  $1 \mu\text{m}$  laser pulse by taking energy and spectral measurements of the cell's output. We determined that  $N_2O$  was the best candidate to use because of its broad spectral coverage, which ensures that a portion of the seed will be in resonance for the BRA process in a plasma which may have density non-uniformities. Although we would have liked to obtain high conversion efficiency along with a narrowband signal centered at the exact downshifted wavelength, we understood that the 0.67 ps and 3.7 ps pulsewidths we were working with put us in the transient Raman regime where conversion is naturally lower and the resulting spectrum would be

broad. The spectral energy at the resonance wavelength of  $1.2 \mu\text{m}$  was on the order of  $100 \mu\text{J}$ . Therefore if it's even possible to make an intense seed pulse in the near-IR, another mechanism besides Raman downshifting in a gas would need to be used. In Chapter 5 we reported the results of the full BRA experiment in which we incorporated the laboratory setup from the seed creation experiment. By using attenuation we were able to get different seed energies to measure the amount of amplification for each one and to see if there is an overall trend. We discovered how challenging it was to get amplification since we took numerous shots and only ended up with a few that showed clear evidence that the seed amplified. There were some adverse experimental constraints that made it difficult to consistently get amplification such as timing jitter between the pump and the seed and an inhomogeneous plasma density profile due to non-uniformities in the gas flow from the gas jet nozzle. As a result we were unable to obtain multiple shots at each one of the seed energies to gauge the repeatability of the amplification and did not observe a clear-cut intensity scaling of the gain beyond what looks like a tendency for the gain to be less for higher initial seed intensities. Furthermore because our plasma conditions were in the strong damping regime, the seed in the experiment did not deplete the pump and we only obtained small amounts of amplification. To wrap up our studies we simulated the experimental parameters using 1D OSIRIS and 2D pF3d codes and compared the simulation results to the experimental data points in Chapter 6. What we found was that for both short and long pulses the 1D OSIRIS showed a trend in which the gain first increased and then decreased as the initial seed intensity was increased, while the 2D pF3d showed the gain to be almost constant. We were not surprised by this result since we understand that 1D OSIRIS is based on kinetic modeling of the plasma which could cause it to predict changes in the amplification from dynamics such as particle trapping and detuning via frequency shift while 2D

pF3d is based on the linear theory of LPI and won't show any changes in the amplification unless the pump is significantly depleted.

Because of the discrepancy between 1D OSIRIS and 2D pF3d in the simulation of the experiment, we felt it was necessary to perform another comparison with different parameters, showing a case (low  $k_2\lambda_D$ ) in which both codes agreed and another case (high  $k_2\lambda_D$ ) in which they disagreed. The low  $k_2\lambda_D$  case where fluid interactions are prominent showed excellent agreement in terms of predicted peak intensity of the amplified seed. The high  $k_2\lambda_D$  case where kinetic interactions are prominent showed disagreement in the predicted peak intensity. Again this was the result of the different models behind the two codes. Using an RPP in the simulations yielded some very high peak intensity speckles and this compromised the quality of the seed wavefront. This showed that continued simulation studies with RPP are needed to understand more about BRA in the context of transverse intensity profiles.

## 7.2 Ideas for Future Work

The prospect of amplifying a short seed pulse via resonant energy transfer from a long pump pulse remains something that is very intriguing to think about because the amplification process satisfies the same resonance conditions as SRS. But as we have learned first-hand from doing simulations and experiments, working toward the realization of a plasma-based Raman amplifier is a very tough challenge. Many physical effects such as SRS noise from the pump, detuning from resonance, FRS of the amplified seed, self-focusing and filamentation of the pump and seed, and kinetic effects leading to possible saturation of amplification can all adversely impact the seed and place limits on the amount of peak inten-

sity that can be achieved. Therefore the success of BRA will have to depend on new ideas and approaches to be implemented in the future which can mitigate or bypass some of the current physical restrictions. Here we list some ideas and thoughts that could be considered for future work on this problem.

1. Uniformity and reproducibility of plasma density profiles is of utmost importance when doing BRA experiments using supersonic gas jet nozzles. Special nozzle designs that improve the flow of gas [88] and ultrafast-opening valves that reduce the possibility of static build-up in the valve [89] may be the answer to achieving more uniform plasmas.
2. In Figure 7.1 we draw a cartoon showing counter-propagating and shallow angle configurations for a typical BRA experimental setup. When discussing BRA experiments it is usually assumed that the pump and the seed will directly counter-propagate to each other to maximize their interaction. However there are some difficulties with setting up an experiment in this manner as residual amounts of undepleted pump can propagate back along the optical path of the seed and damage the transport optics. It is also harder to set up diagnostics to measure the amplified seed when the pump is in the way. From our experience in the work for this thesis, we recommend using the shallow angle configuration to reduce the risk of damage and make the setup more convenient if one can accept some non-uniformity in the amplification due to the slightly oblique crossing angle.
3. If a phase plate is used on the pump and the seed crosses through it at a slight angle, the interaction will allow the seed to average over effectively more speckle transverse area and thus amplify and acquire a smoother intensity profile at the output.

4. Using a pump pulse with a prescribed chirp may help to decohere any premature Raman backscatter from the pump laser [90]. Having a chirped pump may enable the resonance condition to be maintained by dynamically neutralizing the effect of detuning.
5. Chirping the seed pulse may also be possible to suppress the tendency of the amplified seed to undergo Raman forward scatter [91]. A combination of a chirped seed with a mild plasma density gradient may work even better with the tradeoff being sacrificing some of the amplification.
6. The BRA concept may be scaled to other pump wavelengths besides 1

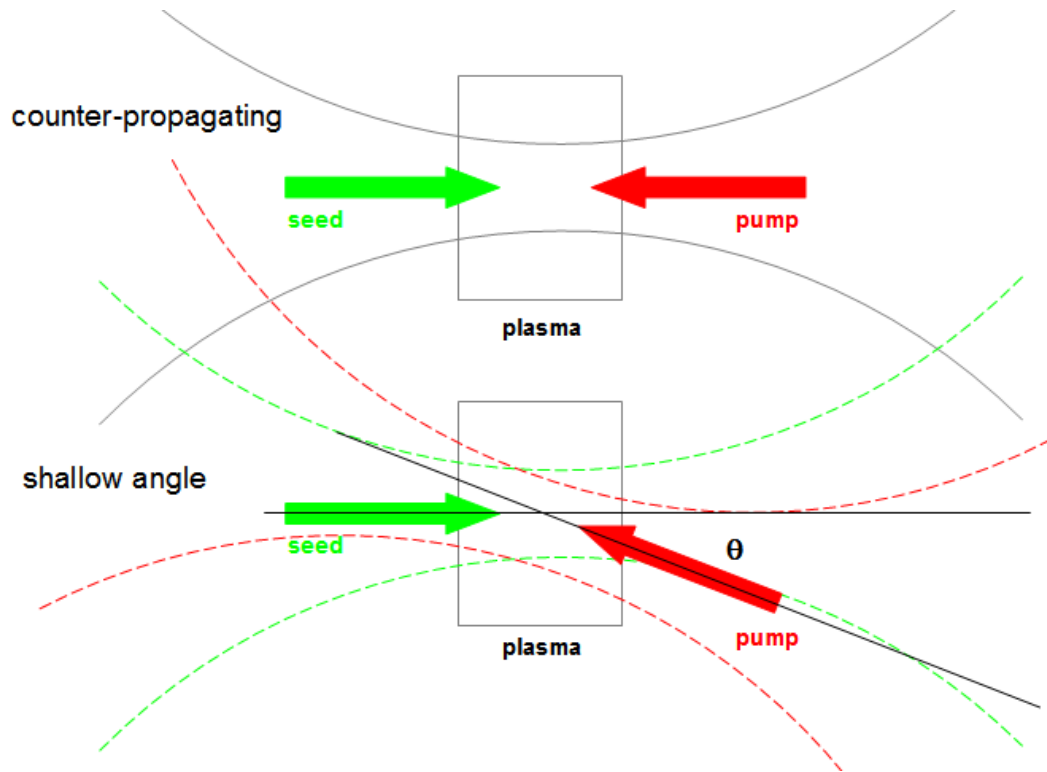


Figure 7.1: Cartoon showing counter-propagating and shallow angle configurations for pump and seed interaction.

$\mu\text{m}$  or  $0.8 \mu\text{m}$ . Examples of this would be to scale the problem to laser wavelengths relevant to NIF [92] or even to x-ray laser wavelengths [93].

7. The role of kinetic effects in multi-dimensional scenarios has been addressed in recent studies of SRS. In particular the phenomena of wavefront bowing of a plasma wave in relation to its phase velocity and self-focusing of plasma waves due to trapped particles have been explained in PIC simulations [94] as well as the growth and convection of finite width plasma wave packets [95]. These dynamics of the plasma wave need to be understood because they can potentially modify the transverse profile of the seed beam.

From this list we note that the implementation of possible improvements to BRA based on any of these ideas could be very complex from a technological standpoint involving lasers and optics, making BRA an exciting ongoing area of research for many years to come.

# APPENDIX A

## Extended Three Wave Model

As mentioned in earlier in this thesis, the nature of PIC simulations makes them computationally intensive, sometimes requiring the use of millions of cells and tens of millions of particles in order to adequately resolve the laser wavelength and the plasma wave frequency. Thus when simulating the BRA problem, where the frequency of the driven plasma wave can be up to twice the frequency of the individual laser beams, the demands on resolution in the simulation box can become quite large especially when one considers multiple dimensions. Therefore it is of practical interest to investigate whether an alternative model, which can run much faster but still incorporate the underlying kinetic effects present to a certain degree of accuracy, can be developed and used to study the BRA problem.

In this appendix we present results from a study that compared 1D simulations of BRA from the conventional PIC code OSIRIS and an extended three wave (ETW) model that was created to model plasma kinetic effects [96]. We present the results of several 1D BRA case studies in which plasmas of fixed density but different temperatures are simulated using OSIRIS, the ETW code, and a more conventional “Landau” three wave (LTW) model which includes the familiar Bohm-Gross detuning of the plasma frequency. The results that we show below have been published in a recent paper [97], but before discussing them we first briefly summarize the underlying idea behind the ETW model.

As we mentioned in Chapter 2, when plasma electrons are trapped in the elec-

trostatic potential of the plasma waves, the waves themselves will begin to lose their coherence. This is because the coherent energy of those plasma waves end up transforming into the incoherent kinetic energy of the phase mixed electrons. Ordinary three wave fluid models do not take into account this nonlinear kinetic process and thus cannot properly model BRA in the kinetic regime. Therefore a reduced kinetic theory was developed with the purpose of modeling these effects more accurately [98]. This theory was subsequently implemented into the ETW model which advects the laser and plasma wave envelopes self-consistently like in ordinary three wave models, but incorporates any possible kinetic behavior of the plasma. The key concept behind this reduced theory is finding a way to model the dynamical transition between the linear Landau damping limit and the BGK-type distribution limit based on energy considerations. The method that was created involved taking the amount of energy that is damped from the plasma wave in the linear damping regime and using it to calculate a local nonlinear amplitude-dependent frequency shift  $\delta\omega$  that is undergone by the plasma wave as it evolves into a BGK mode in the time-asymptotic or late time limit. An interpolating function that involves the ratio of the Landau damped energy to the incoherent kinetic energy is derived from the principles of conservation of action and canonical momentum and is used to smoothly transition the plasma wave from from one limit to the other. Thus the modification to the electron distribution function leading to a nonlinear frequency shift in thermal plasmas is modeled in this manner. Since the plasma frequency of a thermal plasma is modified from the cold plasma frequency, the ETW model makes use of the parameter  $\omega_L$ , which is the natural frequency of the plasma that appears in the Vlasov dispersion relation. In the ETW model,  $\omega_L$  is specified as a coefficient multiplied by the cold plasma frequency  $\omega_p$ , and this becomes the resonant frequency of the thermal plasma.

In the setup for the comparison of the different models we specify a 1 mm

uniform plasma with a density of  $3.6 \times 10^{19} \text{ cm}^{-3}$ , buffered by vacuum regions on both sides. As shown in Figure A.1, which is our cold plasma test case, the 1054 nm pump laser envelope travels from right to left while the 1300 nm seed laser envelope propagates from left to right. The 1300 nm vacuum wavelength for the seed carrier is chosen so that the difference between the corresponding pump and seed frequencies is the cold linear plasma frequency. The vacuum regions are wide enough to contain the entire pump and seed after they leave the plasma slab, allowing diagnostic observation of the laser pulses in vacuum outside of the plasma. The pump is specified as having  $a_0 = 0.015$  with a 100 fs rise followed by a 6.66 ps flat top. The seed is specified as an approximate Gaussian having  $a_1 = 0.015$  with a pulse width of 100 fs. For the PIC simulations, the box size is  $30250.45 c/\omega_0$  and contains 290000 uniform cells with 128 macroparticles per cell. Length units are normalized to  $c/\omega_0$  ( $0.17 \mu\text{m}$ ) and time units are normalized to  $1/\omega_0$  (0.56 fs) for the 1054 nm pump laser. The time step used is 0.058 fs and the total simulation time is 13.6 ps. The cell size is  $0.1043 c/\omega_0$ , corresponding to 60 cells per pump laser wavelength. The ions are taken as fixed, so only the electron sheets are allowed to move. Upon looking at the test case presented in Figure A.1, we observe reasonably close overlap between ETW and PIC predictions for the seed and pump envelopes at the beginning and at the end of the simulation. This gives us confidence that the ETW model works as well as the PIC model for the case of a cold plasma.

Having verified reasonable agreement between the ETW and PIC algorithms for a cold plasma, we next examined their predictions for thermal plasmas. This time we also included the LTW model as a reference. We compared results for a sequence of initial plasma temperatures corresponding to 78 eV, 142 eV, 200 eV, 365 eV, and 525 eV, all with the same initial pump and seed lasers. Because of thermal effects, the resonant plasma frequency  $\omega_L$  is modified from the cold

Table A.1: Parameters used for simulations comparing the ETW, PIC, and LTW models

Temperature	$k_2\lambda_D$	$\omega_L/\omega_p$
0 eV	0	1
78 eV	0.115	1.02
142 eV	0.156	1.038
200 eV	0.185	1.055
365 eV	0.25	1.106
525 eV	0.3	1.158

plasma frequency  $\omega_p$ , and thus for higher temperatures the resonance between the lasers and the plasma becomes increasingly detuned. As mentioned previously, the ETW code makes use of an interpolating function and a  $\omega_L$  value obtained from the ETW model for each different temperature at the chosen plasma density. Table A.1 provides these basic parameters for each of the temperature cases. The LTW model that we included for reference uses the real (detuning) and imaginary (damping) frequency shifts of the plasma wave as predicted from linear theory, but contains none of the nonlinear kinetic physics.

The results of the comparison between the ETW, PIC, and LTW codes for the seed pulse in each of the thermal plasma simulations are shown in Figure A.2, which zooms in on a local section of the simulation box containing the first few peaks of the seed envelopes. The fine-scale spikiness in the PIC seed is due primarily to numerical errors in the simple algorithm employed to approximate the envelope from the full transverse electric fields, while the remnant traces of the counter-propagating (magenta) fields are a numerical artifact of the directional diagnostic used to extract the left and right-moving electromagnetic fields. The cold plasma test simulation result is included for completeness. Since the

amplitudes in both three wave simulations are normalized to the initial pump amplitude, the PIC result had to be scaled in the same manner in order to overlap it meaningfully on the three wave results. Note that because the three wave models advect the laser fields precisely at speed  $c$  while the PIC propagates the laser fields at something closer to  $v_{g0,1} = c[1 - \omega_p^2/\omega_{0,1}^2]^{1/2}$  while inside the plasma, a slight overall phase shift of the PIC waveforms had to be introduced in order to compensate for the differing group velocities and observe the best-case overlap. After doing this, we observed reasonably good agreement between ETW and PIC results for all cases (a)-(f), with the agreement generally improving for the lower temperatures. Furthermore, at a sufficiently low temperature, the final seed in the ETW model does resemble to some extent the characteristic self-similar  $\pi$ -pulse structure described in the nonlinear theory of BRA. We find the agreement between PIC and ETW to be the best in the leading spike of the seeds, where the peak amplitudes and pulsewidths match quite closely, and the agreement even holds moderately well at higher temperatures. We also find that the ETW and LTW results coincide at zero temperature, but their agreement becomes poor as the temperature is increased. At the lower temperatures, the leading spikes have temporal widths of  $O(50 \text{ fs})$  at half-maximum and  $O(100 \text{ fs})$  near the base, while the bounce period is estimated as  $O(25 \text{ fs})$ . Therefore, even at the lower (but non-zero) temperatures, a given plasma particle may execute a significant fraction of one bounce oscillation or more while under the leading spike of the seed envelope, so we should not be surprised that the predictions of the ETW and LTW models begin to differ. Although both ETW and LTW models tend to misrepresent the width of the leading spike at higher temperatures in comparison to PIC, the LTW model consistently underestimates the width and overestimates the height of the leading spike in comparison to the ETW model. This discrepancy gets more significant at the higher temperatures. Compared to PIC, both

ETW and LTW models predict too many discernible secondary spikes in the amplified seed envelope. At lower temperatures, they predict the trailing portion of the seed more accurately, but at higher temperatures the ETW model does better in the sense of predicting fewer discernible secondary spikes and tracking more closely the general decay of the amplitudes.

Because agreement between PIC and ETW is reasonably close in the leading spike of the seeds, in terms of both peak amplitudes and pulse widths over the covered temperature range, we expect that their predictions for the peak intensity and total energy in the leading spike should also compare favorably within the same order-of-magnitude. To quantify this further, Figure A.3 shows a plot of normalized peak seed intensity versus time and compares the ETW to the LTW and PIC results. The ETW models underestimate the peak intensity achieved at all but the highest temperature considered, but at moderate temperatures (up to 200 eV) the predicted peak seed intensities in ETW and PIC differ by no more than 10%, and even at the higher temperatures, they agree to within 20%. In contrast, the LTW model always overestimates the peak power, with this error becoming increasingly pronounced at higher temperatures. At the highest temperature, the LTW result overestimates the PIC result by about 300%. In all, agreement between ETW and PIC is generally superior to that between LTW and PIC. Efforts are underway to pinpoint the exact cause of the increasing discrepancy between ETW and PIC for higher temperature regimes and to resolve residual disagreement over the peak intensities. Furthermore, as visual inspection of the seed envelopes in Figure A.2 revealed, rather different waveform features emerge in the secondary pulselets behind the leading spike, and thus further simulations must be done to determine the cause of these differences in trailing edge behavior.

The ETW model used in this study of BRA is an improvement over ordinary

three wave models like the LTW model in that it incorporates important non-linear aspects of kinetic effects. Although the ETW model takes certain kinetic effects into account, it does not comprehensively include all the kinetic physics, most notably full wave-breaking of the plasma wave and nonlinear saturation of the seed growth in BRA. Nonetheless its modeling capability agrees with PIC simulations to a certain semi-quantitative extent, and it enjoys the extra benefit of computational simplicity and speed. The time required to simulate typical cases with the ETW code was vastly shorter, by over two to three orders of magnitude, than that required for the corresponding simulations using the PIC code. One case study that took less than one minute on a dual-core Intel PC running the ETW code required approximately 13 hours on 32 processors of a parallel supercomputing cluster running the 1D PIC code. Because of this quick turnaround time the ETW code can conceivably be used to complement a PIC code by first running numerous exploratory scans of the parameter space and identifying a few favorable parameter sets, which can then be simulated with a PIC code in more detail. As for its stand-alone practical usefulness, further development of the ETW model as well as other reduced models [99, 100, 101] will have to be done in order to create a more realistic simulation model. A final point to mention is that 1D models should not be used with the expectation of obtaining very precise quantitative predictions for real experiments. Transverse physics such as diffraction and filamentation are among the effects that need to be considered for better prediction of experimental scenarios. Therefore another area for future development is higher-dimensional reduced model codes, and the current ETW model is a good starting point on the path to realizing that objective.

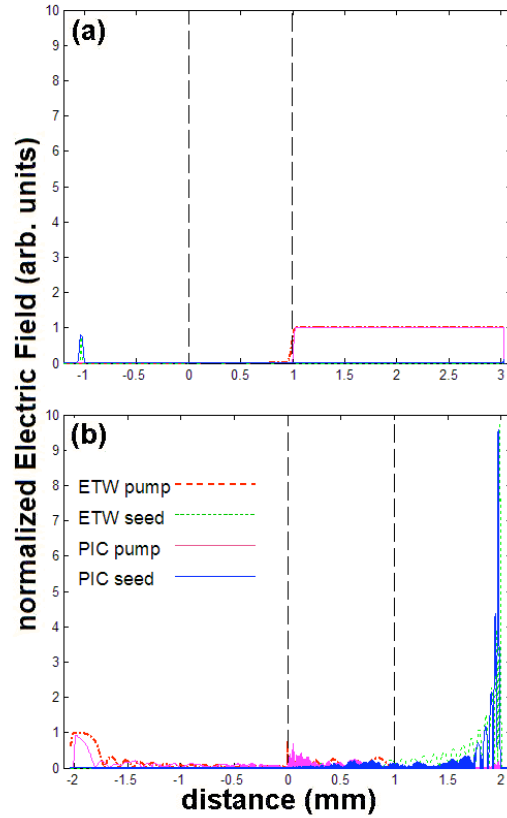


Figure A.1: Snapshots of the 1054 nm pump laser envelope (dash-dotted red line for ETW, solid magenta line for PIC) and the 1300 nm seed laser envelope (dashed green line for ETW, blue line for PIC) interacting in a cold plasma at (a) near the beginning of the simulation, with the seed still outside the plasma and the pump just entering the plasma and (b) near the end of the simulation, after the bulk of the seed and pump envelopes have exited the plasma. The vertical dashed lines indicate the boundaries of the 1 mm plasma slab. Reprinted with permission from T.-L. Wang, D. Michta, R. R. Lindberg, A. E. Charman, S. F. Martins, and J. S. Wurtele, *Phys. Plasmas* **16**, 123110 (2009). Copyright 2009, American Institute of Physics.

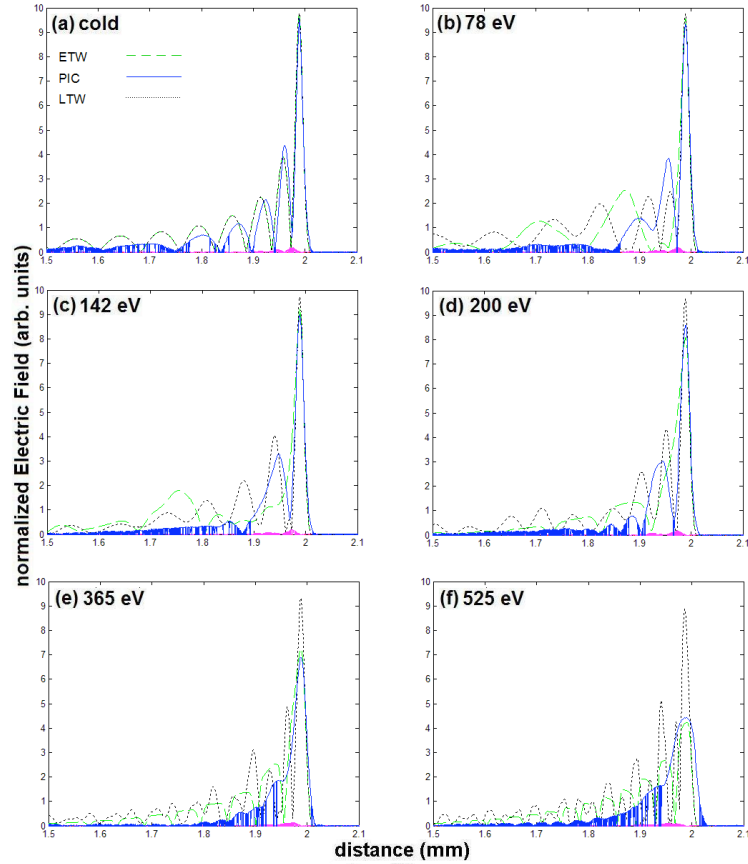


Figure A.2: Profiles of the final seed laser envelopes (green line for ETW, blue line for PIC, dashed line for LTW) after exiting the plasma for (a) cold, (b) 78 eV, (c) 142 eV, (d) 200 eV, (d) 365 eV, (e) 525 eV cases. Due to the difference in group velocities, the PIC waveforms have been shifted to best overlap with the ETW and LTW envelopes. Reprinted with permission from T.-L. Wang, D. Michta, R. R. Lindberg, A. E. Charman, S. F. Martins, and J. S. Wurtele, *Phys. Plasmas* **16**, 123110 (2009). Copyright 2009, American Institute of Physics.

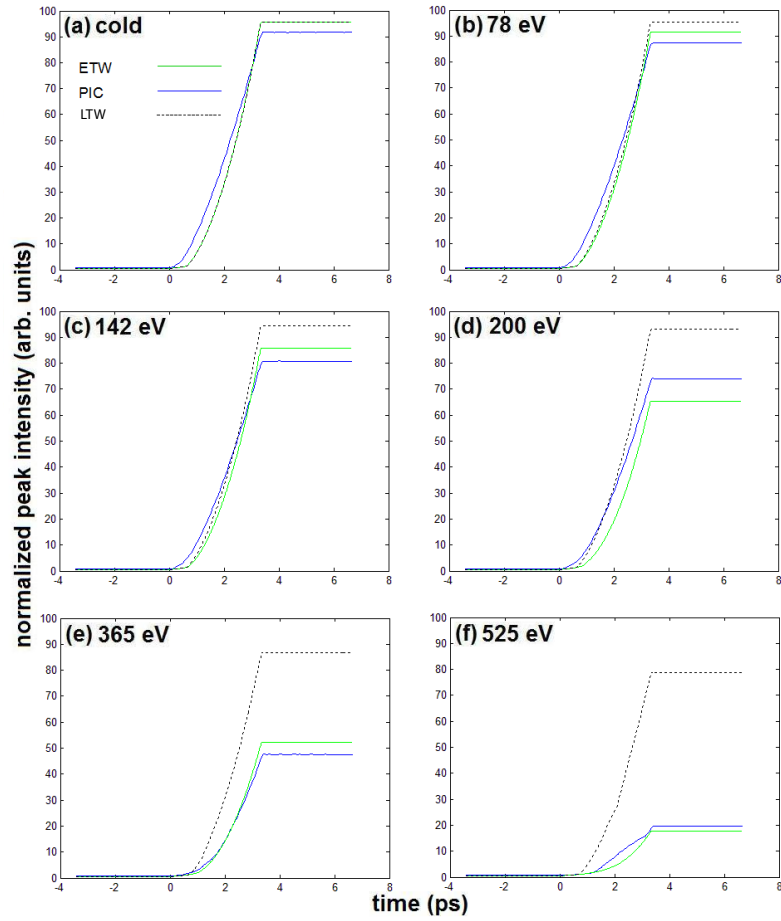


Figure A.3: Time-series of normalized peak intensity versus time for (a) cold, (b) 78 eV, (c) 142 eV, (d) 200 eV, (d) 365 eV, and (e) 525 eV cases, showing predictions of the ETW (green line), PIC (blue line), and LTW (dotted line) models. At time  $t = 0$  ps the peak of the seed and the peak of the pump meet close to the the leading (left) edge of the plasma slab. Reprinted with permission from T.-L. Wang, D. Michta, R. R. Lindberg, A. E. Charman, S. F. Martins, and J. S. Wurtele, *Phys. Plasmas* **16**, 123110 (2009). Copyright 2009, American Institute of Physics.

## REFERENCES

- [1] W. L. Kruer, *The Physics of Laser Plasma Interactions*, Addison-Wesley Publishing Co., New York, 1988.
- [2] D. Strickland and G. Mourou, “Compression of amplified chirped optical pulses”, *Optics Communications* **56**, 219 (1985).
- [3] N. J. Fisch and V. M. Malkin, “Generation of ultrahigh intensity laser pulses”, *Phys. Plasmas* **10**, 2056 (2003).
- [4] V. M. Malkin, G. Shvets, and N. J. Fisch, “Fast Compression of Laser Beams to Highly Overcritical Powers”, *Phys. Rev. Lett.* **82**, 4448 (1999).
- [5] V. M. Malkin, G. Shvets, and N. J. Fisch, “Ultra-powerful compact amplifiers for short laser pulses”, *Phys. Plasmas* **7**, 2232 (2000).
- [6] C. E. Capjack, C. R. James, and J. N. McMullin, “Plasma KrF laser pulse compressor”, *J. Appl. Phys.* **53**, 4046 (1982).
- [7] J. R. Murray, J. Goldhar, D. Eimerl, and A. Szoke, “Raman Pulse Compression of Excimer Lasers for Application to Laser Fusion”, *IEEE Journ. Quantum Electronics* **QE-15**, 342 (1979).
- [8] Y. Ping, W. Cheng, S. Suckewer, D. S. Clark, and N. J. Fisch, “Amplification of Ultrashort Laser Pulses by a Resonant Raman Scheme in a Gas-Jet Plasma”, *Phys. Rev. Lett.* **92**, 175007 (2004).
- [9] W. Cheng, Y. Avitzour, Y. Ping, S. Suckewer, N. J. Fisch, M. S. Hur, and J. S. Wurtele, “Reaching the Nonlinear Regime of Raman Amplification of Ultrashort Laser Pulses”, *Phys. Rev. Lett.* **94**, 045003 (2005).
- [10] J. Ren, S. Li, A. Morozov, S. Suckewer, N. A. Yampolsky, V. M. Malkin, and N. J. Fisch, “A compact double-pass Raman backscattering amplifier/compressor”, *Phys. Plasmas* **15**, 056702 (2008).
- [11] C.-H. Pai, M.-W. Lin, L.-C. Ha, S.-T. Huang, Y.-C. Tsou, H.-H. Chu, J.-Y. Lin, J. Wang, and S.-Y. Chen, “Backward Raman Amplification in a Plasma Waveguide”, *Phys. Rev. Lett.* **101**, 065005 (2008).
- [12] T. Tajima and G. Mourou, “Zettawatt-exawatt lasers and their applications in ultrastrong-field physics”, *Phys. Rev. STAB* **5**, 031301 (2002).
- [13] S. V. Bulanov, T. Esirkepov, and T. Tajima, “Light Intensification towards the Schwinger Limit”, *Phys. Rev. Lett.* **91**, 085001 (2003).

- [14] M. Tabak, J. Hammer, M. E. Glinsky, W. L. Kruer, S C. Wilks, J. Woodworth, E. M. Campbell, and M. D. Perry, “Ignition and high gain with ultrapowerful lasers”, *Phys. Plasmas* **1**, 1626 (1994).
- [15] D. S. Clark and N. J. Fisch, “Raman laser amplification in preformed and ionizing plasmas”, *Laser and Particle Beams* **23**, 101 (2005).
- [16] D. S. Clark and N. J. Fisch, “Particle-in-cell simulations of Raman laser amplification in preformed plasmas”, *Phys. Plasmas* **10**, 4848 (2003).
- [17] P. J. Mardahl, H. J. Lee, G. Penn, J. S. Wurtele, and N. J. Fisch, “Intense laser pulse amplification using Raman backscatter in plasma channels”, *Phys. Lett. A* **296**, 109, (2002).
- [18] R. M. G. M. Trines, F. Fiuza, R. Bingham, R. A. Fonseca, L. O. Silva, R. A. Cairns, and P. A. Norreys, “Efficient Raman amplification into the Petawatt regime”, e-print arXiv:0811.1736v1.
- [19] Y.-F. Xiao, H.-H. Chu, H.-E. Tsai, C.-H. Lee, J.-Y. Lin, J. Wang, and S.-Y. Chen, “Efficient generation of extended plasma waveguides with the axicon ignitor-heater scheme”, *Phys. Plasmas* **11**, L21 (2004).
- [20] R. K. Kirkwood, E. Dewald, C. Niemann, N. Meezan, S. C. Wilks, D. W. Price, O. L. Landen, J. Wurtele, A. E. Charman, R. Lindberg, N. J. Fisch, V. M. Malkin, and E. O. Valeo, “Amplification of an ultrashort pulse laser by stimulated Raman scattering of a 1 ns pulse in a low density plasma”, *Phys. Plasmas* **14**, 113109 (2007).
- [21] A. Bers, “Space-time evolution of plasma instabilities - absolute and convective”, *Handbook of Plasma Physics*, Volume 1, p. 451, North-Holland, New York (1983).
- [22] B. I. Cohen, H. A. Baldis, R. L. Berger, K. G. Estabrook, E. A. Williams, and C. Labaune, “Modeling of the competition of stimulated Raman and Brillouin scatter in multiple beam experiments”, *Phys. Plasmas* **8**, 571 (2001).
- [23] J. L. Kline, D. S. Montgomery, L. Yin, D. F. DuBois, B. J. Albright, B. Bezzerides, J. A. Cobble, E. S. Dodd, J. C. Fernandez, R. P. Johnson, J. M. Kindel, H. A. Rose, H. X. Vu, and W. Daughton, “Different  $k\lambda_D$  regimes for nonlinear effects on Langmuir waves”, *Phys. Plasmas* **13**, 055906 (2006).
- [24] B. L. Bobroff and H. A. Haus, “Impulse response of active coupled wave systems”, *J. Appl. Phys.* **38**, 390 (1967).

- [25] G. L. Lamb, “Propagation of Ultrashort Optical Pulses”, Phys. Lett. A **25A**, 181 (1967).
- [26] G. L. Lamb, “ $\pi$  pulse Propagation in a Lossless Amplifier”, Phys. Lett. A **29A**, 507 (1969).
- [27] G. L. Lamb, “Analytical Descriptions of Ultrashort Optical Pulse Propagation in a Resonant Medium”, Rev. Mod. Phys. **43**, 99 (1971).
- [28] L. D. Landau, “On The Vibrations Of The Electronic Plasma”, J. Phys. USSR **10**, 25 (1946).
- [29] T. P. Coffey, “Breaking of large amplitude plasma oscillations”, Phys. Fluids **14**, 1402 (1971).
- [30] T. M. O’Neil, “Collisionless Damping of Nonlinear Plasma Oscillations”, Phys. Fluids **8**, 2255 (1965).
- [31] G. J. Morales and T. M. O’Neil, “Nonlinear Frequency Shift of an Electron Plasma Wave”, Phys. Rev. Lett. **28**, 417 (1972).
- [32] I. B. Bernstein, J. M. Greene, and M. D. Kruskal, “Exact Nonlinear Plasma Oscillations”, Phys. Rev. **108**, 546 (1957).
- [33] H. X. Vu, D. F. DuBois, and B. Bezzerides, “Inflation threshold: A nonlinear trapping-induced threshold for the rapid onset of stimulated Raman scattering from a single laser speckle”, Phys. Plasmas **14**, 012702 (2007).
- [34] W. B. Mori, *Private Communication*, 2010.
- [35] B. J. Winjum, J. E. Fahlen, F. S. Tsung, and W. B. Mori, “Effects of plasma wave packets and local pump depletion in stimulated Raman scattering”, Phys. Rev. E **81**, 045401(R) (2010).
- [36] G. J. Pert, “Inverse bremsstrahlung in strong radiation fields at low temperatures”, Phys. Rev. E **51**, 4778 (1995).
- [37] P. K. Kaw, G. Schmidt, and T. Wilcox, “Filamentation and trapping of electromagnetic radiation in plasmas”, Phys. Fluids **16**, 1522 (1973).
- [38] G.-Z. Sun, E. Ott, Y. C. Lee, and P. Guzdar, “Self-focusing of short intense pulses in plasmas”, Phys. Fluids **30**, 526 (1987).
- [39] P. Sprangle, C.-M. Tang, and E. Esarey “Relativistic self-focusing of short-pulse radiation beams in plasmas”, IEEE Trans. Plasma Sci. **PS-15**, 145 (1987).

- [40] A. G. Litvak, “Finite-amplitude Wave Beams in a Magnetoactive Plasma”, *Sov. Phys. JETP* **30**, 344 (1970).
- [41] C. E. Max, J. Arons, and A. B. Langdon, “Self-Modulation and Self-Focusing of Electromagnetic Waves in Plasmas”, *Phys. Rev. Lett.* **33**, 209 (1974).
- [42] T. M. Antonsen and P. Mora, “Self-Focusing and Raman Scattering of Laser Pulses in Tenuous Plasmas”, *Phys. Rev. Lett.* **69**, 2204 (1992).
- [43] G. M. Fraiman, N. A. Yampolsky, V. M. Malkin, and N. J. Fisch, “Robustness of laser phase fronts in backward Raman amplifiers”, *Phys. Plasmas* **9**, 3617 (2002).
- [44] A. A. Solodov, V. M. Malkin, and N. J. Fisch, “Random density inhomogeneities and focusability of the output pulses for plasma-based powerful backward Raman amplifiers”, *Phys. Plasmas* **10**, 2540 (2003).
- [45] J. Nuckolls, L. Wood, A. Thiessen, and G. Zimmerman, “Laser Compression of Matter to Super-High Densities: Thermonuclear (CTR) Applications”, *Nature* **239**, 139 (1972).
- [46] G. H. Miller, E. I. Moses, and C. R. Wuest, “The National Ignition Facility”, *Opt. Eng.* **43**, 2841 (2004).
- [47] J. D. Lindl, *Inertial Confinement Fusion: The Quest for Ignition and Energy Gain Using Indirect Drive*, Springer-Verlag, New York, 1998.
- [48] R. K. Kirkwood, D. S. Montgomery, B. B. Afeyan, J. D. Moody, B. J. MacGowan, C. Joshi, K. B. Wharton, S. H. Glenzer, E. A. Williams, P. E. Young, W. L. Kruer, K. G. Estabrook, and R. L. Berger, “Observation of the Nonlinear Saturation of Langmuir Waves Driven by Ponderomotive Force in a Large Scale Plasma”, *Phys. Rev. Lett.* **83**, 2965 (1999).
- [49] C. K. Birdsall and A. B. Langdon, *Plasma Physics via Computer Simulation*, Adam Hilger, New York (1991).
- [50] T.-L. Wang, D. S. Clark, D. J. Strozzi, S. C. Wilks, S. F. Martins, and R. K. Kirkwood, “Particle-in-cell simulations of kinetic effects in plasma-based backward Raman amplification in underdense plasmas”, *Phys. Plasmas* **17**, 023109 (2010).
- [51] Yu. A. Tsidulko, V. M. Malkin, and N. J. Fisch, “Suppression of Superluminescent Precursors in High-Power Backward Raman Amplifiers”, *Phys. Rev. Lett.* **88**, 235004 (2002).

- [52] R. A. Fonseca, L. O. Silva, F. S. Tsung, V. K. Decyk, W. Lu, C. Ren, W. B. Mori, S. Deng, S. Lee, T. Katsouleas, and J. C Adam, “OSIRIS: A three-dimensional, fully relativistic particle in cell code for modeling plasma based accelerators”, *Lecture Notes In Computer Science*, ICCS 2002, **2331**, p. 342, Springer, Berlin (2002).
- [53] W. B. Mori, C. D. Decker, D. E. Hinkel, and T. Katsouleas, “Raman Forward Scattering of Short-Pulse High-Intensity Lasers”, *Phys. Rev. Lett.* **72**, 1482 (1994).
- [54] W. Mueckenheim, *Manual For Raman Cells*, Report No. NASA TM-77756, National Aeronautics and Space Administration, Washington D.C. (1984).
- [55] D. G. Fouche and R. K. Chang, “Relative Raman Cross Section for  $O_3$ ,  $CH_4$ ,  $C_3H_8$ , NO,  $N_2O$ , and  $H_2$ ”, *Appl. Phys. Lett.* **20**, 256 (1972).
- [56] W. R. Fenner, H. A. Hyatt, J. M. Kellam, S. P. S. Porto, “Raman cross section of some simple gases”, *J. Opt. Soc. Am.* **63**, 73 (1973).
- [57] J. Dunn, J. Nilsen, A. L. Osterheld, Y. Li, and V. N. Shlyaptsev, “Demonstration of transient gain x-ray lasers near 20nm for nickellike yttrium, zirconium, niobium, and molybdenum”, *Opt. Lett.* **24**, 101 (1999).
- [58] M. A. Henesian, C. D. Swift, and J. R. Murray, “Stimulated rotational Raman scattering in nitrogen in long air paths”, *Opt. Lett.* **10**, 565 (1985).
- [59] R. L. Carman, M. E. Mack, F. Shimizu, and N. Bloembergen, “Forward Picosecond Stokes-Pulse Generation In Transient Stimulated Raman Scattering”, *Phys. Rev. Lett.* **23**, 1327, (1969).
- [60] M. E. Mack, R. L. Carman, J. Reintjes, and N. Bloembergen, “Transient Stimulated Rotational And Vibrational Raman Scattering In Gases”, *Appl. Phys. Lett.* **16**, 209 (1970).
- [61] J. T. Verdeyen, *Laser Electronics*, Third Edition, Prentice-Hall Inc., Englewood Cliffs, NJ (1995).
- [62] Y. Ping, R. K. Kirkwood, T.-L. Wang, D. S. Clark, S. C. Wilks, N. Meezan, R. L. Berger, J. Wurtele, N. J. Fisch, V. M. Malkin, E. J. Valeo, S. F. Martins, and C. Joshi, “Development of a nanosecond-laser-pumped Raman amplifier for short laser pulses in plasma”, *Phys. Plasmas* **16**, 123113 (2009).
- [63] W. L. Kruer, “Intense laser plasma interactions: From Janus to Nova”, *Phys. Fluids B* **3**, 2356 (1991).

- [64] V. Malka, C. Coulaud, J. P. Geindre, V. Lopez, Z. Najmudin, D. Neely, and F. Amiranoff, “Characterization of neutral density profile in a wide range of pressure of cylindrical pulsed gas jets”, *Rev. Sci. Instrum.* **71**, 2329 (2000).
- [65] M. M. Marinak, G. D. Kerbel, N. A. Gentile, O. Jones, D. Munro, S. Pollaine, T. R. Dittrich, and S. W. Haan, “Three-dimensional HYDRA simulations of National Ignition Facility targets”, *Phys. Plasmas* **8**, 2275 (2001).
- [66] E. H. Lieb, “Thomas-Fermi and related theories of atoms and molecules”, *Rev. Mod. Phys.* **53**, 603 (1981).
- [67] N. B. Meezan, R. L. Berger, L. Divol, D. H. Froula, D. E. Hinkel, O. S. Jones, R. A. London, J. D. Moody, M. M. Marinak, C. Niemann, P. B. Neumayer, S. T. Prisbrey, J. S. Ross, E. A. Williams, S. H. Glenzer, and L. J. Suter, “Role of hydrodynamics simulations in laser-plasma interaction predictive capability”, *Phys. Plasmas* **14**, 056304 (2007).
- [68] L. Divol, R. L. Berger, N. B. Meezan, D. H. Froula, S. Dixit, P. Michel, R. London, D. Strozzi, J. Ross, E. A. Williams, B. Still, L. J. Suter, and S. H. Glenzer, “Three-dimensional modeling of laser-plasma interaction: Benchmarking our predictive modeling tools versus experiments”, *Phys. Plasmas* **15**, 056313 (2008).
- [69] G. Gregori, S. H. Glenzer, J. Knight, C. Niemann, D. Price, D. H. Froula, M. J. Edwards, R. P. J. Town, A. Brantov, W. Rozmus, and V. Yu. Bychenkov, “Effect of Nonlocal Transport on Heat-Wave Propagation”, *Phys. Rev. Lett.* **92**, 205006 (2004).
- [70] N. B. Meezan, *Private Communication*, 2009.
- [71] L. Spitzer and R. Härm, “Transport Phenomena in a Completely Ionized Gas”, *Phys. Rev.* **89**, 977 (1953).
- [72] J. D. Huba, *NRL Plasma Formulary*, Naval Research Laboratory, Washington D.C. (2002).
- [73] J. W. Goodman, “Some fundamental properties of speckle”, *J. Opt. Soc. Am.* **66**, 1145 (1976).
- [74] S. Skupsky and T. Kessler, “A source of hot spots in frequency-tripled laser light”, *Optics Communications* **70**, 123 (1989).
- [75] E. A. Williams, “On the control of filamentation of intense laser beams propagating in underdense plasma”, *Phys. Plasmas* **13**, 056310 (2006).

- [76] J. Garnier, “Statistics of the hot spots of smoothed beams produced by random phase plates revisited”, *Phys. Plasmas* **6**, 1601 (1999).
- [77] Y. Kato, K. Mima, N. Miyanaga, S. Arinaga, Y. Kitagawa, M. Nakatsuka, and C. Yamanaka, “Random Phasing of High-Power Lasers for Uniform Target Acceleration and Plasma-Instability Suppression”, *Phys. Rev. Lett.* **53**, 1057 (1984).
- [78] S. N. Dixit, J. K. Lawson, K. R. Manes, H. T. Powell, and K. A. Nugent, “Kinoform phase plates for focal plane irradiance profile control”, *Opt. Lett.* **19**, 417 (1994).
- [79] T. H. Bett, C. N. Danson, P. Jinks, D. A. Pepler, I. N. Ross, and R. M. Stevenson, “Binary phase zone-plate arrays for laser-beam spatial-intensity distribution conversion”, *Appl. Opt.* **34**, 4025 (1995).
- [80] J. A. F. Hittinger and M. R. Dorr, “Improving the capabilities of a continuum laser plasma interaction code”, *Journal of Physics: Conf. Series, SciDAC* **46**, 422 (2006).
- [81] R. L. Berger, B. F. Lasinski, T. B. Kaiser, E. A. Williams, A. B. Langdon, and B. I. Cohen, “Theory and three-dimensional simulation of light filamentation in laser-produced plasma”, *Phys. Fluids B* **5**, 2243 (1993).
- [82] C. H. Still, R. L. Berger, A. B. Langdon, D. E. Hinkel, L. J. Suter, and E. A. Williams, “Filamentation and forward Brillouin scatter of entire smoothed and aberrated laser beams”, *Phys. Plasmas* **7**, 2023 (2000).
- [83] E. S. Dodd, B. Bezzerides, D. F. DuBois, and H. X. Vu, “pF3d simulations of nonlinear laser propagation in a multi-speckle environment”, *Bull. Am. Phys. Soc.* **52**, 20 (2007).
- [84] D. E. Hinkel, D. A. Callahan, A. B. Langdon, S. H. Langer, C. H. Still, and E. A. Williams, “Analyses of laser-plasma interactions in National Ignition Facility ignition targets”, *Phys. Plasmas* **15**, 056314 (2008).
- [85] D. E. Hinkel, E. A. Williams, R. L. Berger, L. V. Powers, A. B. Langdon, and C. H. Still, “Propagation of realistic beams in underdense plasma”, *Phys. Plasmas* **5**, 1887 (1998).
- [86] D. H. Froula, L. Divol, R. A. London, P. Michel, R. L. Berger, N. B. Meezan, P. Neumayer, J. S. Ross, R. Wallace, and S. H. Glenzer, “Pushing the Limits of Plasma Length in Inertial-Fusion Laser-Plasma Interaction Experiments”, *Phys. Rev. Lett.* **100**, 015002 (2008).

- [87] N. A. Krall and A. W. Trivelpiece, *Principles of Plasma Physics*, McGraw-Hill Inc., New York (1973).
- [88] N. Lemos, N. Lopes, J. M. Dias, and F. Viola, “Design and characterization of supersonic nozzles for wide focus laser-plasma interactions”, *Rev. Sci. Instrum.* **80**, 103301 (2009).
- [89] M. Krishnan, J. Wright, and T. Ma, “A Fast, Electromagnetically Driven Supersonic Gas Jet Target For Laser Wakefield Acceleration”, *Advanced Accelerator Concepts: 13th Workshop Proceedings* (2009).
- [90] V. M. Malkin, G. Shvets, and N. J. Fisch, “Detuned Raman Amplification of Short Laser Pulses in Plasma”, *Phys. Rev. Lett.* **84**, 1208 (2000).
- [91] V. M. Malkin, Yu. A. Tsidulko, and N. J. Fisch, “Stimulated Raman Scattering of Rapidly Amplified Short Laser Pulses”, *Phys. Rev. Lett.* **85**, 4068 (2000).
- [92] V. M. Malkin and N. J. Fisch, “Manipulating ultraintense laser pulses in plasmas”, *Phys. Plasmas* **12**, 044507 (2005).
- [93] V. M. Malkin, N. J. Fisch, and J. S. Wurtele, “Compression of powerful x-ray pulses to attosecond durations by stimulated Raman backscattering in plasmas”, *Phys. Rev. E* **75**, 026404 (2007).
- [94] L. Yin, B. J. Albright, K. J. Bowers, W. Daughton, and H. A. Rose, “Saturation of Backward Stimulated Scattering of a Laser Beam in the Kinetic Regime”, *Phys. Rev. Lett.* **99**, 265004 (2007).
- [95] J. E. Fahlen, B. J. Winjum, T. Grismayer, and W. B. Mori, “Propagation and Damping of Nonlinear Plasma Wave Packets”, *Phys. Rev. Lett.* **102**, 245002 (2009).
- [96] R. R. Lindberg, A. E. Charman, and J. S. Wurtele, “Reduced kinetic description of weakly-driven plasma waves”, *Phys. Plasmas* **15**, 055911 (2008).
- [97] T.-L. Wang, D. Michta, R. R. Lindberg, A. E. Charman, S. F. Martins, and J. S. Wurtele, “Feasibility study for using an extended three-wave model to simulate plasma-based backward Raman amplification in one spatial dimension”, *Phys. Plasmas* **16**, 123110 (2009).
- [98] R. R. Lindberg, A. E. Charman, and J. S. Wurtele, “Self-consistent Langmuir waves in resonantly driven thermal plasmas”, *Phys. Plasmas* **14**, 122103 (2007).

- [99] D. Bénisti and L. Gremillet, “Nonlinear plasma response to a slowly varying electrostatic wave, and application to stimulated Raman scattering”, *Phys. Plasmas* **14**, 042304 (2007).
- [100] N. A. Yampolsky and N. J. Fisch, “Simplified model of nonlinear Landau damping”, *Phys. Plasmas* **16**, 072104 (2009).
- [101] N. A. Yampolsky and N. J. Fisch, “Effect of nonlinear Landau damping in plasma-based backward Raman amplifier”, *Phys. Plasmas* **16**, 072105 (2009).